

# WHAT IS LIFE

## 70 YEARS AFTER SCHRÖDINGER

Antti J. Niemi

*Department of Physics and Astronomy, Uppsala University, P.O. Box 803, S-75108, Uppsala,  
Sweden*

*Laboratoire de Mathématiques et Physique Théorique CNRS UMR 6083, Fédération Denis  
Poisson, Université de Tours, Parc de Grandmont, F37200, Tours, France*

*Department of Physics, Beijing Institute of Technology, Haidian District, Beijing 100081,  
China*



*Dedicated to the 70<sup>th</sup> anniversary of Schrödinger's 1944 Lectures in Dublin.*



# Preface

*"There are at present fundamental problems in theoretical physics awaiting solution, e.g. the relativistic formulation of quantum mechanics and the nature of atomic nuclei (to be followed by more difficult ones such as the problem of life)." (P.A.M. Dirac 1931)*

70 years ago Erwin Schrödinger presented a series of lectures at the Dublin Institute for Advanced Studies with the title *What is Life? The Physical Aspect of the Living Cell*. The lectures were subsequently published in the form of a small book [1]. According to Google Scholar this book has been cited even more frequently than Schrödinger's articles on quantum mechanics. In particular, it was credited by Crick and Watson as the source of inspiration that led them to reveal the double helix structure of DNA.

My lectures at les Houches were a celebration of the anniversary of Schrödinger's lectures, and for that reason I decided to share a title.

Besides Crick and Watson, Schrödinger's book has been, and continues to be, a source of inspiration to generations of physicists. But it seems to me that its full dimensionality might not yet have been fully comprehended, nor appreciated. In particular, the book has many parallels to Philip Anderson's highly inspiring 1972 article *More is different. Broken symmetry and the nature of the hierarchical structure of science*. [2]. Schrödinger clearly realised that *Bol'she* (больше) makes a difference when he wrote that

*... living matter, while not eluding the 'laws of physics' as established up to date, is likely to involve 'other laws of physics' hitherto unknown, which, however, once they have been revealed, will form just as integral a part of this science as the former.*

Time should be ripe to accept a universal formal definition of life in terms of proteins and their dynamics: Proteins are the workhorses of all living organisms, proteins are true nano-machines that participate in all the metabolic activities which constitutes life as we know it. From this perspective life is indeed something that can be modelled and understood using both known and still to be revealed laws that govern sub-cellular physics of live matter. For a physicist like me this is an exciting way to try and answer Schrödinger's question.

The underlying theme in my lectures is to view proteins as an exciting example of a physical system where much of Anderson's *Bol'she* can be found. Indeed, proteins seem to bring together *most* of the contemporary lines of research in modern theoretical physics: Geometry of string-like structures, topological solitons, spin chains, integrable models, equilibrium and non-equilibrium statistical physics, quest for entropy, emergent phenomena, ... and much, much more. Moreover, the tools that are needed to fully understand proteins range from highly formal to extensively numerical, and for a theorist there are almost endless opportunities to address questions with di-

rect and important experimental relevance; physical, chemical, biological, medical, ... The amount of data is *overwhelming* and it is readily accessible. Experiments can be done and directly compared with theoretical calculations and numerical computations; the subject continues to grow at a highly exponential rate.

These lectures were prepared for students in condensed matter physics, both theoretical and experimental. I assumed the students did not really have any prior knowledge of proteins, that they did not even know how protein looks like at the atomic level. Thus I begin with a *protein minimum*. It explains the basic facts that I think one needs to know, to get started in research on physics of proteins. The rest of the lectures address proteins from the point of view of a physicist, from a perspective that I hope appeals to the way a physicist thinks. As such the presentation could be somewhat intimidating to chemists and biologists who might find the concepts and techniques that I introduce as foreign, something they have not seen and are not accustomed to, in the context of a problem which is traditionally viewed as theirs. However, I assure you that everything I describe is very simple. A good command of basic algebra is all that it really takes to follow these lectures. Indeed, proteins brings physics together in a unique fashion with biology, chemistry, applied mathematics, even medical research. Theory and experiments. With the goal to understand matter that is alive. I hope you *catch the bug*, too!

These lectures are available on-line at

[http://topo-houches.pks.mpg.de/?page\\_id=255](http://topo-houches.pks.mpg.de/?page_id=255)

## Acknowledgements

I wish to thank my many collaborators, postdocs and students from whom I have learned so much on the subject of these lectures. They include Si Chen, Alireza Chenani, Maxim Chernodub, Jin Dai, Ulf Danielsson, Jan Davidsson, Thomas Garandel, Ivan Gordeliy, Jianfeng He, Yanzhen Hou, Konrad Hinsén, Shuangwei Hu, Theodora Ioannidou, Ying Jiang, Gerald Kneller, Andrei Krokhov, Nevena Litova, Jiaojia Liu, Adam Liwo, Martin Lundgren, Gia Maisuradze, Nora Molkenthin, Alexander Molochov, Alexander Nasedkin, Daniel Neiss, Xuan Nguyen, Stam Nicolis, Xubiao Peng, Fan Sha, Harold Scheraga, Adam Sieradzan, Ann Sinelnikova, Maxim Ulybushev, Yifan Zhou, and many many others (to whom I apologise if name is not mentioned above). I also thank Frank Wilczek for making me curious about Anderson's *большое*.

My research has been supported by CNRS PEPS grant, Region Centre Recherche d'Initiative Academique grant, Sino-French Cai Yuanpei Exchange Program (Partenariat Hubert Curien), Vetenskapsrådet, Carl Trygger's Stiftelse för vetenskaplig forskning, and Qian Ren Grant. I thank the organisers of the *Topological Aspects in Condensed Matter Physics* Claudio Chamon, Mark Goerbig and Roderich Moessner for giving me the opportunity to present these lectures at Les Houches. I thank International Institute of Physics in Natal, Brazil for hospitality during the writing of these notes. Last but not least, thanks to the great audience at Les Houches!





# Contents

<b>1</b>	<b>A Protein Minimum</b>	<b>1</b>
1.1	Why proteins	1
1.2	Protein chemistry and the genetic code	2
1.3	Data banks and experiments	3
1.4	Phases of proteins	6
1.5	Backbone geometry	9
1.6	Ramachandran angles	11
1.7	Homology modelling	13
1.8	All-atom models	14
1.9	All-atom simulations	16
1.10	Thermostats	17
1.11	Other Physics-based approaches:	20
<b>2</b>	<b>Bol'she</b>	<b>22</b>
2.1	The importance of symmetry breaking	22
2.2	An optical illusion	23
2.3	Fractional charge	23
2.4	Spin-charge separation	25
2.5	All-atom is Landau liquid	28
<b>3</b>	<b>Strings in three space dimensions</b>	<b>30</b>
3.1	Abelian Higgs Model and the limit of slow spatial variations	30
3.2	The Frenet Equation	32
3.3	Frame rotation and abelian Higgs multiplet	33
3.4	The unique string Hamiltonian	35
3.5	Integrable hierarchy	35
3.6	Strings from solitons	36
3.7	Anomaly in the Frenet frames	38
3.8	Perestroika	40
<b>4</b>	<b>Discrete Frenet Frames</b>	<b>42</b>
4.1	The $C\alpha$ trace reconstruction	44
4.2	Universal discretised energy	45
4.3	Discretized solitons	48
4.4	Proteins out of thermal equilibrium	49
4.5	Temperature renormalisation	50
<b>5</b>	<b>Solitons and ordered proteins</b>	<b>54</b>
5.1	$\lambda$ -repressor as a multi-soliton	54
5.2	Structure of myoglobin	57

**xii**   *Contents*

5.3	Dynamical myoglobin	64
<b>6</b>	<b>Intrinsically disordered proteins</b>	<b>75</b>
6.1	Order vs. disorder	75
6.2	hIAPP and type-II diabetes	77
6.3	hIAPP as a three-soliton	79
6.4	Heating and cooling hIAPP	83
<b>7</b>	<b>Beyond <math>C\alpha</math></b>	<b>88</b>
7.1	"What-you-see-is-what-you-have"	89
	<b>References</b>	<b>95</b>

# 1

## A Protein Minimum

---

### 1.1 Why proteins

Proteins are nano-scale machines that control and operate all metabolic processes in all living organisms. Proteins often have to function with extreme precision: Like most machines, those made of proteins need to have their parts and pieces in the right place, in a good shape and finely tuned. How else could these self-producing nano-machines work in such a great harmony, cooperate over an enormous range of scales and uphold something as complex as life? Indeed, it is widely understood that the biological function of a protein depends critically on its three dimensional geometry. From this perspective the so called *protein folding problem* that aims to explain and derive the shape of a biologically active protein using laws of physics, addresses the origin of life itself [3, 4].

Furthermore, a wrong fold is a common cause for a protein to lose its function. A wrongly folded protein can be dangerous, even fatal, to a biological organism. It is now widely understood that diverse neurodegenerative diseases including various forms of dementia such as Alzheimer's and Parkinson's, type-II diabetes, and about half of all cancers, are caused by wrong folds in certain proteins [5]. At the same time, bacteria are on the rampage and emergent resistance through evolutionary processes renders existing antibiotics ineffective at a rapid pace [6–8]. No effective methods and treatments have been found to prevent or cure viral maladies like HIV, Ebola, or respiratory syndromes such as SARS and MERS. Our future protection against these and various other harmful and deadly pathogens depends on our skills and knowledge to develop conceptually new, protein-level approaches to fight and eliminate our enemies. Research on proteins is really about 'Saving the Planet' as much as in any video game or movie ever made. But it is for real: By doing research on proteins you have a chance to become a real-life *Gordon Freeman*.

For all these and many other reasons the ability to accurately describe the physics of proteins, their structure and dynamics, would have an enormous impact on biology, pharmacy, and health sciences. It would provide huge benefits to the society by paving ways to prevent and cure many tormenting diseases. In particular, it would provide us an answer to *what is life* along the lines foreseen by Schrödinger.

In the following I will give a short introduction to proteins, what you need to get your research started as a physicist. For those who are really seriously interested in the biological aspects, I recommend the textbook *Molecular Biology of the Cell* [9].

## 1.2 Protein chemistry and the genetic code

Proteins are one dimensional linear polymers. Proteins are composed of twenty different amino acids that share a number of structural properties: There are the *backbone* atoms which are common to all amino acids. There are the *residues* or *side-chains* which are different for each of the twenty amino acid.

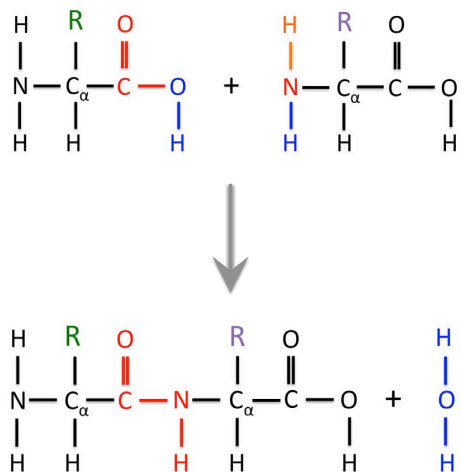


**Fig. 1.1** Amino acids have a common backbone with heavy atom pattern  $-\text{N}-\text{C}-\text{C}-\text{O}-$  but there are also twenty different residues (side-chains) which we denote R. When two amino acids combine together we obtain a di-peptide, in addition of a water molecule.

In Figure 1.1 we show the chemical composition of a generic amino acid. When two amino acids meet, a chemical process can take place that joins them together into a di-peptide plus water, as shown in the Figure. When this process repeats itself we eventually arrive at a long polypeptide chain *a.k.a.* protein as shown in Figure 1.2. Once the protein attains the correct shape, it becomes ready for biological action.

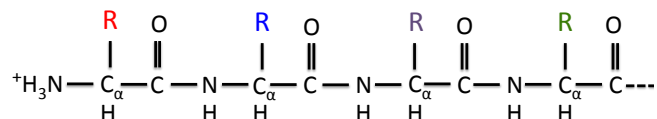


**Fig. 1.2** Proteins are long linear chains of amino acids, each with a self-similar backbone structure but twenty different residue structures (R).

Note the carbon atoms that are denoted  $\text{C}_\alpha$  in Figures 1.1 and 1.2. These are called the  $\alpha$ -carbon, and they have a central rôle in protein structure. As shown in the Figures the  $\text{C}_\alpha$  carbons connect the residues to the backbone; the  $\text{C}_\alpha$  forms the center of a  $sp^3$ -hybridised tetrahedron which subjects it to strong steric constraints, and holds it rigidly in place in relation to the other atoms. As we shall find the  $\text{C}_\alpha$

carbons largely determine the shape of the protein. Thus much of our subsequent analysis of protein structure and dynamics is based on the central rôle of the  $C\alpha$ , for reasons that become increasingly apparent as we proceed.

In a living organism like you and me, the instructions for making proteins are stored in our *genome*. At the level of DNA the *genetic code* consists of a sequence of nucleobases, that connect the two strands of DNA. A group of three nucleobases corresponds to a single amino acid; there is a segment of DNA, for each protein. The genetic code is copied from DNA to RNA in a process called *transcription*. This process, like all other processed in our body is driven by various proteins. Particular proteins called enzymes act as catalysts to help and control complex biological reactions.

Our DNA consists of four different nucleobases. Hence there are  $4 \times 4 \times 4 = 64$  different combinations. But two of them are instructions to *stop* the process of transcription. Thus we have a total of 62 combinations of nucleobases that encode the 20 amino acids, the genetic code is degenerate.

*Research project: From the point of view of Physics, we have an appetising similarity between genetic code where a group of three nucleobases corresponds to an amino acid, and the Standard Model where baryons are made of three quarks. Can you find a symmetry principle akin the Eightfold Way that relates the 62 codons to the 20 amino acids? Hint: A good way to start trying is to follow [10].*

Once formed, the RNA has the mission to carry the genetic code to a ribosome. A ribosome is essentially a nano-scale 3D printer. It is made of proteins, and it has the duty to produce new proteins according to the instructions given to it by RNA. The process where ribosome combines amino acids into a protein chain is called *translation*.

### 1.3 Data banks and experiments

The amount of data and information which is available in internet is abundant, both on the genetic code and on proteins. There are various open-access libraries both on the sequences and on the structures of proteins; the amount of data is already more than any single person can possibly ever analyse, and it continues to increase at an exponential rate.

For those who are mainly interested in biology and related bioinformatics, an excellent resource on protein sequences and their biological function is

$$\text{http} : // \text{www.uniprot.org/} \quad (1.1)$$

This data bank contains presently almost 90 million different protein sequences. As shown in Figure 1.3 (left) the number of known sequences grows at a very high, exponential rate.

For those who are mainly interested in physics of proteins, *Protein Data Bank* (PDB) is an excellent resource

$$\text{http} : // \text{www.pdb.org/} \quad (1.2)$$

As shown in Figure 1.3 (right) the number of known protein structures in PDB is around 100.000 and growing. But not at all as fast as the number of known sequences, only about 0.1% of known protein sequences have a known structure.

#### 4 A Protein Minimum

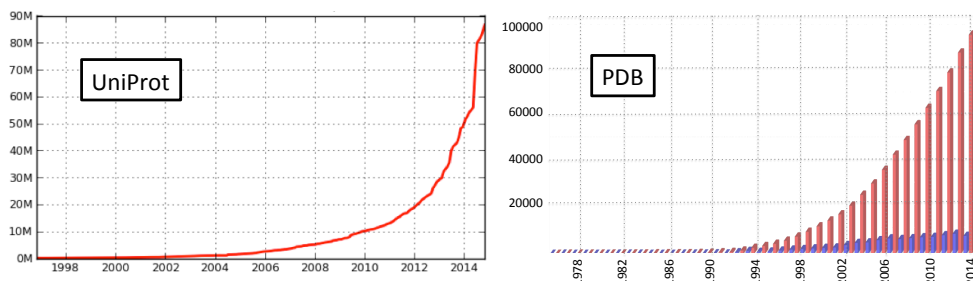


**Fig. 1.3** *Left:* The increase in the number of sequences in *Uniprot*, as a function of year, taken from (1.1). *Right:* The increase in the number of structures in PDB as a function of year. Both annual increase and accumulated total are shown. Taken from (1.2).

Numerous other good sources of information exist and can be found in internet. For example *PSI-Nature Structural Biology Knowledgebase* is a comprehensive database for various structural aspects of proteins. It can be found at

<http://sbkb.org/>

Most of the 100.000 structures in PDB have been resolved using x-ray crystallography. But other techniques are also being used. In particular, the number of NMR structures is increasing. Until now it has been very difficult to resolve long protein sequences using NMR techniques. Most NMR structures are quite short, those with more than 100 amino acids are rare. The advantage of NMR where no crystallisation is needed over x-ray crystallography is, that NMR can more easily provide dynamical information. It is possible to follow proteins in motion using NMR, while crystallised structures have problems moving. But even x-ray techniques such as small angle x-ray scattering (SAXS) and wide angle x-ray scattering (WAXS) are now being developed, to observe proteins in motion. In the near future, equipments including free electron lasers can provide detailed structural and dynamical information, at very short time scales. Various other methods are also in use and under development: The experimental study of protein structure and dynamics is still very much in its infancy. This makes the study of proteins into an exciting field to enter, also for those who are experimentally minded. New techniques are developed and introduced, all the time.

The protein crystals in PDB are *ordered*, they are commonly presumed to display a crystallised conformation which is close to the biologically active one. But *most* proteins are apparently intrinsically unstructured. Such proteins can not be crystallised into any kind of biologically unique conformation. When these proteins are biologically active, they do not have any single conformation. Instead they change their form, perpetually. Most proteins in our body are like this, intricate nano-machines that are in a constant action. Very little, in fact next-to-nothing, is known on the structural aspects of intrinsically unstructured proteins. In these lectures we shall look at examples of both ordered and intrinsically disordered proteins.

Our experimental considerations will mainly make use of a subset of crystallographic PDB structures which have been measured with a ultra-high precision, with

a resolution better than 1.0 Å. The reason why we prefer to use these ultra-high resolution structures is due to a process called *refinement* that commonly takes place during experimental data validation and model building [11]. During refinement and validation, one iteratively improves the parameters of an approximate trial structure of the experimental observations, until one obtains some kind of a best fit between the trial structure and the observed diffraction pattern. As an *Ansatz*, and as reference, the process utilises known experimental crystallographic structures. Widely used experimentally determined, highly accurate template libraries of small molecules include the one by Engh and Huber [12]. Thus, the process of refinement *might* introduce a bias towards structures that are already known. In particular, it is not clear to what extent the structure of a small molecule persists in the complex, highly interactive environment of a large protein.

Indeed, it is important to recognise and keep in mind that the PDB data files are prone to all kinds of errors [11,13–15]. The data should be used with care. *Molprobability* is an example of a web-server that can be used to analyse the quality of an experimental protein structure. It can be found at

$$\text{http://molprobability.biochem.duke.edu/} \quad (1.3)$$

One might presume that in the case of ultra-high resolution structures, those that have been measured with better than 1.0 Å resolution, the quality of observed diffraction pattern should be very good. These structures should have much less need for refinement, during the model building. Thus, they should be much less biased towards known structures. The number of misplaced atoms should be relatively low.

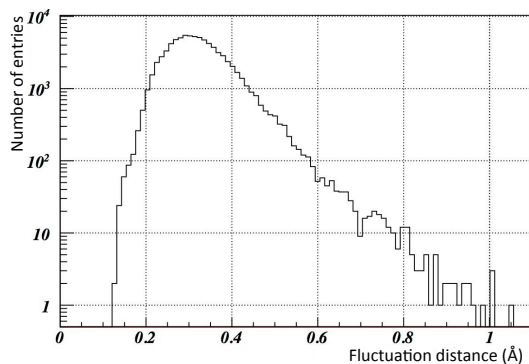


**Fig. 1.4** The distribution of the Debye-Waller fluctuation distance for the C $\alpha$  atoms, among those crystallographic PDB structures that have been measured with better than 1.0 Å resolution.

In order to minimise radiation damage, crystallographic structures are often measured at temperatures which are near that of liquid nitrogen *i.e.* around 80-90 Kelvin. Thus the thermal fluctuations in the atomic coordinates should be small. In the PDB data, the experimental uncertainty in the atomic coordinates is estimated by the (temperature) B-factors. Besides the thermal fluctuations, these B-factors summarise also

## 6 A Protein Minimum

all the other uncertainties that the experimentalist thinks affects the precision. In Figure 1.4 we show the distribution of the Debye-Waller fluctuation distance in our subset of the ultra-high precision structures, for the  $C\alpha$  atom coordinates. The fluctuation distance can be estimated using the Debye-Waller relation,

$$\sqrt{\langle \mathbf{x}^2 \rangle} \approx \sqrt{\frac{B}{8\pi^2}} \quad (1.4)$$

This corresponds roughly to the one standard deviation uncertainty in the experimentally measured coordinate values. In Figure 1.5 is an example of a generic PDB entry that shows how the B-factors are listed together with the atomic coordinates.

ATOM	98	N	HIS	A	12	37.554	22.049	-3.039	1.00	7.00	N
ATOM	99	CA	HIS	A	12	38.052	23.320	-2.567	1.00	7.99	C
ATOM	100	C	HIS	A	12	37.862	23.459	-1.070	1.00	6.88	C
ATOM	101	O	HIS	A	12	38.654	24.106	-0.390	1.00	7.05	O
ATOM	102	CB	HIS	A	12	37.387	24.460	-3.314	1.00	11.49	C
ATOM	103	CG	HIS	A	12	38.195	24.796	-4.556	1.00	15.84	C
ATOM	104	ND1	HIS	A	12	39.254	25.596	-4.535	1.00	18.10	N
ATOM	105	CD2	HIS	A	12	38.101	24.186	-5.778	1.00	17.75	C
ATOM	106	CE1	HIS	A	12	39.815	25.479	-5.722	1.00	18.99	C
ATOM	107	NE2	HIS	A	12	39.122	24.635	-6.465	1.00	19.38	N

**Fig. 1.5** An example of PDB file, in this case the amino acid histidine (HIS). The second column lists the atom number (98-107) along the backbone. The third column lists the type of the atom; CA stands for  $C\alpha$ , and the entries 98-101 are the backbone N- $C\alpha$ -C-O atoms of HIS. The entries 102-107 are side chain atoms. In this case, HIS is the 12<sup>th</sup> amino acid along the backbone. The  $(x, y, z)$  coordinates are listed in the following three columns. The B-factors are listed in the last column, before a list of the chemical symbols. Note that in this list, the hydrogen atoms are absent. Hydrogens can be difficult to observe.

According to Figure 1.4, among our ultra-high resolution PDB structures the one standard deviation error distance in the  $C\alpha$  atomic positions peaks in the range of 0.3 - 0.5 Ångström. The lower bound is around 0.15 - 0.2 Ångström and in these lectures we shall adopt  $\sim 0.15$  Å i.e. around 20% of the radius of the carbon atom, as the lower bound estimate for the size of quantum mechanical zero point fluctuations in the  $C\alpha$  positions. Note that historically  $\sim 0.2$  Å has been considered as the boundary between x-rays and  $\gamma$ -rays.

## 1.4 Phases of proteins

Like most linear polymers, proteins have a highly complex phase structure that can depend on a multitude of factors, including the chemical structure of a polymer and its solvent, temperature, pressure, changes in solvent's acidity and many other environmental factors [16, 17]. In a good solvent environment, the interactions between a polymer segment and the solvent molecules usually cause the polymer to expand, and the polymer behaves like a self-avoiding random walk. In a poor solvent environment, such as water that surrounds proteins in our cells, the polymer-polymer self-interactions dominate and the polymer tends to collapse into a space filling conformation. These two phases are separated by a  $\theta$ -regime, where the repulsive and



attractive interactions cancel each other and the polymer has the geometric character of a random walk (Brownian motion).

In the limit where the number  $N$  of monomers is very large, many aspects of the phase structure become *universal* [18–20]. An example of a universal quantity in the case of a linear polymer such as a protein, is the compactness index  $\nu$ . It is defined in terms of the radius of gyration  $R_g$  [16, 17, 21–23]

$$R_g^2 = \frac{1}{2N^2} \sum_{i,j} (\mathbf{r}_i - \mathbf{r}_j)^2 \quad (1.5)$$

Here  $\mathbf{r}_i$  are the coordinates of all the atoms in the polymer. In the case of a protein, with no loss of generality we may restrict  $\mathbf{r}_i$  to the coordinates of the backbone C $\alpha$  atoms only. The compactness index  $\nu$  governs the large- $N$  asymptotic form of (1.5). When the number  $N$  of monomers becomes very large, we have [23]

$$R_g^2 \xrightarrow{N \text{ large}} R_0^2 N^{2\nu} (1 + R_1 N^{-\delta_1} + \dots) \quad (1.6)$$

It should be obvious that  $\nu$  coincides with the inverse Hausdorff dimension of the structure. Besides the compactness index  $\nu$ , the critical exponents  $\delta_1$  etc. are also universal quantities. But the form factor  $R_0$  that characterises the effective distance between the monomers in the large  $N$  limit, and the subsequent amplitudes  $R_1$  etc. that parametrise the finite size corrections, are not universal [23]. These parameters can in principle be computed from the chemical structure of the polymer and solvent, in terms of environmental factors such as temperature and pressure.

As a universal quantity,  $\nu$  is independent of the detailed atomic structure. Different values of  $\nu$  correspond to different phases of polymer. The four commonly accepted mean-field values of  $\nu$  are

$$\nu = \begin{cases} 1/3 \\ 1/2 \\ 3/5 \\ 1 \end{cases} \quad (1.7)$$

Under poor solvent conditions such as in the case of proteins in our cells, a linear single chain polymer collapses into the space filling conformation and we have the mean field exponent  $\nu = 1/3$ . For a fully flexible ideal chain the mean field value is  $\nu = 1/2$ . This phase takes place at the  $\theta$ -regime that separates the collapsed phase from the high temperature self-avoiding random walk phase, for which we have the mean field Flory value  $\nu = 3/5$ . Finally, when  $\nu = 1$  the polymer is like a rigid stick. Some proteins are like this, some collagens for example.

*Research project: Three dimensional dynamical systems such as the Lorenz equation provide numerous examples of space curves with attractors that have all kind of Hausdorff dimensions. Can you find physical examples of polymers (proteins) where  $\nu$  takes values that correspond to phases which are different from the four listed in (1.7)?*

The mean-field values of the critical exponents  $\nu$ ,  $\delta_1$  etc. in equation (1.6) may be corrected by fluctuations. In particular, in the universality class of the self-avoiding random walk the improved values are [24, 25]

## 8 A Protein Minimum

$$\begin{aligned}\nu &= 0.5880 \pm 0.0015 \\ \delta_1 &= 0.47 \pm 0.03\end{aligned}\tag{1.8}$$

The computation of (1.8) in [24, 25] utilises the concept of universality to argue that the three dimensional self-avoiding random walk is in same universality class with the  $O(n)$  symmetric scalar field theory with a quartic self-interaction, in the limit where the number of components  $n \rightarrow 0$ . A subsequent numerical Monte Carlo evaluation of the critical exponents (1.8), computed using a self-avoiding random walk model on a square lattice [23] gave very similar values

$$\begin{aligned}\nu &= 0.5877 \pm 0.0006 \\ \delta_1 &= 0.56 \pm 0.03\end{aligned}\tag{1.9}$$

In the case of crystallographic PDB protein structures, we may evaluate the dependence of the radius of gyration on the number of residues using the coordinates of the  $C\alpha$  atoms. The result is shown in Figure 1.6. A least-square fit to the data gives

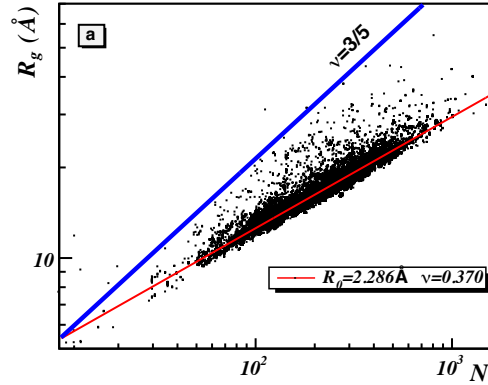


**Fig. 1.6** The  $C\alpha$  radius of gyration as a function of residues, in the case of those monomeric crystallographic PDB proteins that have been measured with better than  $2.0 \text{ \AA}$  resolution. The red line is the least-square linear fit, and the blue line denotes the Flory value  $\nu = 3/5$ .

$$R_g \approx R_0 N^\nu \approx 2.280 N^{0.375} \text{ \AA} \tag{1.10}$$

Note that proteins are not homopolymers. But when  $N$  increases, the detailed amino acid structure of a protein should become increasingly irrelevant in determining the relation between the radius of gyration and the number of residues. For long protein chains, the inhomogeneity due to amino acids should be treated as a finite size correction in (1.6), when  $N$  becomes very large. Indeed, in the limit of very large number of residues a generic protein is like a chain along which the 20 residues have been quite randomly distributed. It should be like a spin-chain embedded in  $\mathbb{R}^3$  where each residue is a spin variable, with 20 different (random) values. Thus, when the ratio

$20/N$  becomes very small the effect of an individual residue becomes small in an average, statistical sense. The protein approaches a homopolymer that is equipped with an "averaged" residue.

*Research project: Develop theory of spin chains embedded in  $\mathbb{R}^3$ .*

## 1.5 Backbone geometry

According to Figure 1.6, those proteins that can be crystallised are in the collapsed  $\nu \approx 1/3$  phase. To describe the properties of their thermodynamical phase state, we need to identify a proper set of *order parameters* in the sense of Landau, Ginzburg and Wilson; the concept of order parameter is described in numerous textbooks.<sup>1</sup> A local order parameter is a systematically constructed effective dynamical variable, that describes collectively a set of elemental degrees of freedom such as atoms and molecules, in a system that is subject to the laws of statistical physics. Examples of an order parameter include magnetisation in the case of a ferromagnet, director in a nematic crystal, condensate wave function in superfluid  $He^4$ , and Cooper pair in a BCS superconductor. The concept of an order parameter is often intimately related to the concept of symmetry breaking and emergent phenomena. For example, in each of the cases that we mentioned, we have a symmetry that becomes broken, and this symmetry breaking gives rise to emergent structures. In particular, the breaking of the symmetry is described in terms of the properties of the pertinent order parameter, in each case.

In the case of a protein, we have already concluded that the phase structure relates to the aspects of protein geometry. The different phases of a protein are characterised by different Hausdorff dimensions (1.7). Moreover, proteins have an apparent symmetry that has become broken:

Amino acids are chiral molecules. An amino acid can be either left-handed (L) or right-handed (D). The only exception is glycine which has no chirality. For two amino acids to form a di-peptide as shown in Figure 1.1, they must have the same chirality; you can't easily shake someones left hand with your own right. For some reason the symmetry between L and D is broken in Nature, practically all amino acids that appear in proteins of living organisms from prokaryotes such as bacteria to eukaryotes like us, are left-handed chiral. This symmetry breaking apparently reflects itself to higher level geometric structures of proteins: As a polymer chain, the proteins that are found in living organisms are more often twisted in a *right-handed* manner, that the opposite. Thus, any local order parameter that describes the phase properties of proteins in living organism, should somehow capture the helical aspects of protein geometry.

Figure 1.7 details the local geometry of a protein. In this Figure we identify a  $C\alpha$  atom together with its covalently bonded N, C, H atoms, and the residue R that starts with a covalently bonded carbon atom called  $C\beta$ . The covalent bonds between these five atoms form a *sp*<sup>3</sup> hybridised tetrahedron, with  $C\alpha$  at the centre. Take the C atom to be the top of the tetrahedron, and N, H, R as the three bottom vertices. Consider the axis of the tetrahedron that runs along the covalent bond from the C to  $C\alpha$  and

<sup>1</sup>In the context of protein research, order parameters are sometimes called *reaction coordinates*.

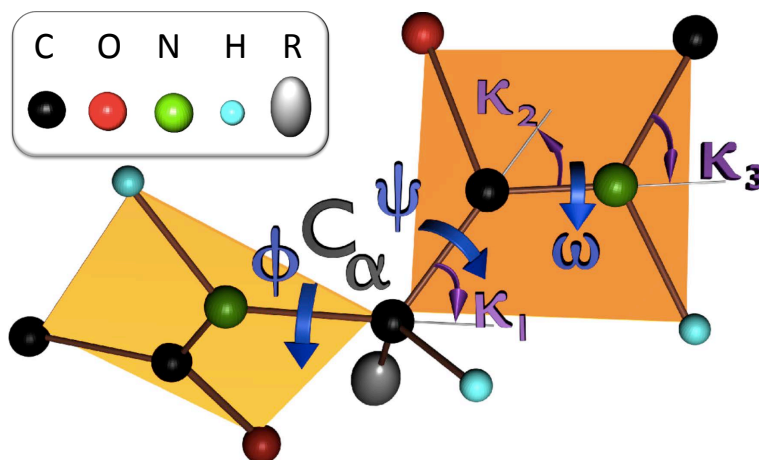


**Fig. 1.7** The atoms along the protein backbone form peptide planes; the two covalent bonds C=O and N-H are anti-parallel. The figure also shows the definition of the various bond and torsion angles, between the covalent bonds. The two torsion angles ( $\phi, \psi$ ) are the Ramachandran angles.

look down this axis from C towards  $C\alpha$ . If the H atom is in the clockwise direction from residue R, the amino acid is left-handed; this is the case in Figure 1.7. Otherwise, the amino acid is right-handed.

In Figure 1.7 we have also two *peptide planes*, one which is prior to the  $C\alpha$  atom and another which is after the  $C\alpha$  atom. The  $C\alpha$  atom is located at the joint vertex of the two adjacent peptide planes. We proceed to analyse in detail the properties of the peptide plane geometry.

It turns out that the geometry of the peptide planes is indeed very rigidly planar. The planarity is measured by the angle  $\omega$  which is shown in Figure 1.7; it is the angle between the C=O covalent bond, and the N- $C\alpha$  covalent bond (or N-H covalent bond). The values of  $\omega$  are found to fluctuate very little around  $\omega = \pi$ , which corresponds to the *trans*-conformation of the backbone and is shown in the Figure; there are a few entries, mainly involving the amino acid *proline*, where the backbone is in the *cis*-conformation where  $\omega$  vanishes. The *cis*-conformation is equally planar, the fluctuations around  $\omega = 0$  are minimal. Figure 1.8 shows the distribution of the  $\omega$  angles in our ultra high resolution subset of crystallographic protein structures, those that have been measured with better than 1.0 Å resolution. In addition, the values of the three covalent bond angles ( $\kappa_1, \kappa_2, \kappa_3$ ) that are defined in Figure 1.7 are shown in this Figure. Their values are likewise subject to relatively small variations.

The various covalent bond lengths along the protein backbone have also values that fluctuate very little around their average values. Figure 1.9 shows the various bond lengths between the heavy atoms along the backbone. We also show the distance

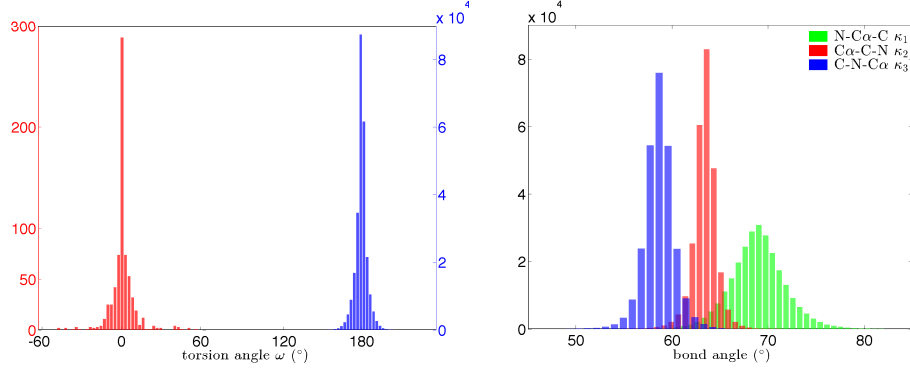


**Fig. 1.8** Left: Distribution of the torsion angle  $\omega$  between the covalent bonds C=O and N-H in Figure 1.6, in our ultra high 1.0 Å resolution PDB subset. The result shows that the geometry of the peptide planes is indeed planar, with very high precision. For *trans* we have  $\omega \approx \pi$  and for *cis* we have  $\omega \approx 0$ . Right: The distribution of the three bond angles ( $\kappa_1, \kappa_2, \kappa_3$ ) defined in Figure 1.7 in our data set. The variation around the average values is relatively small.

between two consecutive C $\alpha$  atoms, which is also subject to very small fluctuations.

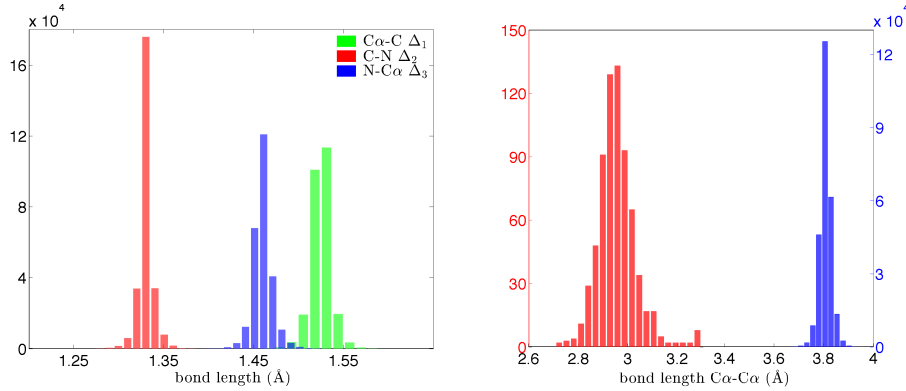


**Fig. 1.9** Left: Distribution of the three covalent bond lengths C $\alpha$ -C, C-N and N-C $\alpha$  shown in Figure 1.7, along the protein backbone. Right: Distribution of the length between neighboring C $\alpha$  atoms, along the protein backbone. The smaller value  $\sim 3.0$  Å corresponds to *cis*, and the larger value  $\sim 3.8$  Å is for *trans*.

## 1.6 Ramachandran angles

The Figures 1.8 and 1.9 show that the three covalent bond angles ( $\kappa_1, \kappa_2, \kappa_3$ ), the torsion angle  $\omega$  and the various covalent bond lengths reveal no dependence on local geometry. Each of these variables have fairly uniform distributions, which is appar-

ently quite insensitive to variations in local backbone geometry. Thus we are left with only the two Ramachandran angles  $(\phi, \psi)$  in Figure 1.7 as the potential local order parameters, to characterise local geometry along the backbone. Indeed, it turns out that the variations in their values are *not* small, and in particular appears to depend on backbone geometry. This is shown by the Ramachandran map in Figure 1.10, that displays the  $(\phi, \psi)$  distribution in PDB structures which have been measured with better than 2.0 Å resolution. Note the asymmetry, both in  $\phi$  and in  $\psi$ ; this asymmetry

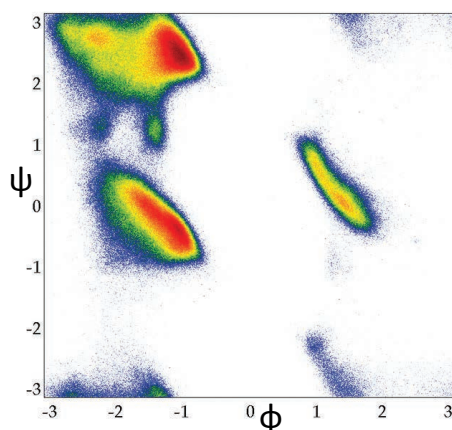


**Fig. 1.10** Distribution of Ramachandran angles  $(\phi, \psi)$  defined in Figure 1.7 in radians.

translates into helicity of the protein backbone. Regular right-handed helical structures (right-handed  $\alpha$ -helices) are quite common, while left-handed helical structures are very rare.

Since the phase structure of a protein relates to its geometry, we may expect that the set of the two Ramachandran angles could be utilised as the local order parameters to describe the phase structure of proteins. However, it turns out that this is not the case [26]: The Ramachandran angles form an incomplete set of local order parameters. To show this, we consider all the PDB structures in our data set of ultra-high resolution structures, those that have been measured with better than 1.0 Å resolution. We do the following *reconstruction*:

From the PDB coordinates of the atoms we first compute the numerical values of all the Ramachandran angles, for each and every peptide plane. Then we continue and do the inverse: We start from the Ramachandran angles that we have computed, and we assume that all the other angles and bond lengths have their average values. We then try to reconstruct the original protein structure, by computing the  $C\alpha$  coordinates.

It turns out that this reconstruction of the coordinates, going from  $C\alpha$  to Ramachandran and the back, usually fails. It is not possible to do such a reconstruction, in the case of a generic protein.

In Figure 1.11 we show how the reconstructed proteins fail to reproduce even the correct fractal geometry of folded proteins [26]. Instead of (1.10), we obtain the asymptotic relation

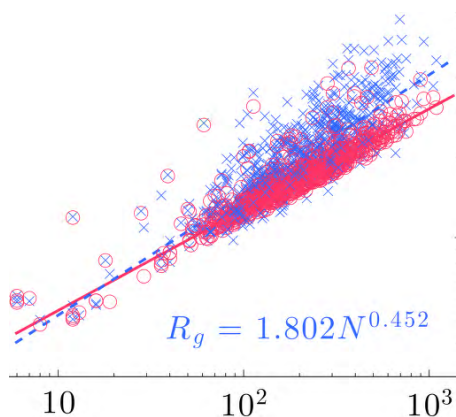


**Fig. 1.11** Comparison of  $R_g$  between the PDB structures, and the structures obtained by a reconstruction which is based on Ramachandran angles, with all other backbone angles and bond lengths set to their ideal values. Red circles are the original PDB structures, blue crosses are the reconstructed structures.

$$R_g \approx 1.8 N^{0.45} \text{ \AA}$$

for the reconstructed protein structures: The inverse Hausdorff dimension  $\nu = 0.45$  is incorrect. In order to reconstruct the correct fractal geometry, it turns out that we need to include *all* the angular variables in Figure 1.7, as variables. Only for the bond lengths, can the average PDB values be used.

Eventually, in a subsequent lecture, we shall construct a *different* set of local order parameters and we show their completeness. However, we first address the modelling of proteins in terms of their (primary) full atom level description.

## 1.7 Homology modelling

As shown in Figure 1.3 (left), the number of sequences in *Uniprot* grows at a rate which is much higher than that of structures in PDB, shown in Figure 1.3 (right). The gap is enormous and keep on growing: Sequencing is now fast, cheap and routine while crystallographic protein structure determination is difficult, time consuming, and often very expensive; apparently the average cost of a PDB structure is around 100 kUSD. Thus it is impossible to close the gap between sequences and structures by purely experimental methods. To close this gap we need to develop efficient and accurate computational methods.

Homology<sup>2</sup> modelling [27–29] together with other comparative modelling techniques, is presently the most reliable and effective approach to generate a three-dimensional model of a protein structure from the knowledge of its amino acid sequence. These methods are consistently the top performers in the bi-annual *Critical Assessment of protein Structure Prediction* (CASP) tests, see

<sup>2</sup>Homology between two proteins is commonly measured on the basis of amino acid sequence similarity. High sequence similarity is a sign of shared ancestry, but for short proteins it can also occur due to chance.

<http://predictioncenter.org/>

Homology modelling techniques aim to construct the atomic level structure of a given protein (target), by comparing its amino acid sequence to various libraries of known, homologically related protein structures (templates). Apparently the reason why this kind of methods work is as follows: It seems to be the case that the number of possible protein folds in nature is limited, and that the three-dimensional protein structures seem to be better conserved than the amino acid sequences [30]. However, the quality of a model obtained for the target is largely dictated by the evolutionary distance between the target and the available template structures. If no closely homologous template can be found, these approaches typically fail.

From the point of view of Physics, any template based approach has the disadvantage that there is no energy function. Thus, no energetic analyses of structure and dynamics can be performed. For this, other techniques need to be introduced: To understand the physical properties of a protein we need to know the energy function.

*Research project: Try to develop a structure prediction approach that uses the best of both worlds: One that finds an initial Ansatz structure using templates, and then develops it using techniques of Physics. For hints, continue reading ...*

## 1.8 All-atom models

*... if we were organisms so sensitive that a single atom, or even a few atoms, could make a perceptible impression on our senses -Heavens, what would life be like! (E. Schrödinger)*

We present a short overview of all-atom molecular dynamics, where impressive progress is being made. The aim of an all-atom approach is to model the way a protein folds, by following the time evolution of each and every atom involved including those of the surrounding solvent (water). But despite impressive progress, the subject remains very much under development and provides enormous challenges to those brave enough to face them: Both conceptual level and technical level problems remain to be resolved, involving issues relevant to physics, chemistry, computer science, and also problems for those interested in optimisation and efficient algorithm development.

There are many examples of all-atom energy functions, called force fields in this context. The most widely used are *Charmm* [31] and *Amber* [32]; we also mention *Gromacs* [33] which is a popular platform for performing molecular dynamics (MD) simulations using different force fields.

A typical all atom force field that describes a protein chain with  $N$  atoms has the following generic form

$$E(r^N) = \sum_{bonds} \frac{k_b}{2} (l - l_0)^2 + \sum_{angles} \frac{k_a}{2} (\kappa - \kappa_0)^2 + \sum_{torsions} \frac{V_n}{2} [1 + \cos(n\omega - \gamma)] \quad (1.11)$$

$$+ \sum_{j=1}^{N-1} \sum_{i=j+1}^N \left\{ \epsilon_{i,j} \left[ \left( \frac{r_{0ij}}{r_{ij}} \right)^2 - 2 \left( \frac{r_{0ij}}{r_{ij}} \right)^6 \right] + \frac{q_i q_j}{4\pi\epsilon_0 r_{ij}} \right\} \quad (1.12)$$

The first two contributions in (1.11) describe harmonic oscillations of the bond lengths and bond angles around certain *ideal values* ( $l_0, \kappa_0$ ). The third contribution involves



torsion angles and evokes a mathematical pendulum, similarly with *ideal value* ground state(s) given by  $\gamma$ . Torsion angles  $\omega$  are often found to be much more flexible than bond angles  $\kappa$ , thus the numerical values of  $V_n$  are commonly orders of magnitude smaller than those of  $k_a$ . Moreover, a mathematical pendulum which is used for the torsion angles in lieu of a harmonic oscillator, allows for larger amplitude motions and multiple equilibrium states, which is consistent with their more flexible character.

The second contribution (1.12) involves the 6-12 Lennard-Jones potential that approximates the interaction between a pair of neutral atoms; the form is chosen for computational efficiency. Finally, we have the Coulomb interaction. In practice, long-range interactions (1.12) are cut off beyond a distance around 10 Ångström, again for computational efficiency. The "ideal" values of the various parameters are usually determined by a process of optimisation, using comparative simulations. For parameter fine tuning, one may use very short peptides that have accurately known experimental structures. Such structures can be found for example in the Engh-Huber library [12].

In a full all-atom MD simulation one solves the Newton's equation of motion with (1.11), (1.12) in an environment of water which in a full all-atom approach is also treated explicitly. We note that *e.g.* the  $r^{-12}$  term in (1.12) models short range Pauli repulsion due to overlapping electron orbitals, and the  $r^{-6}$  term emerges from long range van der Waals interactions. Thus these terms have a quantum mechanical origin, and the proper interpretation of the ensuing Newton's equation is not in terms of a classical equation but in terms of a semi-classical one.

A MD simulation solves the Newton's equation iteratively, with a time-step  $\Delta\tau$ . This time-step should be short in comparison to the shortest time scale  $\Delta t_{min}$ , that characterises the fastest atomic level oscillations. The ratio of the two defines a dimensionless expansion parameter. For good convergence of the iterative, discretised Newton's equation we should have

$$\frac{\Delta\tau}{\Delta t_{min}} \ll 1 \quad (1.13)$$

This implies that  $\Delta\tau$  should be no more than a few femto-seconds: The modelling of protein folding in an all-atom MD is conceptually a weak-coupling expansion in terms of the dimensionless ratio (1.13).

*Research project: The Newton's equation for mathematical pendulum*

$$\ddot{\omega} = V \sin \omega$$

*is integrable. Its naive discretisation*

$$\ddot{\omega} \rightarrow \frac{1}{\epsilon^2}(\omega_{n+1} - 2\omega_n + \omega_{n-1})$$

*yields the so-called standard map [34]*

$$\omega_{n+1} - 2\omega_n + \omega_{n-1} = \epsilon^2 V \sin \omega$$

*which is not integrable. However, an integrable discretisation of the mathematical pendulum is known. See for example Chapter VIII of ref. [35]. Find which one describes protein folding more accurately.*

## 1.9 All-atom simulations

Enormous computational resources have been developed and dedicated to solve the *protein folding problem* [3, 4]. From the point of view of molecular dynamics this amounts to a numerical simulation of the all-atom time evolution in a protein, from a random chain initial condition to the natively folded conformation using a force field such as (1.11), (1.12). For example, the *Blue Gene* family of supercomputers was originally designed by IBM to address the problem of protein folding and gene development, which explains the name. Subsequently special purpose computers have been constructed to address the folding problem, at all-atom level of scrutiny. Thus far the most powerful is the *Anton* supercomputer, built by D.E. Shaw Research [36–38]. In the case of relatively short proteins, *Anton* can produce a few microseconds of *in vitro* folding trajectory per day *in silico* [37]; this is about 3-4 orders of magnitude more than a Blue Gene can achieve. In a series of MD simulations of 12 fast-folding proteins, from chignón with 10 residues to genetically modified  $\lambda$ -repressor with 80 residues, and with each protein capable of folding within a number of micro seconds *in vitro*, *Anton* was able to produce dynamical trajectories that reproduced the experimentally observed folded structures, in some examples with an impressive precision [38]. At the moment, these results set the benchmark for all-atom protein folding simulations. But despite the encouraging results obtained by *Anton*, several issues remain to be overcome before proteins can be routinely folded at all-atom level, starting from a knowledge of the amino acid sequence only. We name a few, as a challenge for future research:

- For the majority of proteins it takes much longer than a millisecond or so to fold. For example myoglobin, which is probably the most widely studied protein and that we shall fold in the sequel, needs about 2.5 seconds *in vitro* to reach its native state when it starts from a random chain initial condition. Thus, it would take at least 1.000 years to simulate the folding of myoglobin at the level of all-atoms, using presently available computers.
- In an all-atom MD simulation with explicit water, an increase in the number of water molecules quickly exhausts the capacity of presently available computers. For example, in the case of the 80 residue  $\lambda$ -repressor mutant simulation using *Anton*, only around 11.000 explicit water molecules could be included. This should be contrasted to the physiological conditions: The normal pH of blood plasma is around 7.4. Since pH is defined as the  $\log_{10}$  of the reciprocal of the hydrogen ion activity in a solution, this translates to an average of one proton per  $10^{7.4}$  water molecules. Protein folding is strongly affected by pH; proteins have different natively folded states, at different pH values. Thus, it remains a formidable task to describe physiologically relevant pH environments in a truly all-atom manner.
- All-atom force fields utilise a quadratic, harmonic oscillator approximation around the ideal values of the bond lengths and angles (1.11); mathematical pendulum in the case of torsional angles. As long as the atomic fluctuations around the ideal values remain very small, this is a decent approximation. But whenever the atoms deviate from their ideal positions more than "just a little", higher order non-linear corrections are inevitably present and can not be ignored. The existing all-atom force fields are

not designed to account for this. The force fields are not built to describe protein conformations in a realistic manner, whenever the lengths and angles are not very close to their ideal values.

## 1.10 Thermostats

*This section describes a technical aspect, that is not needed in the rest of the lectures. We add this section as we feel it addresses a highly important yet still open theoretical issue that needs to be addressed by any all-atom modelling approach.*

Finally, we have the theoretically highly interesting problem of *thermostatting*: An all-atom simulation solves the Newton's equation. As a consequence energy is conserved and we have a microcanonical ensemble. But in a living cell the energy is not conserved, instead temperature is fixed. Accordingly proteins in living organisms should be described in terms of a canonical ensemble. One needs to convert the microcanonical ensemble which is described by the all-atom Newton's equation, into a canonical one. To achieve a conversion, one adds *thermostats* to the system. A thermostat models an environment which maintains its own temperature constant while interacting with the system of interest: We refer to [39] for a detailed description of thermostats.

The Langevin equation is an example of a thermostat which is well grounded in physical principles. In the case of uniform damping we write it as follows,

$$\ddot{\mathbf{x}}_i = -\nabla_i E(\mathbf{x}) - \lambda \dot{\mathbf{x}}_i + \mathbf{F}_i(t) \quad (1.14)$$

$$\langle \mathbf{F}_i(t) \rangle = 0 \quad \& \quad \langle \mathbf{F}_i(t) \cdot \mathbf{F}_j(s) \rangle = \lambda k_B T \delta_{ij}(t-s) \quad (1.15)$$

The derivation of the Langevin equation assumes two sets of variables, *a.k.a.* particles: There are light, small particles that are fast. And there are heavy particles that are slow. The Langevin equation describes the dynamics of the latter, in the limit where the ensuing particles are much slower and heavier than the small and fast ones. The derivation is based on standard arguments of statistical physics. Thus, the Langevin equation is *a priori* a well grounded and rigorous method to introduce temperature into a Newtonian system.

In the case of all-atom MD the Langevin equation can not be used. There are no small and fast variables around. The oscillating atoms are themselves the small and fast variables. Moreover, from a conceptual point of view the presence of a white noise (1.15) *de facto* converts the ensuing numerical algorithm into a Monte Carlo process, albeit an elaborated one.

Many alternatives to Langevin thermostat have been introduced. An example is the Gaussian thermostat [39]. Unlike Langevin's, it is *deterministic*. Instead of small and fast background variables, one couples the variables  $\mathbf{x}_i$  of interest to explicit thermostat variables  $\mathbf{X}_k$ , with equations of motion

$$m_i \ddot{\mathbf{x}}_i = -\nabla_i E(\mathbf{x}) - \nabla_i \mathcal{E}(\mathbf{x}, \mathbf{X}) \quad (1.16)$$

$$M_k \ddot{\mathbf{X}}_k = -\nabla_k \mathcal{U}(\mathbf{X}) - \nabla_k \mathcal{E}(\mathbf{x}, \mathbf{X}) - \alpha_k \dot{\mathbf{X}}_k \quad (1.17)$$

The thermostatting effect is modelled by the last term in (1.17); the  $\alpha_k$  is determined by subjecting the auxiliary variables to the non-holonomic constraint

$$\frac{M_k}{2} \dot{\mathbf{X}}_k^2 = \frac{3}{2} k_B T$$

$$\Rightarrow \alpha_k = \left( \frac{3}{2} k_B T \right)^{-1} \left[ \frac{M_k}{2} \dot{\mathbf{X}}_k^2 + \dot{\mathbf{X}}_k [\nabla_k \mathcal{U}(\mathbf{X}) + \nabla_k \mathcal{E}(\mathbf{x}, \mathbf{X})] \right]$$

for each of the thermostat variable. The disadvantage of a Gaußian thermostat is in the lack of a Hamiltonian character in the equations of motion (1.16), (1.17).

A Hamiltonian, albeit singular, thermostating has been proposed by Nosé and Hoover [40–43]. Their thermostat is probably the most widely used in the context of all atom protein folding simulations. In the simplest variant the all-atom phase space is extended by a single *ghost* particle with a singular, logarithmically divergent potential that provides the temperature for all the rest<sup>3</sup>. The singular character of the potential introduces an inexhaustible heat reservoir, in essence.

Following [44] we consider the toy-model case of a single canonical degree of freedom  $(p, q)$  in the presence of a single Nosé-Hoover thermostat degree of freedom  $(P, Q)$ . The classical action is [40–43]

$$S = \int_{-T}^T dt \left\{ p\dot{q} + P\dot{Q} - \frac{p^2}{2mQ^2} - V(q) - \frac{P^2}{2M} - \frac{1}{\beta_0} \ln Q \right\} \quad (1.18)$$

We may assume that  $V[q]$  has the double-well profile

$$V[q] = \lambda(q^2 - m^2)^2 \quad (1.19)$$

We are interested in the tunnelling amplitude between the two minimum energy configurations  $q = \pm m$ ,

$$\langle +m, T | -m, -T \rangle = \iint_{q(-T)=-m}^{q(+T)=+m} [dp][dq] e^{iS} \quad (1.20)$$

The integration over  $p$  is Gaußian but yields a Jacobian factor that depends on  $Q$ . This Jacobian has the same functional form as the last term in (1.18), thus it can be absorbed by a redefinition (renormalisation) of  $\beta_0 \rightarrow \beta$ . As usual, we evaluate the transition amplitude using Euclidean (imaginary) time formalism, obtained by sending  $t \rightarrow it$ . The Euclidean action is

$$S = \int_{-T}^T dt \left\{ \frac{1}{2} Q^2 \dot{q}^2 + V[q] + \frac{1}{2} Q^2 \dot{P}^2 + \frac{1}{\beta} \ln Q \right\} \quad (1.21)$$

and we search for a finite action instanton trajectory that connects the two states  $q = \pm m$ ; note that the continuation to imaginary time "inverts" the potential term, as shown in Figure 1.12. The instanton is a solution to the equations of motion

<sup>3</sup>We remark that this ghost particle is a little like a Higgs particle that gives the mass for other particles in sub-atomic physics. Except that instead of mass it gives temperature, and it can not be observed.

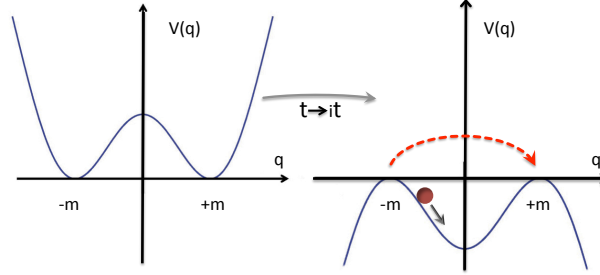


**Fig. 1.12** Analytic continuation to Euclidean time has the effect of inverting the potential  $V(q)$ . The instanton is a trajectory which starts at (Euclidean) time  $-T$  from the local maximum at  $q = -m$  and reaches the local maximum at  $q = +m$  at time  $+T$ , as shown in the Figure on right.

$$Q^2 q_{tt} = V_q - 2Q Q_t q_t \simeq V_q - \gamma q_t \quad (1.22)$$

$$Q Q_{tt} = Q^2 q_t^2 + \frac{1}{\beta} \quad (1.23)$$

Note how the coupling between  $q$  and the thermostat variable  $Q$  gives rise to an effective friction-like coefficient  $\gamma(t)$ .

We first consider the case where the thermostat field  $Q$  is absent. This amounts to setting  $Q \equiv 1$  in (1.21), (1.22) and removing (1.23), leaving us with the equation

$$q_{tt} = V_q = 4\lambda q(q^2 - m^2)$$

By adjusting the initial velocity we conclude that a solution exist which starts from  $q = -m$  at time  $-T$ , and ends at  $q = +m$  at time  $+T$ . This solution is the instanton that gives rise to a finite tunneling amplitude between  $\pm m$ ; in the limit  $T \rightarrow \infty$  the instanton has the familiar double-well topological soliton profile

$$q(t) = m \tanh(\sqrt{2\lambda} m(t - a)) \quad (1.24)$$

Now suppose the thermostat field is present. We first consider a scenario, where at  $\pm T$  the system reaches a stationary state where  $q = \pm q_0 \neq \pm m$ . Since the action (1.21) should remain finite as  $T \rightarrow \infty$ , we arrive at the Gibbsian relation

$$Q(T) \xrightarrow{T \rightarrow \pm\infty} Q_{\pm} = e^{-\beta V[q_{\pm}]} \quad (1.25)$$

This proposes that  $\beta$  is indeed the Boltzmannian temperature factor, when positive.

Next, we integrate (1.23) and then take the limit  $T \rightarrow \infty$ ; since the Euclidean action should be finite, we may assume that  $Q_t$  should vanish as  $T \rightarrow \infty$  which removes the surface term. We find

$$\int_{-\infty}^{\infty} dt \{Q_t^2 + Q^2 q_t^2\} = - \int_{-\infty}^{\infty} dt \frac{1}{\beta} \quad (1.26)$$

For a non-trivial tunnelling configuration and with a finite Euclidean action (1.21) the integral on the left-hand-side of (1.26) should be finite and non-vanishing. But

since the *l.h.s.* is manifestly non-negative, the Boltzmann temperature factor  $\beta$  can not be positive as it should. Thus we conclude that the presence of the thermostat field suppresses tunnelling. We note that a suppression of tunneling amplitude by Nosé-Hoover thermostat in the case of double-well potential has been observed in numerical simulations [43].

Proteins regularly need to tunnel over various different potential barriers in their presumably highly rugged energy landscape, when proceeding from a random initial configuration to the natively folded state. Thus we suspect that simulations using Nosé-Hoover thermostats can cause complications whenever we have a protein for which we can expect that the folding pathway goes thru various intermediates and molten globules.

*Research project: Investigate how the suppression of tunneling amplitudes in the case of a properly modified Nosé-Hoover thermostat could be avoided.*

Other kind of thermostats have also been introduced, in particular we mention the Berendsen thermostat [45]. These thermostats that are often convenient in numerical simulations, are designed to approach canonical ensembles in a limit. But they commonly lack a Hamiltonian interpretation *i.e.* are non-physical, and thus the physical interpretation of the results is not there. While this might not be an issue when the goal is *simply* to find a local energy minimum of an all-atom force field such as (1.11), (1.12), a non-physical thermostat can not be used to model the dynamics of proteins.

### 1.11 Other Physics-based approaches:

The all-atom approaches where the discretised Newton's equation is solved iterately, are conceptually weak coupling expansions in the dimensionless parameter (1.13). To describe the folding of most proteins, one needs to be able to extend this expansion and ensure its convergence, over some fifteen orders of magnitude or even more. From the perspective of sub-atomic Physics, this is like extending perturbative Standard Model calculations all the way to Planck scale.

Several approaches have been developed, with the goal to introduce an expansion parameter that corresponds to a time scale which is clearly larger than the femtosecond scale. Such *coarse-grained* force fields average over the very short time scale atomic fluctuations: If the denominator in (1.13) can be increased, so can the numerator, and it becomes possible to develop expansions which reach longer *in vivo* time scales with no increase in the *in silico* time. In practice, a carefully crafted coarse grained force field can cover up to around three orders of magnitude longer folding trajectories than all-atom approaches, while still maintaining a good overall quality. Here we mention in particular UNRES as an example of such a carefully crafted coarse grained force field [46–48]. See the homepage

<http://www.unres.pl/>

Finally, we comment on the various versions of the Gō model [49] and the closely related elastic (Gaussian) network models [50]. These approaches were historically important, to gain insight to protein folding at a time when the power of computers was insufficient for any kind of serious all-atom folding simulations. In these models the

folded configuration is presumed to be known; the individual atomic coordinates of the folded protein chain appear as an input. A simple energy function is then introduced, tailored to ensure that the known folded configuration is a minimum energy ground state. In the Gō model the energy could be as simple as a square well potential which is centered at the native conformation. In elastic network models the atoms are connected by harmonic oscillators, with energy minima that correspond to the natively folded state. Since the positions of all the relevant atoms appear as parameters in these models, they contain more parameters than unknown and thus no predictions can be made: From the point of view of a system of equations, these models are over-determined. In any *predictive* energy function the number of adjustable parameters must remain *smaller* than the number of independent atomic coordinates. Otherwise, no predictions can be made, and no physical principles can be tested.

## 2

# Bol'she

---

In 1972 Anderson wrote an article [2] entitled *More is different* that has been inspirational to many. In particular, he argued for the importance of emergent phenomena. But the call for *Bol'she* is already present in Schrödinger's 1944 book:

*... living matter, while not eluding the 'laws of physics' as established up to date, is likely to involve 'other laws of physics' hitherto unknown, which, however, once they have been revealed, will form just as integral a part of this science as the former.*

However, Anderson makes a *crucially* important point that can not be found in Schrödinger's book. Anderson's article has this point even as a subtitle: *Broken symmetry and the nature of the hierarchical structure of science*. Anderson realised that in order for emergent phenomena to give rise to structural self-organisation, one needs a symmetry which becomes broken.

We have already pointed out that in the case of proteins a broken symmetry is present. Individual amino acids can be either left-handed chiral or right-handed chiral, equally. But for some reason, living matter is built almost exclusively from amino acids that are left-handed chiral. We note that, apparently as a consequence, protein chains are predominantly chiral with right-handed helicity.

### 2.1 The importance of symmetry breaking

Consider a fluid dynamical system such as water, the atmosphere, or any other scenario that can be described by the Navier-Stokes or Euler equation or their many descendants. These are fundamentally atomic systems, but with an enormous number of constituents. Their macroscopic properties are governed and often with a very high precision, by the properties of a local order parameter which computes the fluid velocity. Structures such as vortices and tornadoes, and solitonic waves like the one that emerges from the Korteweg - de Vries equation, are all described by a solution that breaks an underlying symmetry.

A fluid dynamical vortex line is a familiar example of a highly regular collective state of individual atoms, with a topological character. It is an example of an emergent structure: At the atomic level of scrutiny, the individual atoms and molecules that constitute the vortex are subject to random, brownian thermal motion. By following a single individual water molecule you can not really conclude whether a vortex is present. The vortex materialises only at the macroscopic level, when the individual haphazard atomic motions become collectively self-organised into a regular pattern.

It would be incomprehensible to construct a macroscopic vortex line such as a tornado in atmosphere from purely atomic level considerations, even in principle: A vortex



is an example of a soliton, and solitons can not be constructed simply by adiabatically building up individual atomic level interactions as small perturbations around a ground state which consists of free individual atoms. A (topological) soliton emerges when non-linear interactions combine elementary constituents into a localised collective excitation that is stable against small perturbations and cannot decay, unwrap or disentangle.

## 2.2 An optical illusion

We start to describe the importance of symmetry breaking at an intuitive level. We consider a simple optical illusion, *not* a physical example. But it nevertheless demonstrates how *Bol'she* gives rise to a symmetry that becomes broken, and the illusion of breaking symmetry leads to the formation of structure, in our eyes.

We then proceed to consider two physically relevant examples, where a very similar broken symmetry is present. But now in a physically relevant fashion. Most importantly, each of the two examples we present describes a simple physical scenario that shares many features with proteins.

In Figure 2.1 we have two sets of cubes. On the left we have two individual cubes, and on the right there are more cubes. If one looks at the cubes on the right, one should be able to visualise some order. For example light grey steps that come down, from the left. Now rotate the Figure, slowly. When one keeps ones eyes focused on the two individual cubes on the left, nothing really happens besides an overall rotation of the two cubes. But if one instead focuses on the set of cubes on right, one should observe a rapid transition: There is a point where the direction of the steps changes, abruptly, so that after a rotation by 180 degrees we still have the same light grey steps, still coming down from the left.

The system on the right is *Bol'she*, with a discrete  $\mathbb{Z}_2$  symmetry under a rotation by 180 degrees. There are two ground states, and our mind chooses one, thus breaking the symmetry. In fact, the scenario is very much like that in Figure 1.12, there are two identical ground states. In this sense Anderson's *Bol'she* is present in Figure 2.1. No similar optical illusory effect is observed when the two individual cubes on the left are rotated.

We now proceed to describe two physical examples where a similar kind of  $\mathbb{Z}_2$  symmetry becomes broken, with equally dramatic *physical* - not illusory - consequences.

## 2.3 Fractional charge

Polyacetylene in *trans* conformation is like a simplified protein. Figure 2.2 a) shows the structure. There is a "backbone" that consists entirely of carbon atoms, and at each carbon atom there is a "side chain" with a single hydrogen. Much like in a protein, but simpler. In Figure 2.2 b) we depict the (*trans*) polyacetylene chain by combining each (CH) unit into a single vertex. The double line describes the  $\sigma$ -bond and the single line is the  $\pi$ -bond, between two consecutive C atoms. Due to a Peierls instability the asymmetry of the chain causes the ground state to be doubly degenerate. The free energy acquires the double-well profile that we have depicted in Figure 1.12. The two ground states are related to each other by a  $\mathbb{Z}_2$  reflection (parity) symmetry of the polyacetylene chain about a (CH) site, which exchanges the  $\sigma$ -bonds and the  $\pi$ -bonds.

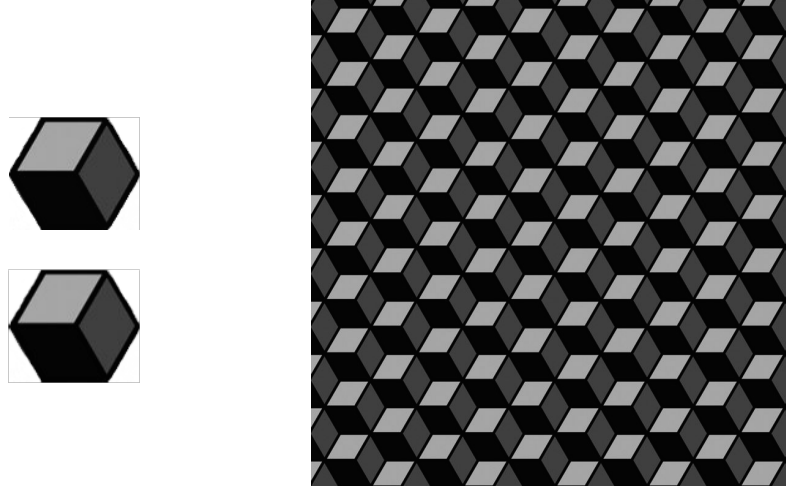


**Fig. 2.1** Rotate the figure, slowly, by 180 degrees. When you focus your eyes on the two individual cubes on the left, nothing much happens. However, if you focus on the set of cubes on the right, you see an abrupt effect like a phase transition between two different but identical ground states; we have a  $\mathbb{Z}_2$  symmetry that has become broken by visual perception.

When we choose one of the ground states, we break the symmetry. But we may introduce domain walls, that interpolate between two different ground states. In Figure 2.2 c) we show an example. In this Figure we have two domain walls. Each interpolates between two different ground states; between the two domain walls we have a region where the  $\sigma$ -bonds and  $\pi$ -bonds have become interchanged. Quantitatively, in terms of the double well potential shown in Figure 1.12, each of the two domain walls correspond to a topological soliton (instanton) profile (1.24).

We now argue that we have *Bol'she* which makes things different: The chain in Figure 2.2 c) is obtained from the chain in Figure 2.2 b) by removal of a single electron. There are 15 bonds in the Figure 2.2 b) and 14 in the Figure 2.2 c). The removal of a single electron converts a double bond into a single bond, and we have simply moved the bonds around to make the two identical domain walls. Since the structures in Figure 2.2 b) and in Figure 2.2 c) differ from each other only by the removal of a single bond and since the two domain walls are identical, related to each other by parity, the two domain walls must share equally the quantum numbers of the missing bond: The two domain walls have electric charge half, each.

This phenomenon of fermion number (charge) fractionalisation demonstrates how Anderson's *Bol'she* really makes a difference: Such exotic quantum number assignments could never be obtained simply by linearly superposing an integer number of initially non-interacting electrons and holes adiabatically, in a continuous manner, into a weakly interacting system: *A charge half state simply can not be made by combining together any finite number of particles with an integer charge.* Unless something *Bol'she* is involved.

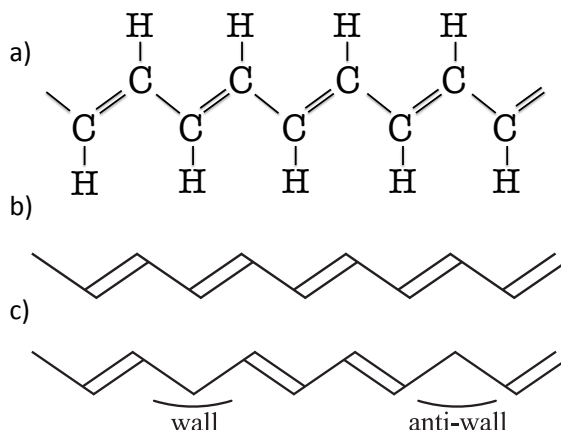


**Fig. 2.2** a) The *trans* polyacetylene. b) One of the two degenerate ground states in a *trans*-polyacetylene chain. The other ground state is obtained by a reflection that interchanges the double bonds and the single bonds. c) A state of a *trans*-polyacetylene chain with one of the double bonds converted into a single bond and then transported to form two domain walls carrying fractional electric charges.

*Fine points:* A bond line in a polyacetylene corresponds to two electrons, one with spin up and the other with spin down. Thus an isolated domain wall must have a net electric charge which is equal in magnitude but opposite in sign to that of a single electron. But since the spins of the electrons that have been removed are paired, the domain wall carries no spin. This unusual spin-charge assignment has been observed experimentally and it constitutes the essence of fermion number fractionalisation [51–53] that gives rise to electric conductivity along the polyacetylene. In the absence of the spin doubling we would observe a domain wall that carries half the electric charge of one electron. Note that if we add a single electron to a domain wall, we obtain a state which is charge neutral but carries the spin of the electron. Alternatively, if we remove a single electron from a domain wall we obtain a state with spin one-half and a charge that equals (minus) twice that of the electron. Neither of these states are possible, without *Bol'she*.

## 2.4 Spin-charge separation

We shall eventually argue that proteins are very much like one dimensional spin-chains; the side chains are akin spin variables along the backbone. Thus, our second example is a one dimensional spin chain. For conceptual clarity we may assume that the spin variables are single electrons (or maybe protons like  $H^+$ ). We assume that the background lattice prefers a ground state which is an antiferromagnetic Néel state where all the spins point into an opposite direction from their nearest neighbours.

Furthermore, we assume that in the ground state all the sites have single occupancy, and that there is a very strong repulsive force between the electrons which prevents a double occupancy. Such a ground state is a Mott insulator, and we have depicted the structure in Figure 2.3. As in the case of a polyacetylene, the ground state is doubly

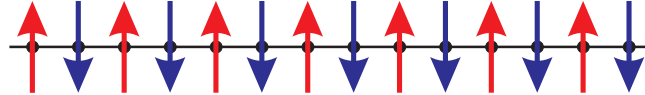


**Fig. 2.3** One the two degenerate ground states in a Néel antiferromagnet, with alternating spin directions along a one dimensional lattice of electrons. The  $\mathbb{Z}_2$  symmetric ground state is obtained by reversing the direction of every spin.

degenerate: The  $\mathbb{Z}_2$  symmetry transformation operates by reversing the direction of the spin at every single lattice site. By choosing one of the two ground states, we break the  $\mathbb{Z}_2$  symmetry.

If we reverse the direction of a single spin along the chain, we form a localized configuration with three parallel neighboring spins; see Figure 2.4 a). By successively

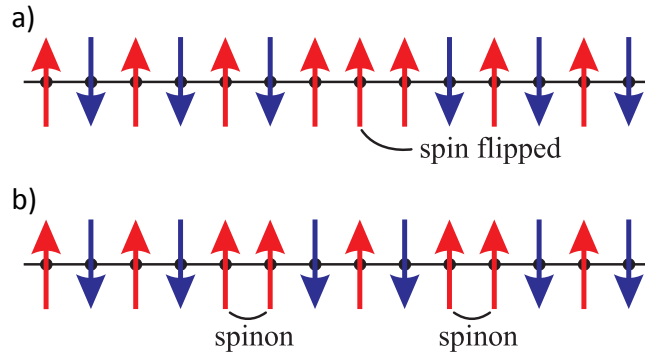


**Fig. 2.4** a) The same as in Figure 2.3 but with the spin of only one electron reversed. b) The state of Figure a) is decomposed into two domain walls representing the spinons.

reversing the direction of neighboring spins but without changing the total spin we can decompose this configuration into two separate domain walls, each consisting of two parallel spins. These domain walls interpolate between the two ground states of the spin chain, as shown in Figure 2.4 b). Since the lattices in Figure 2.4 a) and b) differ from each other only by the flip of a single spin, the total change in the spin between the two lattices is one. The two domain walls in Figure 2.4 b) are also identical. Thus each must have a spin equal to one-half.

Since we have made the two domain walls without adding or removing any electrons, each of them must be charge neutral. We conclude that the domain walls are *spinons*, they describe the same spin degree of freedom as a single electron but with no charge [54]. The two domain walls interpolate between the two different ground

states of the antiferromagnetic chain, very much like the domain walls in the case of polyacetylene.

Now we consider the same antiferromagnetic lattice but with one of the electrons removed as shown in Figure 2.5. This corresponds to an underdoped case, we have a

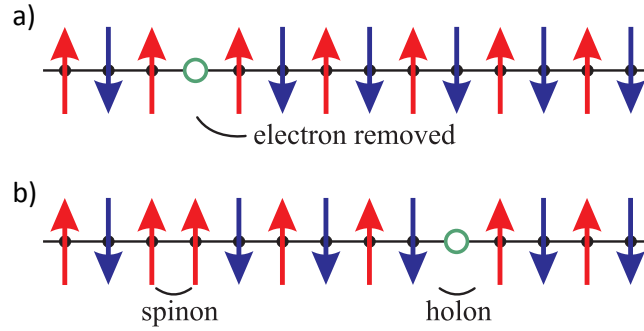


**Fig. 2.5** a) Spinon (left) and chargin (right) states in the underdoped state. b) The state of Figure a) is decomposed into two domain walls representing the spinons.

hole in the spin chain. When we move the hole to the right we arrive at the situation depicted in Figure 2.5 b). In addition of the hole we have here another domain wall which is similar to the two domain walls that we have in Figure 2.4 b). This domain wall is a spinon, it has spin one-half but carries no charge. Since we have removed one electron and since the spinon does not carry charge, the hole must carry a charge which is opposite to that of one electron. But no spin is available for this hole, it describes a spinless *holon*.

The ARPES experiment at Lawrence Berkeley Laboratory has confirmed that such spinons and holons do exist, they have been observed in a one dimensional copper oxide ( $\text{SrCuO}_2$ ) wire [55].

Note that in Figure 2.5 a) the two spins on the left and on the right of the hole are parallel with each other but in Figure 2.5 b) the two spins are opposite to each other. This confirms that like the spinon, the spinless holon is a domain wall that interpolates between the two different ground states of the chain.

Finally, in Figure 2.6 a) we have added a single electron to the lattice. This example is of particular conceptual interest since it allows us to directly address what happens to a (pointlike) electron when it enters the antiferromagnetic environment: The presence of the electron introduces a single site with a double bond ( $\uparrow\downarrow$ ). The chain is now over-doped. As before we transport the double filled state, e.g. to the right so that we arrive at the situation depicted in Figure 2.6 b). Note that due to Pauli exclusion the transport occurs so that we move alternatively either a spin-up or a spin-down state one step to the right. The final configuration shown in Figure 2.6 b) describes two separate domain walls that both interpolate between the two distinct ground states of the spin chain. One of these domain walls is again a spinon. The other one is a *doublon*. Since one electron has been added and since spinon has spin but no charge,

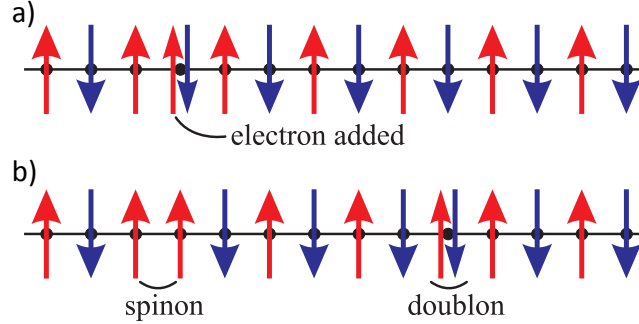


**Fig. 2.6** a) The Néel state with one electron added (overdoped case). b) Spinon (left) and doublon (right) states in the overdoped state.

we conclude that the doublon does not have any spin but it carries the entire charge of one electron. The charge of the doublon is opposite to that of the holon.

The two examples we have discussed, fermion number fractionalisation and spin charge separation, make it plain and clear how much difference *Bol'she* can do: It would be impossible to make states with the spin of an electron but no charge, or states with the charge of an electron but no spin, simply by superposing an integer number of non-interacting electrons and then adiabatically switching on their mutual interactions. For states with such exotic quantum numbers we need to have an environment with a symmetry that has become broken.

## 2.5 All-atom is Landau liquid

The Landau (Fermi) liquid is a paradigm on which much of our understanding of many-body systems like metals is based. This paradigm states, that in a physical system with a large number of atoms, each atom retains its individual integrity. The properties of a material system which is described by a Landau liquid, can be understood by superposing its individual constituents in a weak coupling expansion around a given ground state. In particular a Landau liquid which is made of electrons and protons can only have spin and charge assignments which are obtained by superposing the individual spins and charges. This is the case when the properties of the system can be understood using the notion of adiabaticity: We imagine that we start from an initial condition where the elemental constituents have no mutual interactions. The interactions are then turned on, adiabatically, in a continuous manner. Accordingly the ground state of the original non-interacting system becomes continuously deformed into the ground state of the interacting system.

The two examples that we have described, polyacetylene and antiferromagnetic spin chain, show that the Landau liquid paradigm is not a universal one. In a Landau liquid system it would be impossible to have states with exotic quantum numbers such as an electric charge which is half of that of a single electron. The Landau liquid paradigm can fail whenever we have emergent structures that display symmetries which become broken. In such scenarios there are often collective excitations like topological solitons

which can not be built simply by adding together small adiabatic perturbations around a ground state of non-interacting elemental constituents.

The all-atom description (1.11), (1.12) of protein force field implicitly assumes the Landau liquid paradigm. According to (1.11), (1.12) the individual atoms oscillate around their ideal values, under the influence of a potential which is either a harmonic oscillator or a mathematical pendulum. The Lennard-Jones and Coulomb potentials introduce continuously evolving deformations around the ideal atomic positions, in a manner that can be modelled by a weak coupling expansion of the iterative Newton's equation in powers of (1.13); in practical simulations these long range interactions are tuned off, beyond a distance around 10 Ångström.

It remains to be seen whether an all-atom Landau liquid description of proteins breaks down. But the basal ingredient, that of a broken  $\mathbb{Z}_2$  symmetry which also appears in our examples of polyacetylene and antiferromagnetic spin chain, is certainly present: The amino acids are left-handed chiral, and as a consequence proteins that constitute live matter prefer right-handed helicity along their backbone.

### 3

## Strings in three space dimensions

---

*Thus we have come to the conclusion that an organism and all the biologically relevant processes that it experiences must have an extremely 'many-atomic' structure and must be safeguarded against haphazard, 'single-atomic' events attaining too great importance. (E. Schrödinger)*

We start our search of broken symmetry and the ensuing *Bol'she* that makes us alive, by considering differentiable (class  $\mathcal{C}^3$ ) strings in  $\mathbb{R}^3$ .

### 3.1 Abelian Higgs Model and the limit of slow spatial variations

The Abelian Higgs Model (AHM) is the paradigm framework to describe vortices as solitons. Solitonic vortices are important to many physical phenomena, from cosmic strings in Early Universe to type-II superconductors. In particular, the Weinberg-Salam model of electroweak interactions with its Higgs boson is a non-Abelian extension of AHM.

The AHM involves a single complex scalar (Higgs) field  $\phi$  and a vector field  $A_i$ . These fields are subject to the U(1) gauge transformation

$$\begin{aligned}\phi &\rightarrow e^{ie\vartheta}\phi \\ A_i &\rightarrow A_i + \partial_i\vartheta\end{aligned}\tag{3.1}$$

where  $\vartheta$  is a function, and  $e$  is a parameter. The standard AHM Hamiltonian is

$$\mathcal{H} = \frac{1}{4}G_{ij}^2 + |(\partial_i - ieA_i)\phi|^2 + \lambda(|\phi|^2 - v^2)^2\tag{3.2}$$

where

$$G_{ij} = \partial_i A_j - \partial_j A_i$$

When the space dimension  $D$  is odd, a Chern-Simons term ( $ChS$ ) can be added to (3.2). Explicitly,

$$\begin{aligned}D = 1 : \quad ChS &\sim A \\ D = 3 : \quad ChS &\sim AdA \\ D = 5 : \quad ChS &\sim AdAdA \\ &etc.\end{aligned}\tag{3.3}$$

The Chern-Simons term is the paradigm way to break parity.

In a material system (3.2), (3.3) is the Kadanoff-Wilson energy in the limit where the fields have slow spatial variations [18,19]. To describe this limit, we start from the



full free energy of a material system which is based on the AHM field multiplet; we denote it

$$\mathcal{F}(\phi, A_i)$$

This free energy is in general a non-local functional of the field variables. But it must be gauge invariant. Thus, it can only depend on manifestly gauge invariant combinations of the fields such as

$$|\phi|^2, \quad |(\partial_i - ieA_i)\phi|^2, \quad \dots$$

Consider the limit where the length scale that is associated to spatial variations of the field variables becomes very large in comparison to other characteristic length scales of the system. In this limit we can expand the free energy in powers of the gauge covariant derivatives of the fields. The expansion looks like this [56]:

$$\mathcal{F}(\phi, A_i) = V(|\phi|) + Z(|\phi|) |(\partial_i - ieA_i)\phi|^2 + ChS(A) + W(|\phi|) G_{ij}^2 + \dots \quad (3.4)$$

The leading term is called the effective potential. The higher derivative terms are multiplied by functions  $Z(|\phi|)$ ,  $W(|\phi|)$  etc.

The AHM energy (3.2), (3.3) constitutes the leading order non-trivial contribution to (3.4), in powers of fields and their covariant derivatives.

We introduce a set of new variables  $(J_i, \rho, \theta)$ , obtained from  $(A_i, \phi)$  by the following change of variables

$$\begin{aligned} \phi &= \rho \cdot e^{i\theta} \\ A_i \rightarrow J_i &= \frac{i}{2e|\phi|^2} [\phi^* (\partial_i - ieA_i)\phi - c.c.] \end{aligned} \quad (3.5)$$

We can introduce these new variables whenever  $\rho \neq 0$ . Note that both  $\rho$  and  $J_i$  are gauge invariant under the gauge transformation (3.1). But

$$\theta \rightarrow \theta + \vartheta$$

When we write (3.2), (3.3) in terms of these new variables (3.5), we have

$$\mathcal{H} = \frac{1}{4} \left( J_{ij} + \frac{2\pi}{e} \sigma_{ij} \right)^2 + (\partial_i \rho)^2 + \rho^2 J_i^2 + \lambda (\rho^2 - \eta^2)^2 + ChS \quad (3.6)$$

where

$$J_{ij} = \partial_i J_j - \partial_j J_i$$

and

$$\sigma_{ij} = \frac{1}{2\pi} [\partial_i, \partial_j] \theta \quad (3.7)$$

We observe that (3.6) involves only variables that are manifestly  $U(1)$  gauge invariant. In particular, unlike in the case of (3.2), in (3.6) the local gauge invariance is entirely removed, by a change of variables [57].

The term  $\sigma_{ij}$  is a string current. It has a Dirac  $\delta$ -like support which coincides with the world-sheet of the cores of vortices. When (3.6) describes a finite energy vortex, (3.7) subtracts a singular string contribution that appears in  $J_{ij}$ . Since  $J_i$  is singular in

the presence of a vortex line, it makes a divergent contribution to the third term in the *r.h.s.* of (3.6). But the divergence becomes removed, provided the density  $\rho$  vanishes on the world-sheet of the vortex core. Thus the vanishing of  $\rho$  along a string-like line in space is a *necessary* condition for the presence of finite energy vortex lines.

### 3.2 The Frenet Equation

Proteins are string-like objects. Thus, to understand proteins we need to develop the formalism of strings in  $\mathbb{R}^3$ , at least to some extent.

The geometry of a class  $\mathcal{C}^3$  differentiable string  $\mathbf{x}(z)$  in  $\mathbb{R}^3$  is governed by the Frenet equation, described widely in elementary courses of differential geometry. The parameter  $z \in [0, L]$  where  $L$  is the length of the string in  $\mathbb{R}^3$ . We can compute the length from

$$L = \int_0^L dz \|\mathbf{x}_z\| = \int_0^L dz \sqrt{\mathbf{x}_z \cdot \mathbf{x}_z} \equiv \int_0^L dz \sqrt{g}. \quad (3.8)$$

Here we recognise the static version of the standard Nambu-Goto action, with generic parameter  $z \in [0, L]$ . We re-parametrize the string to express it in terms of the arc-length  $s \in [0, L]$  in the ambient  $\mathbb{R}^3$ , by the change of variables

$$s(z) = \int_0^z \|\mathbf{x}_z(z')\| dz'$$

In the following we use the arc-length parametrisation, exclusively. We consider a single, open string that does not self-cross. We introduce the unit length tangent vector

$$\mathbf{t} = \frac{d\mathbf{x}(s)}{ds} \equiv \mathbf{x}_s \quad (3.9)$$

the unit length bi-normal vector

$$\mathbf{b} = \frac{\mathbf{x}_s \times \mathbf{x}_{ss}}{\|\mathbf{x}_s \times \mathbf{x}_{ss}\|} \quad (3.10)$$

and the unit length normal vector,

$$\mathbf{n} = \mathbf{b} \times \mathbf{t} \quad (3.11)$$

The three vectors  $(\mathbf{n}, \mathbf{b}, \mathbf{t})$  defines the right-handed, orthonormal Frenet frame. We may introduce this framing at every point along the string, whenever

$$\mathbf{x}_s \times \mathbf{x}_{ss} \neq 0 \quad (3.12)$$

We proceed, momentarily, by assuming this to be the case. The Frenet equation then computes the frames along the string as follows,

$$\frac{d}{ds} \begin{pmatrix} \mathbf{n} \\ \mathbf{b} \\ \mathbf{t} \end{pmatrix} = \begin{pmatrix} 0 & \tau & -\kappa \\ -\tau & 0 & 0 \\ \kappa & 0 & 0 \end{pmatrix} \begin{pmatrix} \mathbf{n} \\ \mathbf{b} \\ \mathbf{t} \end{pmatrix} \quad (3.13)$$

Here

$$\kappa(s) = \frac{\|\mathbf{x}_s \times \mathbf{x}_{ss}\|}{\|\mathbf{x}_s\|^3} \quad (3.14)$$

is the curvature of the string on the osculating plane that is spanned by  $\mathbf{t}$  and  $\mathbf{n}$ , and

$$\tau(s) = \frac{(\mathbf{x}_s \times \mathbf{x}_{ss}) \cdot \mathbf{x}_{sss}}{\|\mathbf{x}_s \times \mathbf{x}_{ss}\|^2} \quad (3.15)$$

is the torsion that measures how the string deviates from its osculating plane. Both  $\kappa(s)$  and  $\tau(s)$  are extrinsic geometric quantities *i.e.* they depend only on the shape of the string in the ambient space  $\mathbb{R}^3$ . Conversely, if we know the curvature and torsion we can construct the string. For this we first solve for  $\mathbf{t}(s)$  from the Frenet equation. We then solve for the string by integration of (3.9). The solution is unique, modulo a global translation and rotation of the string.

Finally, we note that both the curvature (3.14) and the torsion (3.15) transform as scalars, under reparametrisations of the string. For this we introduce an infinitesimal local diffeomorphism along the string, by deforming  $s$  as follows

$$s \rightarrow s + \epsilon(s) \quad (3.16)$$

Here  $\epsilon(s)$  is an arbitrary infinitesimally small function such that

$$\epsilon(0) = \epsilon(L) = 0 = \epsilon_s(0) = \epsilon_s(L)$$

Under this reparametrization of the string, the curvature and torsion transform as follows

$$\delta\kappa(s) = -\epsilon(s) \kappa_s \quad (3.17)$$

$$\delta\tau(s) = -\epsilon(s) \tau_s$$

which is the way how scalars transform. The Lie algebra of diffeomorphisms (3.16) is the classical Virasoro (Witt) algebra.

### 3.3 Frame rotation and abelian Higgs multiplet

In order to relate the Abelian Higgs Multiplet with extrinsic string geometry, we observe that the normal and bi-normal vectors do not appear in (3.9). As a consequence a  $\text{SO}(2)$  rotation around  $\mathbf{t}(s)$ ,

$$\begin{pmatrix} \mathbf{n} \\ \mathbf{b} \end{pmatrix} \rightarrow \begin{pmatrix} \mathbf{e}_1 \\ \mathbf{e}_2 \end{pmatrix} = \begin{pmatrix} \cos \eta(s) & \sin \eta(s) \\ -\sin \eta(s) & \cos \eta(s) \end{pmatrix} \begin{pmatrix} \mathbf{n} \\ \mathbf{b} \end{pmatrix}. \quad (3.18)$$

has no effect on the string. For the Frenet equation this rotation gives

$$\frac{d}{ds} \begin{pmatrix} \mathbf{e}_1 \\ \mathbf{e}_2 \\ \mathbf{t} \end{pmatrix} = \begin{pmatrix} 0 & (\tau + \eta_s) & -\kappa \cos \eta \\ -(\tau + \eta_s) & 0 & \kappa \sin \eta \\ \kappa \cos \eta & -\kappa \sin \eta & 0 \end{pmatrix} \begin{pmatrix} \mathbf{e}_1 \\ \mathbf{e}_2 \\ \mathbf{t} \end{pmatrix}. \quad (3.19)$$

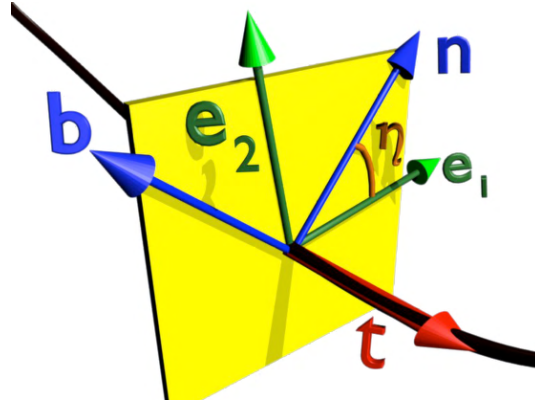


**Fig. 3.1** Rotation between the Frenet frames and a generic frame, on the normal plane of the string.

We may utilise the  $\kappa$  dependent terms in (3.19) to promote  $\kappa$  into a complex quantity, with modulus that coincides with the manifestly frame independent geometric curvature (3.14).

$$\kappa \xrightarrow{\eta} \kappa(\cos \eta + i \sin \eta) \equiv \kappa e^{i\eta} \quad (3.20)$$

This enables us to interpret the transformation of  $(\kappa, \tau)$  in (3.19) in terms of a one-dimensional version of the U(1) gauge transformation (3.1): We identify the curvature as the Higgs field and the torsion as the U(1) gauge field [58],

$$\begin{aligned} \kappa &\rightarrow \kappa e^{-i\eta} \equiv \phi \\ \tau &\rightarrow \tau + \eta_s \equiv A_i \end{aligned} \quad (3.21)$$

Note that when we choose

$$\eta(s) \rightarrow \eta_B(s) = - \int_0^s \tau(\tilde{s}) d\tilde{s} \quad (3.22)$$

we arrive at the *unitary* gauge in terms of the abelian Higgs multiplet. This defines Bishop's parallel transport framing [59]. The Bishop's frame vectors  $\mathbf{e}_{1,2}^B$  do not rotate around the tangent vector,

$$\frac{d}{ds} (\mathbf{e}_1^B + i\mathbf{e}_2^B) = -\kappa e^{-i\eta_B} \mathbf{t}$$

Thus, unlike the Frenet framing that can not be introduced when the curvature  $\kappa(s)$  vanishes, the Bishop framing can be introduced and defined in an unambiguous and continuous manner even in that case. However, it turns out that in the case of proteins which is the subject we are interested in, the Bishop frames do not work very well [60].

### 3.4 The unique string Hamiltonian

The curvature and torsion are the *only* available geometric quantities for constructing energy functions of strings, while (3.2), (3.3) is the *unique* energy of the Abelian Higgs multiplet in the Kadanoff-Wilson sense of universality.

Consider a string, in the limit where the curvature and torsion are slowly varying functions along it. The shape of the string can not depend on the framing, thus its energy can only involve combinations of the curvature and torsion in a manifestly frame independent fashion.

On the other hand, (3.2), (3.3) is the unique  $SO(2) \sim U(1)$  invariant energy function that involves a complex Higgs field and a gauge field. It emerges from general arguments and symmetry principles alone, in the limit where the length scale that is associated to spatial variations of the field variables becomes very large in comparison to other characteristic length scales of the system.

Thus the *only* Hamiltonian that can describe a string and its dynamics in the infrared limit is [58].

$$H = \int_0^L ds \left\{ |(\partial_s + ie\tau)\kappa|^2 + \lambda(|\kappa|^2 - m^2)^2 \right\} + a \int_0^L ds \tau \quad (3.23)$$

We have here included the one dimensional version of the Chern-Simons term (3.3). It introduces net helicity along the string, breaking the  $\mathbb{Z}_2$  symmetry between strings that are twisted in the right-handed and left-handed sense.

In (3.23) both  $\kappa$  and  $\tau$  are expressed in a generic, arbitrary framing of the string. The corresponding gauge invariant variables (3.5) are the curvature (3.14) and torsion (3.15) that characterise the extrinsic string geometry. In terms of these gauge invariant variables, which we from now on denote by  $(\kappa, \tau)$  the Hamiltonian (3.23) is

$$H = \int_0^L ds \left\{ (\partial_s \kappa)^2 + e^2 \kappa^2 \tau^2 + \lambda(\kappa^2 - m^2)^2 \right\} + a \int_0^L ds \tau \quad (3.24)$$

where we have simply followed the steps that gave us (3.6). Thus (3.24) is the unique energy of a string, in terms of geometrically defined curvature and torsion, and in the limit where the spatial variations of curvature and torsion along the string are small.

### 3.5 Integrable hierarchy

A relation exist between (3.24), the integrable hierarchy of the nonlinear Schrödinger (NLS) equation, and the Heisenberg spin chain of ferromagnetism. For this we introduce the following Hasimoto variable

$$\psi(s) = \kappa(s) e^{ie \int_0^s ds' \tau(s')} \quad (3.25)$$

that combines the curvature and torsion into a single gauge invariant complex variable. In terms of (3.25), we obtain the Hamiltonian of the integrable nonlinear Schrödinger equation [61, 62, 65] as follows,

### 36 Strings in three space dimensions

$$\kappa_s^2 + e^2 \kappa^2 \tau^2 + \lambda \kappa^4 = \bar{\psi}_s \psi_s + \lambda (\bar{\psi} \psi)^2 = \mathcal{H}_3 \quad (3.26)$$

The lower level conserved densities in the integrable NLS hierarchy are the helicity  $\mathcal{H}_{-2}$ , length (i.e. Nambu-Goto)  $\mathcal{H}_{-1}$ , number operator  $\mathcal{H}_1$  and momentum  $\mathcal{H}_2$

$$\begin{aligned} \mathcal{H}_{-2} &= \tau \\ \mathcal{H}_{-1} &= L \\ \mathcal{H}_1 &= \kappa^2 \\ \mathcal{H}_2 &= \kappa^2 \tau \end{aligned} \quad (3.27)$$

The energy (3.24) is a combination of  $\mathcal{H}_{-2}$ ,  $\mathcal{H}_1$  and  $\mathcal{H}_3$ . From the perspective of the NLS hierarchy, the momentum  $\mathcal{H}_2$  should also be included for completeness. If higher order corrections are desired the natural candidate is the mKdV density

$$\mathcal{H}_4 = \kappa \kappa_{ss} \tau + 4\kappa^2 \tau^3 - 4e^2 \kappa_s^2 \tau + 3\lambda \kappa^4 \tau$$

with appears as the next level conserved density in the NLS hierarchy.

We note that the Heisenberg spin chain is obtained from  $\mathcal{H}_1$  using the Frenet equation.

$$\int_0^L ds \mathcal{H}_1 = \int_0^L ds \kappa^2 = \int_0^L ds |\mathbf{t}_s|^2$$

The combination of  $\mathcal{H}_{-1}$  and  $\mathcal{H}_1$  leads to Polyakov's rigid string action [63]. This combination also coincides with the Kratky-Porod model of polymers [64].

In reference [63], the concept of perturbative level Wilsonian universality is employed to argue, that no additional terms besides  $\mathcal{H}_{-1}$  and  $\mathcal{H}_1$  should appear in the infrared limit. But in the presence of non-perturbative structures any perturbative argument becomes incomplete: The NLS Hamiltonian (3.26) supports solitons that do not co-exist with perturbative arguments.

## 3.6 Strings from solitons

Solitons are the paradigm structural self-organisers in Nature. Solitons become materialised in diverse scenarios [61, 62, 65, 66]; we have already seen that solitons conduct electricity in organic polymers. But solitons can also transmit data in transoceanic cables, and solitons can transport chemical energy along proteins. Solitons explain the Meißner effect in superconductivity and solitons model dislocations in liquid crystals. Solitons are used to describe hadronic particles, cosmic strings and magnetic monopoles in high energy physics.

We argue that solitons also describe life. We argue that each of us has some  $10^{20}$  solitons in our body. These solitons are the building blocks of folded proteins, they are the essential ingredients in all the metabolic processes that make us alive.

The NLS equation that we obtain from (3.26), is the paradigm equation that supports solitons [61, 62, 66, 65]. Depending on the sign of  $\lambda$ , the soliton is either dark ( $\lambda > 0$ ) or bright ( $\lambda < 0$ ). The torsion independent contribution to (3.24)

$$H = \int_{-\infty}^{\infty} ds \left\{ \kappa_s^2 + \lambda (\kappa^2 - m^2)^2 \right\} \quad (3.28)$$

reproduces our previous instanton equation (1.22) with  $Q = \sqrt{2}$ ; the Hamiltonian (3.28) supports the double well soliton *a.k.a.* the paradigm *topological* soliton: When  $m^2$  is positive and when  $\kappa$  can take both positive and negative values, the equation of motion

$$\kappa_{ss} = 2\lambda\kappa(\kappa^2 - m^2)$$

is solved by - see (1.24)

$$\kappa(s) = m \tanh \left[ m\sqrt{\lambda}(s - s_0) \right] \quad (3.29)$$

We have concluded that the energy function

$$\mathcal{E} = \int ds \left\{ \kappa_s^2 + \lambda(\kappa^2 - m^2)^2 + \frac{d}{2}\kappa^2\tau^2 - b\kappa^2\tau - a\tau + \frac{c}{2}\tau^2 \right\} \quad (3.30)$$

is the most general one, a linear combination of *all* the densities (3.26), (3.27). In (3.30) we have also included the Proca mass; this is the last term. Even though the Proca mass does not appear in the integrable NLS hierarchy, it does have a claim to be gauge invariant [67, 68]. Eventually, we shall present a topological argument why the Proca mass should be included.

The energy (3.30) is quadratic in the torsion. Thus we can eliminate  $\tau$  using its equation of motion,

$$\frac{\delta \mathcal{E}}{\delta \tau} = d\kappa^2\tau - b\kappa^2 - a + c\tau = 0 \quad (3.31)$$

This gives

$$\tau[\kappa] = \frac{a + b\kappa^2}{c + d\kappa^2} \equiv \frac{a}{c} \frac{1 + (b/a)\kappa^2}{1 + (d/c)\kappa^2} \quad (3.32)$$

and we obtain the following *effective* energy for the curvature,

$$\mathcal{E}_\kappa = \int ds \left\{ \frac{1}{2}\kappa_s^2 + V[\kappa] \right\} \quad (3.33)$$

with the equation of motion

$$\frac{\delta \mathcal{E}_\kappa}{\delta \kappa} = -\kappa_{ss} + V_\kappa = 0 \quad (3.34)$$

where

$$V[\kappa] = - \left( \frac{bc - ad}{d} \right) \frac{1}{c + d\kappa^2} - \left( \frac{b^2 + 8\lambda m^2}{2b} \right) \kappa^2 + \lambda \kappa^4 \quad (3.35)$$

This is a deformation of the potential in (3.28), the two share the same large- $\kappa$  asymptotics. When we select the parameters properly, we can expect that (3.31), (3.34),

(3.35) continue to support topological solitons. But we do not know their explicit profile, in terms of elementary functions. In the sequel we shall construct these solitons numerically.

Once we have constructed the soliton of (3.34), we evaluate  $\tau(s)$  from (3.32). We substitute these profiles in the Frenet equation (3.13) and solve for  $\mathbf{t}(s)$ . We then integrate (3.9) to obtain the string  $\mathbf{x}(s)$  that corresponds to the soliton.

### 3.7 Anomaly in the Frenet frames

When the curvature of a string vanishes, we have an anomaly in the Frenet framing. It turns out that the origin of the anomaly is the *raison d'être* for a topological soliton to reside on a string.

Until now, we have assumed (3.12) so that the curvature (3.14) does not vanish. But we have also observed that in the case of the Abelian Higgs model (3.6) it is natural for the density  $\rho$  to vanish, on the world-sheet of a vortex core. Thus, in the context of AHM the vanishing of  $\rho$  relates to important, physically significant effects.

Furthermore, the explicit soliton profile (3.29) displays both positive and negative values, and in particular (3.29) vanishes when  $s = s_0$ . Consequently we should consider the possibility that  $\kappa$  may vanish, even become negative, along a string.

We start by extending the curvature (3.14) so that it has both positive and negative values. According to (3.20) the negative values of  $\kappa$  are related to the positive ones by a  $\eta = \pm\pi$  frame rotation,

$$\kappa \xrightarrow{\eta = \pm\pi} e^{\pm i\pi} \kappa = -\kappa \quad (3.36)$$

Hence we compensate for an extension of (3.14) to negative values, by introducing the discrete  $\mathbb{Z}_2$  symmetry [60]

$$\begin{aligned} \kappa &\leftrightarrow -\kappa \\ \eta &\leftrightarrow \eta \pm \pi \end{aligned} \Leftrightarrow \kappa e^{i\eta} \leftrightarrow \kappa e^{i\eta} \quad (3.37)$$

An (isolated) point where  $\kappa(s)$  vanishes is called an inflection point. Figure 3.2 shows an example of an inflection point. As shown in this Figure, in the limit of a plane curve we obtain a discontinuity in the Frenet frames, when the string goes through the inflection point: The zweibein  $(\mathbf{n}, \mathbf{b})$  becomes reflected according to

$$(\mathbf{n} + i\mathbf{b}) \longrightarrow -(\mathbf{n} + i\mathbf{b}) = e^{\pm i\pi}(\mathbf{n} + i\mathbf{b}) \quad (3.38)$$

when we have a simple inflection point along the string. At the inflection point itself, the Frenet frames can not be defined. Thus we can not deduce whether we have a jump by  $\eta = +\pi$  or by  $\eta = -\pi$  at the inflection point. We can not conclude whether the Frenet frame vectors  $(\mathbf{n}, \mathbf{b})$  become rotated clockwise or counterclockwise by an angle  $\pi$  along the tangent vector. There is a  $\mathbb{Z}_2$  anomaly in the definition of Frenet framing, due to inflection points.

To analyse the anomaly, consider a string  $\mathbf{x}(s)$  that has a simple inflection point when  $s = s_0$ . Thus  $\kappa(s_0) = 0$  but  $\kappa_s(s_0) \neq 0$ , as shown in Figure 3.2. To simplify the notation we re-define the parameter  $s$  so that the inflection point occurs at  $s_0 = 0$ .



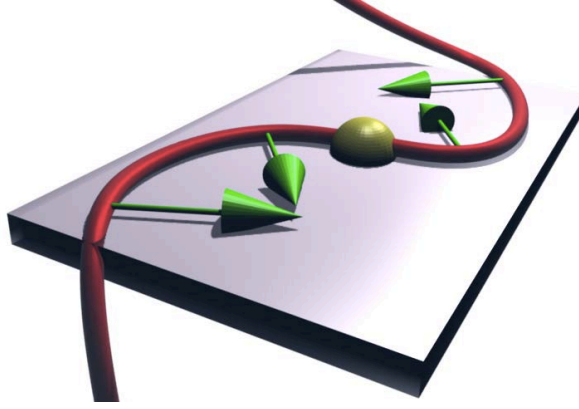


**Fig. 3.2** A string with inflection point (ball). At each point the Frenet frame normal vector points towards the center of the osculating circle. At the inflection point we have a discontinuity in the direction of the normal vectors: The radius of the osculating circle diverges and the normal vector are reflected in the osculating plane, from one side to the other side of the string.

We can always remove the inflection point by a generic deformation of the string: A deformation which is restricted to the plane as in Figure 3.2 only slides the inflection point along the string without removing it. In order to remove the inflection point we need to deform the string off its instantaneous tangent plane: The co-dimension of the inflection point in  $\mathbb{R}^3$  is two, the inflection point is not generic along a string.

Consider two different generic deformations,

$$\mathbf{x}(s) \rightarrow \mathbf{x}(s) + \delta\mathbf{x}_{1,2}(s) = \mathbf{x}_{1,2}(s) \quad (3.39)$$

In the case shown in Figure 3.2, these two deformations amount to moving the string either slightly up from the plane, or slightly down from the plane, around the inflection point. We assume that the deformations are very small, and compactly supported so that

$$\delta\mathbf{x}_{1,2}(\pm\varepsilon_{\pm}) = 0$$

Here  $\varepsilon_{\pm} > 0$  are small and determine the parameter values where the deformations  $\mathbf{x}_{1,2}(s)$  bifurcate.

Imagine now a closed string denoted  $\gamma$ , that starts from  $\mathbf{x}(-\varepsilon_-)$ , follows along  $\mathbf{x}_1$  to  $\mathbf{x}(+\varepsilon_+)$  and then returns along  $\mathbf{x}_2$  back to  $\mathbf{x}(-\varepsilon_-)$ . Introduce the Frenet frame normal vectors of  $\gamma$ ; by shifting  $\gamma$  slightly into the direction of its Frenet frame normals, we obtain a second closed string which we call  $\tilde{\gamma}$ . Let  $\mathbf{t}$  and  $\tilde{\mathbf{t}}$  be the corresponding tangent vectors. The Gauß linking number of  $\gamma$  and  $\tilde{\gamma}$  is

$$\text{Lk} = \frac{1}{4\pi} \oint_{\gamma} \oint_{\tilde{\gamma}} ds d\tilde{s} \frac{\mathbf{x} - \tilde{\mathbf{x}}}{|\mathbf{x} - \tilde{\mathbf{x}}|^3} \cdot (\mathbf{t} \times \tilde{\mathbf{t}})$$

Proceeding along  $\mathbf{x}_{1,2}(s)$  the respective Frenet frames are continuously rotated by  $\eta_{1,2} \approx \pm\pi$ ; in the limit where  $\delta\mathbf{x}_{1,2} \rightarrow 0$  we would obtain the discontinuous jump

(3.38). By continuity of Frenet framing in the complement of inflection points, the linking number has values  $Lk = \pm 1$  when the  $\eta_{1,2}$  change in the same direction; we remind that  $\gamma$  proceeds "backwards" along  $\mathbf{x}_2$ . But if the framing along  $\mathbf{x}_1(s)$  and  $\mathbf{x}_2(s)$  rotate in the opposite directions, we have  $Lk = 0$ .

Accordingly, the relative sign of  $\eta_{1,2}$  depends on the way how the inflection point is circumvented: We have a *frame anomaly* in the Frenet framing as  $\delta\mathbf{x}_{1,2} \rightarrow 0$ , the value of  $Lk$  depends on the way how we define  $\delta\mathbf{x}_{1,2}(s)$ .

*Homework: Analyse the framing of a string in the presence of an inflection point, using the Bishop's frames (3.22).*

### 3.8 Perestroika

An inflection point together with the corresponding Frenet frame anomaly can be given an interpretation in terms of a string specific bifurcation, which is called *inflection point perestroika* [69–73]. It explains why a *uniquely* defined Frenet framing across the inflection point, or any other framing that rotates around the tangent vector, is not possible:

Consider a segment of a string, along which the torsion  $\tau(s)$  vanishes. Accordingly the string segment is constrained on a plane, as in figure 3.2. When a string is constrained on a plane, a simple isolated inflection point is generic. This follows since for a string on plane the inflection point has co-dimension one. Moreover, in the case of a string on plane a single simple inflection point is a topological invariant. It can only be moved around the plane but not made to disappear; unless it escapes the plane which we now assume is not the case. If we have two simple inflection points along a string on plane, we can bring them together to deform the string so that no inflection point remains. Thus the inflection point is a *mod*(2) topological invariant of a string on plane.

Consider now a generic string in  $\mathbb{R}^3$ ; a generic string is not constrained on a plane. The co-dimension of a single simple inflection point is two, thus a generic string does not have any inflection points. But along a string which moves freely in  $\mathbb{R}^3$ , an isolated simple inflection point appears generically, at some point, at some moment, during the motion. When this inflection point perestroika takes place along the moving string, it leaves a trail behind: The inflection point perestroika changes the number of *flattening points*, which are points along the string where the torsion  $\tau(s)$  vanishes [72, 73].

At a simple flattening point the curvature  $\kappa(s)$  is generically non-vanishing, but the torsion  $\tau(s)$  changes its sign. Accordingly the inflection point perestroika can only change the number of simple flattening points by two. Apparently, it always does [72, 73].

Unlike the inflection point, a flattening point where  $\tau(s) = 0$  is generic along a static space string. Furthermore, unlike a simple inflection point, a single simple flattening point that occurs in a one parameter family of strings in  $\mathbb{R}^3$  is a topological invariant. It can not disappear on its own, under local deformations that leave the ends of the string intact. A pair of flattening points can be combined together, into a single bi-flattening point, which can then dissolve. When this happens, a second string-specific bifurcation which is called *bi-flattening perestroika* takes place.

Apparently, inflection point perestroika and bi-flattening perestroika are the only two bifurcations where the number of flattening points can change [73]. The number of simple flattening points is a *local* invariant of the string. Besides the flattening number, and the self-linking number in case of a framed string, a generic smooth string does not possess any other essential local invariants [72]. The two are also mutually independent, even though they often appear together.

For example, one can deduce that the self-linking number of a string increases by one if the torsion is positive when the string approaches its simple inflection point, and if two simple flattening points disappear after the passage of the inflection point. Moreover, if the torsion is negative, the self-linking number decreases by one when two flattening points disappear after the passage [72]. But when two simple flattening points dissolve in a bi-flattening perestroika, the self-linking number in general does not change.

A bifurcation is the paradigm cause for structural transitions, including phase transitions, in any dynamical system. Inflection point and bi-flattening perestroika's are the only bifurcations that are string specific. Accordingly these two perestroika's must have a profound influence on determining the physical behaviour and phase structure of string-like configurations. In particular, these perestroika's must be responsible for any string-specific structural re-organisation that can take place when the value of the compactness index  $\nu$  (1.7) changes. Since perestroika's relate to the creation and disappearance of topological solitons such as (3.29) along a string, it is clear that perestroika's and topological solitons, with the ensuing physical effects, are commonplace whenever we have a string with an energy function of the form (3.30).

### 3.8.1 Example:

A good example of the interplay between inflection points and flattening points is given by (3.29) or more generally by a soliton solution of (3.34), and (3.32). For a regular string, the denominator of (3.32) should not vanish. Thus, in the case of an inflection point the ration  $(d/c)$  should be positive. When  $(b/a)$  is negative, we have a symmetric pair of inflection points around the inflection point. Thus starting from a one-parameter family of strings  $\kappa(s, v)$  with  $v$  the parameter, if initially  $\kappa(s, v)$  is sufficient large and e.g. positive, and we are not close to an inflection point, there are no flattening points either. When  $v$  is varied so that the inflection point is approached, a pair of flattening points emerges and remains whenever the curvature has the profile (3.29). In particular, we conclude that it is important to retain the Proca mass term, even a very small one, as a regulator.

## 4

# Discrete Frenet Frames

---

Proteins are not like continuous differentiable strings. Proteins are like piecewise linear polygonal strings. Thus, to understand the physical properties of proteins we need to develop the formalism of discrete strings. Accordingly, we proceed to generalise the Frenet frame formalism to the case of polygonal strings that are piecewise linear [60].

Let  $\mathbf{r}_i$  with  $i = 1, \dots, N$  be the vertices of a piecewise linear discrete string. At each vertex we introduce the unit tangent vector

$$\mathbf{t}_i = \frac{\mathbf{r}_{i+1} - \mathbf{r}_i}{|\mathbf{r}_{i+1} - \mathbf{r}_i|} \quad (4.1)$$

the unit binormal vector

$$\mathbf{b}_i = \frac{\mathbf{t}_{i-1} - \mathbf{t}_i}{|\mathbf{t}_{i-1} - \mathbf{t}_i|} \quad (4.2)$$

and the unit normal vector

$$\mathbf{n}_i = \mathbf{b}_i \times \mathbf{t}_i \quad (4.3)$$

The orthonormal triplet  $(\mathbf{n}_i, \mathbf{b}_i, \mathbf{t}_i)$  defines a discrete version of the Frenet frames (3.9)-(3.11) at each position  $\mathbf{r}_i$  along the string, as shown in Figure (4.1)

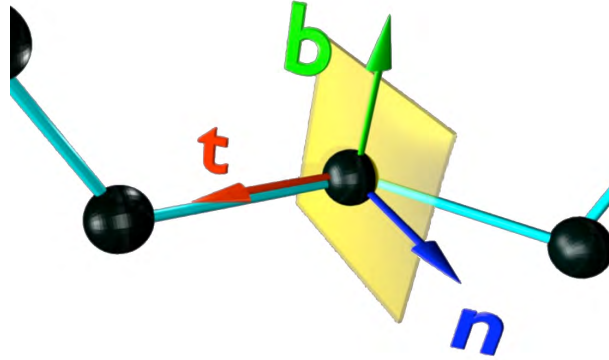


**Fig. 4.1** Discrete Frenet frames along a piecewise linear discrete string.

In lieu of the curvature and torsion, we have the bond angles and torsion angles, defined as in Figure 4.2.

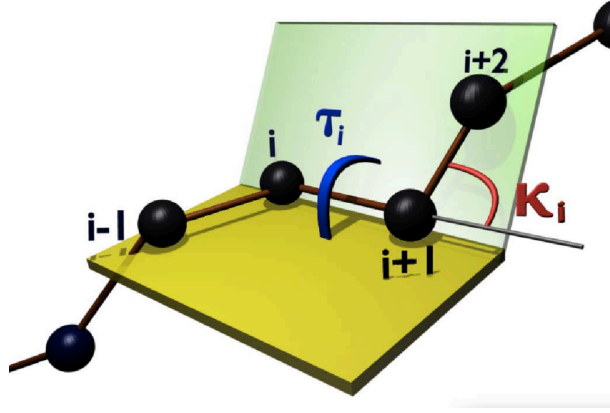


**Fig. 4.2** Definition of bond ( $\kappa_i$ ) and torsion ( $\tau_i$ ) angles, along the piecewise linear discrete string.

When we know the Frenet frames at each vertex, we can compute the values of these angles: The bond angles are

$$\kappa_i \equiv \kappa_{i+1,i} = \arccos(\mathbf{t}_{i+1} \cdot \mathbf{t}_i) \quad (4.4)$$

and the torsion angles are

$$\tau_i \equiv \tau_{i+1,i} = \text{sign}\{\mathbf{b}_{i-1} \times \mathbf{b}_i \cdot \mathbf{t}_i\} \cdot \arccos(\mathbf{b}_{i+1} \cdot \mathbf{b}_i) \quad (4.5)$$

Conversely, when the values of the bond and torsion angles are all known, we can use the discrete Frenet equation

$$\begin{pmatrix} \mathbf{n}_{i+1} \\ \mathbf{b}_{i+1} \\ \mathbf{t}_{i+1} \end{pmatrix} = \begin{pmatrix} \cos \kappa \cos \tau & \cos \kappa \sin \tau & -\sin \kappa \\ -\sin \tau & \cos \tau & 0 \\ \sin \kappa \cos \tau & \sin \kappa \sin \tau & \cos \kappa \end{pmatrix}_{i+1,i} \begin{pmatrix} \mathbf{n}_i \\ \mathbf{b}_i \\ \mathbf{t}_i \end{pmatrix} \quad (4.6)$$

to compute the frame at position  $i+1$  from the frame at position  $i$ . Once all the frames have been constructed, the entire string is given by

$$\mathbf{r}_k = \sum_{i=0}^{k-1} |\mathbf{r}_{i+1} - \mathbf{r}_i| \cdot \mathbf{t}_i \quad (4.7)$$

Without any loss of generality we may choose  $\mathbf{r}_0 = 0$ , make  $\mathbf{t}_0$  to point into the direction of the positive  $z$ -axis, and let  $\mathbf{t}_1$  lie on the  $y$ - $z$  plane.

The vectors  $\mathbf{n}_i$  and  $\mathbf{b}_i$  do not appear in (4.7). Thus, as in the case of continuum strings, a discrete string remains intact under frame rotations of the  $(\mathbf{n}_i, \mathbf{b}_i)$  zweibein around  $\mathbf{t}_i$ . This local  $\text{SO}(2)$  rotation acts on the frames as follows

$$\begin{pmatrix} \mathbf{n} \\ \mathbf{b} \\ \mathbf{t} \end{pmatrix}_i \rightarrow e^{\Delta_i T^3} \begin{pmatrix} \mathbf{n} \\ \mathbf{b} \\ \mathbf{t} \end{pmatrix}_i = \begin{pmatrix} \cos \Delta_i & \sin \Delta_i & 0 \\ -\sin \Delta_i & \cos \Delta_i & 0 \\ 0 & 0 & 1 \end{pmatrix} \begin{pmatrix} \mathbf{n} \\ \mathbf{b} \\ \mathbf{t} \end{pmatrix}_i \quad (4.8)$$

#### 44 Discrete Frenet Frames

Here  $\Delta_i$  is the rotation angle at vertex  $i$  and  $T^3$  is one of the  $\text{SO}(3)$  generators

$$T^1 = \begin{pmatrix} 0 & 0 & 0 \\ 0 & 0 & -1 \\ 0 & 1 & 0 \end{pmatrix} \quad T^2 = \begin{pmatrix} 0 & 0 & 1 \\ 0 & 0 & 0 \\ -1 & 0 & 0 \end{pmatrix} \quad T^3 = \begin{pmatrix} 0 & -1 & 0 \\ 1 & 0 & 0 \\ 0 & 0 & 0 \end{pmatrix}$$

that satisfy the Lie algebra

$$[T^a, T^b] = \epsilon^{abc} T^c$$

Using these matrices we can write the effect of frame rotation on the bond and torsion angles as follows

$$\kappa_i T^2 \rightarrow e^{\Delta_i T^3} (\kappa_i T^2) e^{-\Delta_i T^3} \quad (4.9)$$

$$\tau_i \rightarrow \tau_i + \Delta_{i-1} - \Delta_i \quad (4.10)$$

From the point of view of lattice gauge theories, the transformation of bond angles is like an adjoint  $\text{SO}(2) \in \text{SO}(3)$  gauge rotation of a Higgs triplet around the Cartan generator  $T^3$ , when the Higgs triplet is in the direction of  $T^2$ . The transformation of torsion angle coincides with that of the  $\text{SO}(2)$  lattice gauge field. Since the  $\mathbf{t}_i$  remain intact under (4.8), the gauge transformation of  $(\kappa_i, \tau_i)$  has no effect on the geometry of the discrete string.

*A priori*, the fundamental range of the bond angle is  $\kappa_i \in [0, \pi]$  while for the torsion angle the range is  $\tau_i \in [-\pi, \pi]$ . Thus we identify  $(\kappa_i, \tau_i)$  as the canonical latitude and longitude angles of a two-sphere  $\mathbb{S}^2$ . In parallel with the continuum case we find it useful to extend the range of  $\kappa_i$  into negative values  $\kappa_i \in [-\pi, \pi] \bmod(2\pi)$ . As in (3.36) we compensate for this two-fold covering of  $\mathbb{S}^2$  by a  $\mathbb{Z}_2$  symmetry which now takes the following form:

$$\begin{aligned} \kappa_k &\rightarrow -\kappa_k & \text{for all } k \geq i \\ \tau_i &\rightarrow \tau_i - \pi \end{aligned} \quad (4.11)$$

This is a special case of (4.9), (4.10), with

$$\begin{aligned} \Delta_k &= \pi & \text{for } k \geq i+1 \\ \Delta_k &= 0 & \text{for } k < i+1 \end{aligned}$$

### 4.1 The $\text{C}\alpha$ trace reconstruction

We have already concluded that the Ramachandran angles are not sufficient for reconstructing the protein backbones: As shown in Figure (1.11) the reconstructed backbones are not in the same universality class with folded proteins. The value of the compactness index  $\nu$  is different. For a correct reconstruction, we need to utilise all the bond and torsion angles that we have defined in Figure 1.7. Only for the bond lengths can the average values be used.

We now consider the protein backbone reconstruction, in terms of virtual  $\text{C}\alpha$  backbone. We identify the vertices in Figure 4.2 with the  $\text{C}\alpha$  atoms, so that  $(\kappa_i, \tau_i)$  are the

virtual  $C\alpha$  backbone bond and torsion angles. For the virtual  $C\alpha$ - $C\alpha$  bond lengths we use the average PDB value

$$|\mathbf{r}_{i+1} - \mathbf{r}_i| \sim 3.8 \text{ \AA} \quad (4.12)$$

It turns out that, *unlike* in the case of the Ramachandran angles, the ensuing reconstructed  $C\alpha$  backbones reproduce the original crystallographic structures, with a very high precision; the difference is mostly within the range of experimental errors, as measured by the B-factor (1.4). In Figure 4.3 we compare the radius of gyration values

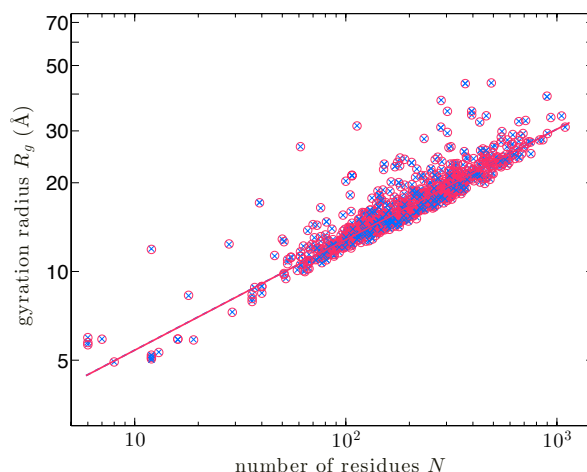


**Fig. 4.3** Comparison of the  $C\alpha$ - $C\alpha$  radius of gyration data between the original PDB structures and those reconstructed in terms of variable virtual bond and torsion angles in combination with optimal  $C\alpha$ - $C\alpha$  virtual bond lengths. The (blue) crosses are the original PDB structures, and the (red) circles are the reconstructed ones. The line shows the fits of the radius of gyration. We have no visual difference, between the two cases.

in our ultra-high resolution protein structures, for the original PDB structures and those that have been reconstructed using the virtual  $C\alpha$  backbone bond and torsion angles when we use the constant virtual bond length value (4.12). Unlike in the Figure (1.11), now we observe no visual difference. For the reconstructed data, we obtain the relation [26]

$$R_g \approx 2.281 N^{0.375} \text{ \AA}$$

This is remarkably close to (1.10), the difference is immaterial. Thus we conclude that in the case of crystallographic protein structures the virtual  $C\alpha$  trace bond and torsion angles  $(\kappa_i, \tau_i)$  form a complete set of geometrical local order parameters.

## 4.2 Universal discretised energy

The goal is to describe the structure and dynamics of proteins *beyond* the limitations of an expansion in a small coupling like (1.13). For this we propose to start with an energy function where the virtual  $C\alpha$  backbone bond and torsion angles appear as

local order parameters; these variables form a complete set of local order parameters, for reconstruction.

Let  $F$  be the thermodynamical Helmholtz free energy of a protein. Its minimum energy configuration describes a folded protein, under thermodynamical equilibrium conditions. The free energy is the sum of the internal energy  $U$  and the entropy  $S$ , at temperature  $T$

$$F = U - TS \quad (4.13)$$

It is a function of all the inter-atomic distances

$$F = F(r_{\alpha\beta}) ; \quad r_{\alpha\beta} = |\mathbf{r}_\alpha - \mathbf{r}_\beta| \quad (4.14)$$

where the indices  $\alpha, \beta, \dots$  extend over all the atoms in the protein system, including those of the solvent environment.

We assume that the characteristic length scales of spatial deformations along the protein backbone around its thermal equilibrium configuration are large in comparison to the covalent bond lengths; there are no abrupt wrenches and buckles, only gradual bends and twists. We also assume that the  $C\alpha$  virtual bond length oscillations have a characteristic time scale which is short in comparison to the time scale we consider; we adopt (4.12) as a time averaged value for all the virtual bond lengths. The completeness of the  $C\alpha$  bond and torsion angles then proposes that in the vicinity of the free energy minimum we utilise these angles as the local order parameters. Accordingly, we consider the response of the interatomic distances to variations in these angles,

$$r_{\alpha\beta} = r_{\alpha\beta}(\kappa_i, \tau_i)$$

Suppose that at a local extremum of the free energy, the  $C\alpha$  bond and torsion angles have the values

$$(\kappa_i, \tau_i) = (\kappa_{i0}, \tau_{i0})$$

Consider a conformation where the  $(\kappa_i, \tau_i)$  deviate from these extremum values. The deviations are

$$\begin{aligned} \Delta\kappa_i &= \kappa_i - \kappa_{i0} \\ \Delta\tau_i &= \tau_i - \tau_{i0} \end{aligned} \quad (4.15)$$

Taylor expand the infrared limit Helmholtz free energy (4.13) around the extremum,

$$\begin{aligned} F[r_{\alpha\beta} = r_{\alpha\beta}(\kappa_i, \tau_i)] &\equiv F(\kappa_i, \tau_i) = F(\kappa_{i0}, \tau_{i0}) + \sum_k \left\{ \frac{\partial F}{\partial \kappa_k} \Big|_0 \Delta\kappa_k + \frac{\partial F}{\partial \tau_k} \Big|_0 \Delta\tau_k \right\} \\ &+ \sum_{k,l} \left\{ \frac{1}{2} \frac{\partial^2 F}{\partial \kappa_k \partial \kappa_l} \Big|_0 \Delta\kappa_k \Delta\kappa_l + \frac{\partial^2 F}{\partial \kappa_k \partial \tau_l} \Big|_0 \Delta\kappa_k \Delta\tau_l + \frac{1}{2} \frac{\partial^2 F}{\partial \tau_k \partial \tau_l} \Big|_0 \Delta\tau_k \Delta\tau_l \right\} + \mathcal{O}(\Delta^3) \end{aligned}$$

The first term in the expansion evaluates the free energy at the extremum. Since  $(\kappa_{i0}, \tau_{i0})$  correspond to the extremum, the second term vanishes and we are left with the following expansion of the averaged free energy,

$$F(\kappa_i, \tau_i) = F(\kappa_{i0}, \tau_{i0})$$



$$+ \sum_{k,l} \left\{ \frac{1}{2} \frac{\partial^2 F}{\partial \kappa_k \partial \kappa_l} \Delta \kappa_k \Delta \kappa_l + \frac{\partial^2 F}{\partial \kappa_k \partial \tau_l} \Delta \kappa_k \Delta \tau_l + \frac{1}{2} \frac{\partial^2 F}{\partial \tau_k \partial \tau_l} \Delta \tau_k \Delta \tau_l \right\} + \dots \quad (4.16)$$

In the limit where the characteristic scale of the extent of spatial deformations around a minimum energy configuration is large in comparison to a covalent bond length, and the amplitude of these deformations remains small, we may *re-arrange* the expansion (4.16) in terms of the differences in the angles as follows: First comes local terms. Then comes terms that connect the nearest-neighbors. Then comes terms that connect the next-to-nearest neighbours. And so forth ... This re-ordering of the expansion ensures that we recover the derivative expansion (3.4) in leading order, when we take the continuum limit where the virtual bond length vanishes. Moreover, since the free energy *must* remain invariant under the local frame rotations (4.9), (4.10) we conclude [58, 74–81] that to the leading order the expansion of the free energy *must* coincide with a discretisation of the AHM energy (3.2), (3.3):

$$F = - \sum_{i=1}^{N-1} 2 \kappa_{i+1} \kappa_i + \sum_{i=1}^N \left\{ 2 \kappa_i^2 + \lambda (\kappa_i^2 - m^2)^2 + \frac{q}{2} \kappa_i^2 \tau_i^2 - p \tau_i + \frac{r}{2} \tau_i^2 \right\} + \dots \quad (4.17)$$

The corrections include next-to-nearest neighbours couplings and so forth, which are higher order terms from the point of view of our systematic expansion: The approximation (4.17) is valid, as long as there are no abrupt wrenches and buckles but only gradual bends and twists along the backbone. In particular, long range interactions are accounted for as long as they don't introduce any localised buckling of the backbone.

In (4.17)  $\lambda$ ,  $q$ ,  $p$ ,  $r$ , and  $m$  depend on the atomic level physical properties and the chemical microstructure of the protein and its environment. In principle, these parameters can be computed from this knowledge.

We note the following: The free energy (4.17) is a deformation of the standard energy function of the discrete nonlinear Schrödinger equation (DNLS) [61, 62]. The first sum together with the three first terms in the second sum is the energy of the standard DNLS equation, in terms of the discretized Hasimoto variable (3.25). The fourth term ( $p$ ) is the conserved helicity, it breaks the  $\mathbb{Z}_2$  parity symmetry and is responsible for the right-handed helicity of the C $\alpha$  backbone. The last ( $r$ ) term is the Proca mass that we again add, as a "regulator". Observe in particular the explicit presence of the non-linear, quartic contribution to the (virtual) bond angle energy. This is the familiar double-well potential, shown in Figure 1.12. Its  $\mathbb{Z}_2$  symmetry becomes eventually broken. The breaking of this symmetry is essential for the emergence of structure, in the case of proteins. It is the source of *Bol'she* that makes us alive. We note that this kind of explicit non-linearity is absent in (1.11).

We summarise: The expression (4.17) of the free energy describes the small amplitude fluctuations around the local extremum  $(\kappa_{i0}, \tau_{i0})$  in the space of bond and torsion angles. It can be identified as the long wavelength (infrared) limit of the full free energy, in the sense of Kadanoff and Wilson. To the present order of the expansion in powers of  $(\kappa_i, \tau_i)$ , the functional form (4.17) is the *most general* long wavelength free energy that is compatible with the principle gauge invariance. This *fundamental* symmetry principle ensures that no physical quantity depends on our choice of coordinates (framing) along the backbone.

*Research project: Develop a method to compute the parameters in (4.17) from an all-atom energy function.*

### 4.3 Discretized solitons

The energy (4.17) is a deformation of the integrable energy of the discrete nonlinear Schrödinger (DNLS) equation [61, 62, 65]: The first term together with the  $\lambda$  and  $d$  dependent terms constitute the (naively) discretized Hamiltonian of the NLS model in the Hasimoto variable. The conventional DNLS equation is known to support solitons. Thus we can try and find soliton solutions of (4.17).

As in (3.32) we first eliminate the torsion angle,

$$\tau_i[\kappa] = \frac{a + b\kappa_i^2}{c + d\kappa_i^2} = a \frac{1 + b\kappa_i^2}{c + d\kappa_i^2} \equiv a\hat{\tau}_i[\kappa] \quad (4.18)$$

For bond angles we then have

$$\kappa_{i+1} = 2\kappa_i - \kappa_{i-1} + \frac{dV[\kappa]}{d\kappa_i^2} \kappa_i \quad (i = 1, \dots, N) \quad (4.19)$$

where we set  $\kappa_0 = \kappa_{N+1} = 0$ , and  $V[\kappa]$  is given by (3.35). This equation is a deformation of the conventional DNLS equation, and it is not integrable, *a priori*. For a numerical solution, we extend (4.19) into the following iterative equation [76]

$$\kappa_i^{(n+1)} = \kappa_i^{(n)} - \epsilon \left\{ \kappa_i^{(n)} V'[\kappa_i^{(n)}] - (\kappa_{i+1}^{(n)} - 2\kappa_i^{(n)} + \kappa_{i-1}^{(n)}) \right\} \quad (4.20)$$

Here  $\{\kappa_i^{(n)}\}_{i \in N}$  denotes the  $n^{th}$  iteration of an initial configuration  $\{\kappa_i^{(0)}\}_{i \in N}$  and  $\epsilon$  is some sufficiently small but otherwise arbitrary numerical constant; we often choose  $\epsilon = 0.01$  in practical computations. The fixed point of (4.20) is clearly independent of the value chosen. But the radius and rate of numerical convergence in a simulation towards the fixed point, depends on the value of  $\epsilon$ : The fixed point is clearly a solution of (4.19).

Once the numerically constructed fixed point is available, we calculate the corresponding torsion angles from (4.18). Then, we obtain the frames from (4.6) and can proceed to the construction of the discrete string, using (4.7).

At the moment we do not know of an analytical expression of the soliton solution to the equation (4.19). But we have found [75, 77, 79] that an *excellent* approximative solution can be obtained by discretizing the topological soliton (3.29).

$$\kappa_i \approx \frac{m_1 \cdot e^{c_1(i-s)} - m_2 \cdot e^{-c_2(i-s)}}{e^{c_1(i-s)} + e^{-c_2(i-s)}} \quad (4.21)$$

Here  $(c_1, c_2, m_1, m_2, s)$  are parameters. The  $m_1$  and  $m_2$  specify the asymptotic  $\kappa_i$ -values of the soliton. Thus, these parameters are entirely determined by the character of the regular, constant bond and torsion angle structures that are adjacent to the soliton. In particular, these parameters are not specific to the soliton *per se*, but to the adjoining regular structures. The parameter  $s$  defines the location of the soliton

along the string. This leaves us with only two loop specific parameter, the  $c_1$  and  $c_2$ . These parameters quantify the length of the bond angle profile that describes the soliton.

For the torsion angle, (4.18) involves one parameter ( $a$ ) that we have factored out as the overall relative scale between the bond angle and torsion angle contributions to the energy; this parameter determined the relative flexibility of the torsion angles, with respect to the bond angles. Then, there are three additional parameters ( $b/a, c/a, d/a$ ) in the remainder  $\hat{\tau}[\kappa]$ . Two of these are again determined by the character of the regular structures that are adjacent to the soliton. As such, these parameters are not specific to the soliton. The remaining single parameter specifies the size of the regime where the torsion angle fluctuates.

On the regions adjacent to a soliton, we have constant values of  $(\kappa_i, \tau_i)$ . In the case of a protein, these are the regions that correspond to the standard regular secondary structures: In a rough sense, proteins are made of right-handed  $\alpha$ -helices,  $\beta$ -strands and loops. For example, the standard right-handed  $\alpha$ -helix is

$$\alpha - \text{helix} : \quad \begin{cases} \kappa \approx \frac{\pi}{2} \\ \tau \approx 1 \end{cases} \quad (4.22)$$

and the standard  $\beta$ -strand is

$$\beta - \text{strand} : \quad \begin{cases} \kappa \approx 1 \\ \tau \approx \pi \end{cases} \quad (4.23)$$

All the other standard regular secondary structures such as 3/10 helices, left-handed helices *etc.* are similarly described by definite constant values of  $\kappa_i$  and  $\tau_i$ .

Protein loops correspond to regions where the values of  $(\kappa_i, \tau_i)$  are variable, protein loops are the soliton proper: A soliton is a configuration that interpolates between two regular structures, with constant values of  $(\kappa_i, \tau_i)$ .

## 4.4 Proteins out of thermal equilibrium

When a protein folds towards its native state, it is out of thermal equilibrium. Several studies propose, that in the case of a small protein the folding takes place in a manner which is consistent with Arrhenius' law; we recall that Arrhenius' law states that the reaction rate depends exponentially on the ratio of activation energy  $E_A$  and temperature,

$$r \propto \exp\left\{-\frac{E_A}{k_B T}\right\}$$

On the other hand, in the case of simple spin chains it has been found that the *Glauber dynamics* [82, 83] describes the approach to thermal equilibrium in a manner which follows Arrhenius's law. Since we have argued that proteins can be viewed as spin chains, with residues corresponding to the spin variables, it is natural to try and model the way how a protein approaches thermal equilibrium by using Glauber dynamics.

Glauber proposed to model non-equilibrium dynamics in terms of a Markovian Monte Carlo (MC) time evolution, defined by the following heat bath probability distribution [82, 83]

$$\mathcal{P} = \frac{x}{1+x} \quad \text{with} \quad x = \exp\left\{-\frac{\Delta E}{k\mathcal{T}}\right\} \quad (4.24)$$

Here  $\Delta E$  is the energy difference between consecutive MC time steps ( $\sim$ activation energy). We compute it from (4.17) in the case of a protein. In addition, in the case of a protein we need to account for steric constraints: Analysis of PDB structures reveals, that the distance between two C $\alpha$  atoms which are *not* nearest neighbours along the backbone, is always larger than (4.12)

$$|\mathbf{r}_i - \mathbf{r}_k| > 3.8 \text{ \AA} \quad \text{for} \quad |i - k| \geq 2 \quad (4.25)$$

Note the apparent similarity between Arrhenius law and Glauber algorithm. We also note that the scale of units of  $k\mathcal{T}$  which appears in (4.24) as a temperature factor, should not be directly identified with the Boltzmannian temperature factor  $k_B T$ . The scale of units depends on the overall scale of the energy function (4.17), and in particular by our choice of the normalisation factor in the first, nearest neighbor interaction term. To determine the unit, we need a renormalisation condition. For this we need to perform a proper experimental measurement(s), and compare the predictions of our model to those of the protein that it describes, at that temperature. One suitable renormalisation point could be, to try and identify the experimentally measured  $\theta$ -transition temperature by comparison with the properties of our model.

## 4.5 Temperature renormalisation

*This section is somewhat technical. The details are not needed in the rest of the lectures. We include this section because we feel that good understanding of temperature renormalisation of parameters is relevant to physics of proteins [81]. For example, thus far this has not been really addressed in any other approach we are aware of. You might find the subject described here to be an inspiration for your future research.*

In the probability distribution (4.24) the nearest-neighbor coupling contribution in (4.17) becomes normalised as follows,

$$-\frac{2}{k\mathcal{T}} \sum_{i=1}^N \kappa_{i+1} \kappa_i \quad (4.26)$$

Thus the temperature factor  $k\mathcal{T}$  depends on the physical temperature factor  $k_B T$  in a non-trivial fashion. That is, we should really write

$$\frac{2}{k\mathcal{T}} \rightarrow \frac{J(T)}{k_B T} \quad (4.27)$$

where  $J(T)$  is the strength of the nearest neighbour coupling at Boltzmannian  $k_B T$ . Its numerical value depends on the temperature in a manner that is governed by the standard renormalisation group equation

$$T \frac{dJ}{dT} = \beta_J(J; \lambda, m, q, p, r) \sim \beta_J(J) + \dots \quad (4.28)$$

For simplicity we may assume that to leading order the dependence of  $\beta_J$  on the other couplings can be ignored. Note that the parameters and thus their  $\beta$ -functions, depend

on the properties of the environmental factors such as properties of solvent, the pH of solvent, pressure *etc.*

In the low temperature limit we can expand the nearest neighbour coupling as follows,

$$J(T) \approx J_0 - J_1 T^\alpha + \dots \quad \text{as } T \rightarrow 0 \quad (4.29)$$

Here the value of  $J_0$  is non-vanishing, and the critical exponent  $\alpha$  controls the low temperature behavior of  $J(T)$ . The asymptotic expansion (4.29) corresponds to a  $\beta$ -function (4.28) that in the  $T \rightarrow 0$  limit approaches

$$\beta_J(J) = \alpha(J - J_0) + \dots$$

Consequently, at low temperatures we have

$$k\mathcal{T} \approx \frac{2k_B}{J_0} T \quad (4.30)$$

In terms of the temperature factor, (4.28) translates into

$$T \frac{d}{dT} \left( \frac{1}{k\mathcal{T}} \right) = -\frac{1}{k\mathcal{T}} + \frac{1}{2k_B T} \beta_J \left( \frac{2k_B T}{k\mathcal{T}} \right) \quad (4.31)$$

We try to find an approximative solution in the collapsed phase, when the temperature  $T$  is below the critical  $\theta$ -point temperature  $T_\theta$  where the transition between the collapsed phase and the random walk phase takes place. This coincides with the physical temperature value that corresponds to the unfolding transition temperature factor value  $k\mathcal{T}_\Theta$ . Let

$$\beta_J \left( \frac{2k_B T}{k\mathcal{T}} \right) = \frac{2k_B T}{k\mathcal{T}} + F \left( \frac{2k_B T}{k\mathcal{T}} \right)$$

and define

$$y = \frac{1}{k\mathcal{T}}$$

$$x = \frac{1}{2k_B T}$$

The equation (4.31) then translates into

$$\frac{dy}{dx} = -F\left(\frac{y}{x}\right)$$

with the solution

$$\ln(cx) = - \int^{\frac{y}{x}} \frac{du}{F(u) + u}$$

Here  $c$  is an integration constant. We shall assume that the leading non-linear corrections are logarithmic; this is often the case. To the leading order we then have

$$F(u) = (\eta - 1)u + \alpha u \ln u + \dots$$

Note, that in general there are higher order corrections. When we re-introduce the original variables and set

$$\eta = -\alpha \ln J_0$$

we get for the temperature factor

$$\begin{aligned} k\mathcal{T} &\approx \frac{2}{J_0} k_B T \exp\left\{\frac{J_1}{J_0} T^\alpha\right\} \\ &\approx \frac{2}{J_0} k_B T + \frac{2J_1}{J_0^2} k_B T^{\alpha+1} + \dots \quad \text{as } T \rightarrow 0 \quad (\alpha > 0) \end{aligned} \quad (4.32)$$

where we have chosen the integration constant so that in the low temperature limit we obtain (4.30).

For the nearest neighbor coupling, (4.32) yields

$$J(T) \approx J_0 \exp\left\{-\frac{J_1}{J_0} T^\alpha\right\}$$

Thus the coupling between bond angles becomes weak, at an exponential rate, when the temperature approaches the transition temperature  $T_\theta$  between the collapsed phase and the random walk phase.

Similarly, all the other couplings that are present in (4.17) are temperature dependent. Each of them has its own renormalisation group equation. For example, the quartic  $\kappa_i$  self-coupling  $\lambda$  in (4.17) flows according to a renormalization group equation of the form

$$T \frac{d\lambda}{dT} = \beta_\lambda(\lambda) \quad (4.33)$$

For simplicity, we again assume that to the leading order the  $\beta_\lambda$  depends only on  $\lambda$ .

It is natural to interpret  $\lambda$  as a measure of the strength of hydrogen bonds: Structures such as  $\alpha$ -helices and  $\beta$  strands become stable, due to hydrogen bonds. At the same time, the value of  $\lambda$  controls the affinity of  $\kappa_i$  towards the ground state value of the quartic potential in (4.17). The hydrogen bonds are presumed to become vanishingly weak, when the protein unfolds. This can take place when the protein approaches the transition temperature  $T_\theta$  which separates the collapsed phase from the random walk phases. This proposes that asymptotically,

$$\lambda(T) \rightarrow \lambda_\theta |T - T_\theta|^{\gamma_\lambda} \quad \text{as } T \rightarrow T_\theta \text{ from below}$$

Here  $\gamma_\lambda$  is a critical exponent that controls the way how the strength of (effective) hydrogen bonds vanish. More generally, we may send  $T_\theta \rightarrow T_H$ , which is the temperature value where hydrogen bonds disappear even between the solvent molecules; in the case of water at atmospheric conditions  $T_H \approx 100^\circ\text{C}$ . In general, we expect that the value of  $T_H$  is higher than that of  $T_\theta$ .

Above  $T > T_\theta$ , when the hydrogen bonds become vanishingly weak, we expect that effectively  $\lambda \approx 0$  (or  $m \approx 0$ ) in (4.17). On the other hand, we expect that as the temperature decreases the value of  $\lambda(T)$  increases, so that in the low temperature limit we have

$$\lambda(T) \rightarrow \lambda_0 - \lambda_1 T^{\gamma_0} + \dots \quad \text{as } T \rightarrow 0$$

Thus

$$\beta_\lambda(\lambda) \approx \gamma_0(\lambda - \lambda_0) + \mathcal{O}[(\lambda - \lambda_0)^2]$$

Here  $\lambda_0$  should be close to the value we obtain from PDB, when we compute the parameters in (4.17) from the crystallographic low temperature structure.

*Research project:* Try to numerically evaluate the  $\beta$ -function (4.28) in the case of a simple protein, such as villin headpiece (PDB code 1YRF), using results from detailed experimental measurements.

*Research project:* Find out how the parameters in (1.11), (1.12) depend on temperature.

## 5

# Solitons and ordered proteins

---

Various taxonomy schemes such as CATH and SCOP [84,85] have revealed that folded proteins are built in a modular fashion, from a relatively small number of building blocks. Despite essentially exponential increase in the number of new crystallographic protein structures, novel fold topologies are now rarely found and some authors think that most modular building blocks of proteins are already known [30,86]. This convergence in protein architecture demonstrates that protein folding should be a process which is driven by some kind of universal structural self-organisation principle.

We know that solitons are the paradigm structural self-organisers. Thus we argue that the soliton solution of the DNLS equation (4.19), (4.18) must be the universal modular building block from which folded proteins can be constructed. Indeed, we know that the energy function (4.17) is unique, in the limit where it becomes applicable. Moreover, it has already been shown that over 92% of all C $\alpha$ -traces of PDB proteins can be described in terms of no more than 200 different parametrizations of the discretised NLS soliton (4.21), with a root-mean-square-distance (RMSD) precision which is better than 0.5 Å [78].

Accordingly, we set up to describe the modular building blocks of proteins in terms of various parametrizations of the DNLS soliton profile, which is described by the equations (4.20), (4.18), (4.6) and (4.7).

### 5.1 $\lambda$ -repressor as a multi-soliton

In order to identify the soliton structure of a given protein, we start by computing the C $\alpha$  virtual backbone bond and torsion angles from the PDB data. We *initially* fix the  $\mathbb{Z}_2$  gauge in (4.11) so that all the bond angles take positive values  $\kappa_i \in [0, \pi]$ . A generic protein profile consists of a set of  $\kappa_i$  with values that are typically between  $\kappa_i \approx 1$  and  $\kappa_i \approx \pi/2$ ; the upper bound can be estimated using steric constraints. The torsion angle values  $\tau_i$  are commonly much more unsettled, and their values extend more widely over the entire range  $\tau \in [-\pi, +\pi]$ .

As an example we consider the  $\lambda$ -repressor which is a protein that controls the lysogenic-to-lytic transition in bacteriophage  $\lambda$  infected *E. coli* cell. The transition between the lysogenic and lytic phases in bacteriophage  $\lambda$  infected *E. coli* is the paradigm example of genetic switch mechanism, which has been described in numerous molecular biology textbooks and review articles. See for example [87, 88]. The interplay between the lysogeny maintaining  $\lambda$ -repressor protein and the regulator protein that controls the transition to the lytic state is a simple model for more complex regulatory networks, including those that can lead to cancer in humans.



The  $\lambda$ -repressor structure we consider has PDB code 1LMB. It is a homo-dimer with 92 residues in each of the two monomers. It maintains the lysogenic state by binding to DNA with a helix-turn-helix motif which is located between the residue sites 33-51.

The  $\lambda$ -repressor is a fast-folding protein: In [38] an 80-residue long mutant of the  $\lambda$ -repressor was studied in all-atom simulation.

In figure 5.1 (left column) we show the  $(\kappa_i, \tau_i)$  spectrum of 1LMB, with the convention (i.e.  $\mathbb{Z}_2$  gauge fixing) that  $\kappa_i$  is positive. We display the segments between residues 19-82. We note that this spectrum is fairly typical, for the PDB structures we have analysed.

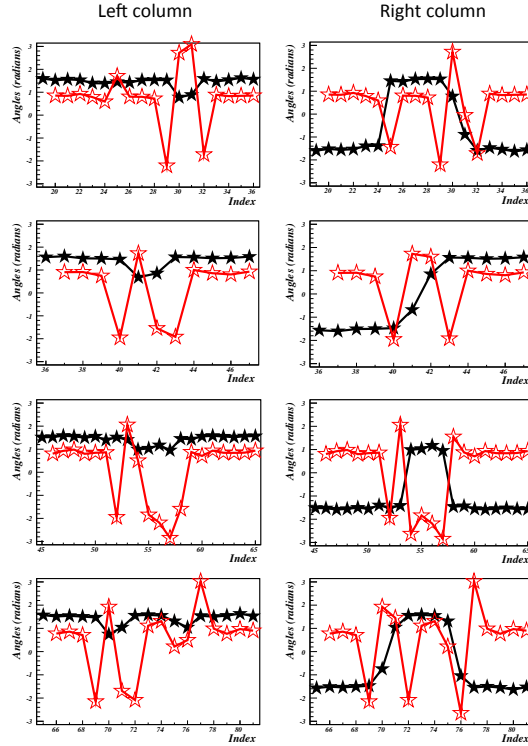


**Fig. 5.1** The bond angle ( $\kappa$ ) and torsion angle ( $\tau$ ) spectrum of  $\lambda$ -repressor 1LMB, with indexing that follows PDB. The left column shows the spectrum in the  $\mathbb{Z}_2$  gauge where all  $\kappa_i > 0$  and the right column shows the spectrum after we have implemented the  $\mathbb{Z}_2$  gauge transformations that identify the solitons.

The results in Section 3.8 suggests that in analysing the PDB data, one should first pay attention to flattening points i.e. points where  $\tau_i$  changes its sign. The flattening points should be located near a putative inflection point where a soliton is located and perestroika takes place. Accordingly, we perform in the spectrum of Figure 5.1 left

column the  $\mathbb{Z}_2$  gauge transformations (4.11) in the vicinity of the apparent flattening points, to identify the putative multi-soliton profile of  $\kappa_i$ . For example, in the case of 1LMB we observe four regions with an irregular  $\tau_i$  profile as shown in Figure 5.1. By a judicious choice of  $\mathbb{Z}_2$  gauge transformations we identify seven different solitons in  $\kappa_i$ . The profiles are shown in the right column of Figure 5.1. Each of the soliton profiles is clearly accompanied by putative flattening points. Note that  $\tau_i$  is multi-valued,  $\text{mod}(2\pi)$ . Thus the large fluctuations in the values of  $\tau_i$  are deceitful. Once you account for the multivaluedness, you find that  $\tau_i$  is actually quite regular. This is in full accordance with the observed, much higher flexibility of the torsion angles in relation to the bond angles, which is known to occur in proteins.

On the basis of the general considerations in Section 3.8, we argue that protein folding from a regular unfolded configuration with no solitons to the biologically active natively folded configuration with its solitons is a process which is driven by inflection and flattening point perestroika's. The initial configuration with no solitons can be chosen to coincide with the minimum of the second sum in (4.17). It could also be e.g. a uniform right-handed  $\alpha$ -helix (4.22), or  $\beta$ -strand (4.23), or a polyproline-II type conformation. When the protein folds it proceeds from this initial configuration towards the final configuration, thru successive perestroika's *i.e.* bifurcations. These perestroika's deform the  $C\alpha$  backbone, creating DNLS-like solitons along it and thus causing the backbone to enter the space-filling  $\nu \sim 1/3$  collapsed phase.

In the case of 1LMB, we identify seven soliton profiles as shown in Figure 5.1 (right column). We proceed to determine the parameters in the energy function (4.17). For this we train the energy function so that it describes the seven individual solitons in terms of a solution of (4.19), (4.18), for each of them individually. The training is performed by demanding that the fixed point of the iterative equation (4.20) models the ensuing  $C\alpha$  backbone structure as a soliton solution, with a prescribed precision.

We have developed a program *GaugeIT* that implements the  $\mathbb{Z}_2$  gauge transformations to identify the background, and we have developed a program *PropoUI* that trains the energy so that it has an extremum which models the background in terms of solitons. These programs are described at

$$\text{http} : // \text{www.folding} - \text{protein.org} \quad (5.1)$$

In the case of a protein for which the PDB structure is determined with an ultra-high resolution, typically below 1.0 Ångström, *PropoUI* routinely constructs a soliton solution that describes the  $C\alpha$  backbone with a precision which is comparable to the accuracy of the experimentally measured crystallographic structure; recall that the accuracy of the experimental PDB structure is estimated by the B-factors using the Debye-Waller relation (1.4).

In figure 5.2 we compare the distance between the  $C\alpha$  backbone, and the seven individual soliton solutions for 1LMB. The B-factor fluctuation distance in the experimental structure 1LMB, evacuated from the Debye-Waller relation, is also displayed. As shown in the Figure, the solitons describe the loops with a precision that is fully comparable with the experimental uncertainties. The grey zone around the soliton profile denotes our best estimate for the extent of quantum mechanical zero-point fluctuations; according to Figure (1.4) there are practically no Debye-Waller values

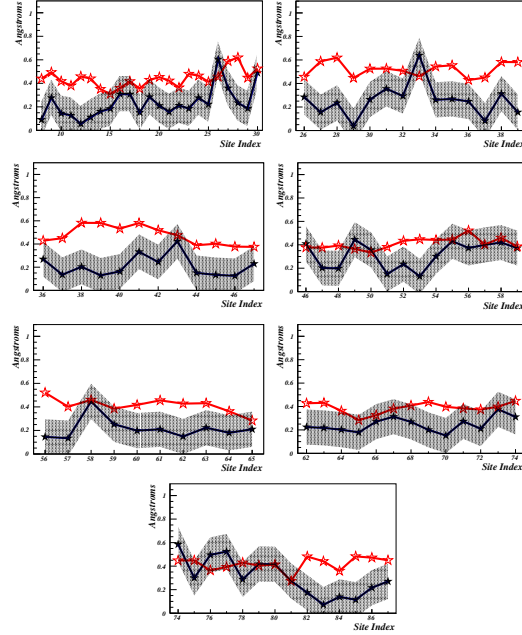


**Fig. 5.2** The distance between the PDB backbone of the first 1LMB chain and its seven solitons. The black line denotes the distance between the PDB structure and the corresponding soliton. The grey area around the black line describes the lower bound estimate of 15 pico meter (quantum mechanical) zero point fluctuation distance around each soliton, obtained from Figure (1.4). The red line denotes the Debye-Waller fluctuation distance (1.4).

less than 15 pico meters, which we have chosen here as the zero point fluctuation distance, in the Figure.

## 5.2 Structure of myoglobin

Myoglobin [9] is the primary oxygen-carrying protein in the muscle cells of mammals. Myoglobin is closely related to haemoglobin, which is the oxygen binding protein in blood. Myoglobin gives meat its red color; the more red, the more myoglobin. Myoglobin also allows organisms to hold their breath, for a period of time. Diving mammals such as whales and seals have a high myoglobin concentration in their muscles.

Myoglobin is the first protein to have its three-dimensional structure determined by x-ray crystallography. Subsequently myoglobin has remained among the most actively studied proteins. But theoretically, the investigation of myoglobin *e.g.* in an all-atom molecular dynamics simulation remains a formidable task: The experimentally measured folding time from a random chain to the natively folded state is around 2.5 seconds [89]. At the same time, the fastest ever built special purpose MD supercomputer *Anton* can produce at most a few microseconds of *in vitro* folding trajectory per day *in silico*, in the case of proteins that are much shorter and simpler than myoglobin.

Accordingly it would take at least a million or so days to reproduce a *single* myoglobin folding trajectory *in silico*, at all-atom level, even with *Anton*. A good convergence of Newton's iteration with the energy function (1.11), (1.12) over such a long time scale would be truly amazing.

We have already noted that all-atom MD simulation is conceptually a weak coupling expansion, appropriate for describing phenomena over very short time periods only: The time ratio (1.13) is the small, iterative expansion parameter. In the case of long time trajectories, such a weak coupling expansion can not be expected to be very effective, not even convergent. Alternative approximative methods need to be introduced, to model myoglobin and the large majority of proteins that fold much slower than the microsecond-to-millisecond scale.

From the perspective of quantum field theory this means that we need a non-perturbative approach. For example, in QCD we do not expect that standard perturbation theory is capable of describing hadrons. On the other hand, lattice QCD is designed for modelling hadrons. But it can hardly describe the scattering of quarks and gluons.

Indeed, we have argued that in the case of proteins, the energy function (4.17) is an example of such a non-perturbative approach. It avoids altogether the need to introduce a time step ratio such as (1.13), as a weak coupling expansion parameter. Instead the  $C\alpha$  geometry is modelled in terms of small variations in the angular variables, around their equilibrium conformations. Since the approximation does not engage time directly, it becomes in principle possible to describe folding phenomena that can be very difficult, even impossible, to model in terms of conventional and presently available all-atom MD.

We proceed to apply the energy function (4.17) to investigate detailed properties of myoglobin. In this Section we analyse the static structure and in the next Section we consider out-of-equilibrium dynamics.

We first construct the multi-soliton solution that models the myoglobin backbone. We use the crystallographic PDB structure 1ABS as a decoy, to train the energy function. This structure has been measured at very low liquid helium temperatures  $\sim 20$  K. Thus the thermal B-factor fluctuations (1.4) are small.

We propose that at this point, the reader downloads the PDB structure 1ABS, to make it easier to follow details of our analysis. We propose to use the Java interface provided at the PDB site (1.2) for visualisation of the backbone and side-chain atoms. We also recommend the analysis tools available on the website of *Molprobity* (1.3) which we shall refer to in the following. We shall provide the values for all the parameters in the energy function (4.17) which the reader can use as input in the programs *Propro* and *GaugeIT*, that are described at our website (5.1). This enables a detailed analysis of the multi-soliton that describes 1ABS, and should help the reader to start his/her independent research.

We proceed to the construction of the multi-soliton: 1ABS has 154 amino acids, and the PDB index runs over  $i = 0, \dots, 153$ . Conventionally one identifies the structure as a bundle of eight  $\alpha$ -helices (A,B,C,...,H) which are separated by 7 loops as shown in Figure 5.3.

Here we shall limit the construction of the multi-soliton to the sites with PDB index between  $N=8-149$ . That is, we include all the named helices but we do not include the

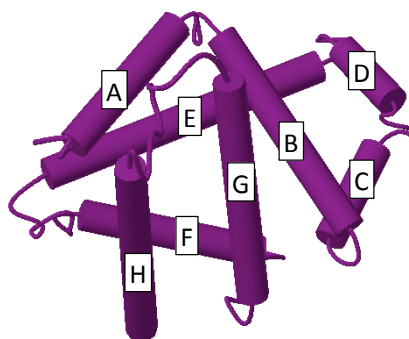


**Fig. 5.3** Myoglobin has 8  $\alpha$ -helices that are named A,B,C, ... , H

flexible tails at the ends of the backbone. These tails could be included, but without much additional insight to the issues that we address.

In Figure (5.4) (top) we show the backbone bond and torsion angle spectrum with the convention that all  $\kappa_i$  are positive. In Figure (5.4) (bottom) we show the spectrum after we have implemented the  $\mathbb{Z}_2$  transformations (4.11) to putatively identify the multi-soliton profile; we use the program packages *Propro* and *GaugeIT* that are described at our website (5.1) in our analysis.

We remind that both the top and bottom of Figure (5.4) correspond to the same intrinsic backbone geometry. The  $\mathbb{Z}_2$  transformation is a symmetry of the discrete string which is obtained by solving the discrete Frenet equation.

We conclude from the  $\kappa_i$  profile of the bottom Figure (5.4) that the myoglobin backbone has eleven helices that are separated by ten single soliton loops. The number of loops and helices is more or less unambiguously determined by the number of inflection points which we identify visually in Figure (5.4), in the manner explained in Section 3.8. The PDB sites of the ten individual soliton profiles that we use for our construction, are identified in Table 5.1. We *emphasise* that our geometry based identification of the loops and helices along the 1ABS backbone does not necessarily need to coincide with the conventional one used e.g. in crystallography, which is based on inspection of hydrogen bonds. In particular, according to the conventional classification, the soliton pair 3 and 4, the soliton pair 6 and 7, and the soliton pair 9 and 10, are all interpreted as a single loop. From our geometric point of view, the PDB data reveals that in 1ABS, we have four different types of solitons. Those that connect two  $\alpha$  helices, those that connect an  $\alpha$ -helix with a 3/10-helix or vice versa, and finally, those that connect two 3/10-helices; see Table 5.1.

In Table 5.2 we give our parameter values for the multi-soliton solution. It describes the 1ABS backbone with 0.78 Å RMSD accuracy. Note that in those terms in (4.17) which engage the torsion angles, the numerical parameter values are consistently much smaller than in terms that contain only the bond angles. This is in line with the known fact, that in proteins the torsion angles i.e. dihedrals are usually quite flexible while the bond angles are relatively stiff.

Note also that our energy function has 80 parameters, while there are 153 amino

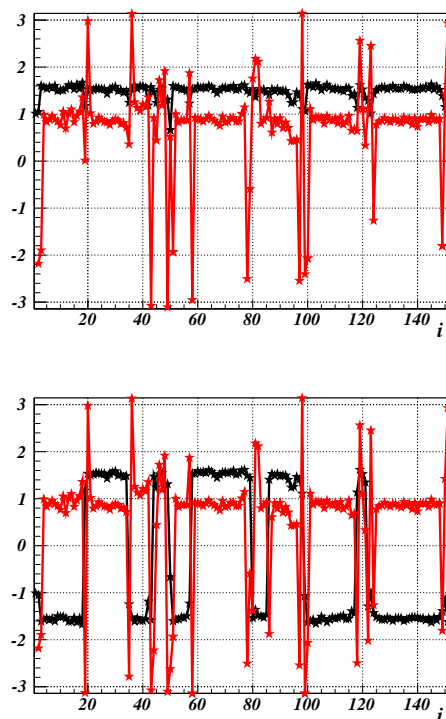


**Fig. 5.4** Top: The  $\kappa_i$  (black) and  $\tau_i$  (red) profiles of 1ABS using the standard differential geometric convention that bond angles are positive. Bottom: The soliton structure becomes visible in the  $\kappa_i$  profile once we implement the transformations (4.11).

acids in the entire myoglobin backbone. Thus the energy function (4.17) is *highly predictive*: The number of free parameters is even *less than the number of amino acids*. This shows that myoglobin displays structural redundancy, in its amino acids.

The predictive power of (4.17) can alternatively be characterised as follows: When we assume that all the bond lengths have the constant value (4.12), we are left with 282  $C\alpha$  angular coordinate values in our truncated backbone. These we need to determine from the properties of the energy function (4.17), in order to construct the backbone from (4.6), (4.7). We have a total of 80 parameters in Table 5.2, thus a total of 202 coordinates remain to be determined by the multi-soliton solution that minimises the energy function. Therefore, we have 202 unknowns which are to be *predicted* by the model. These predictions then directly probe the physical principles on which (4.17) has been built.

We remind that approaches such as the Gō model and its variants and various elastic network models lack this kind of predictive power. In those models the positions of *all* the atoms are assumed to be known *a priori*. In addition one needs a description how the atoms interact. Thus there are always *more parameters* than degrees of

**Table 5.1** The solitons along the 1ABS C $\alpha$ -backbone, with indexing starting from the N terminus. We have left out the end sites that correspond to monotonous helices, and the N and C termini segments. The type identifies whether the soliton corresponds to a loop that connects  $\alpha$ -helices and (or) 3/10-helices.

soliton	1	2	3	4	5
sites	15-27	30-41	39-49	47-57	54-66
type	$\alpha$ - $\alpha$	$\alpha$ -3/10	3/10-3/10	3/10-3/10	3/10- $\alpha$
soliton	6	7	8	9	10
site	72-87	83-92	94-106	110-123	121-135
type	$\alpha$ - $\alpha$	$\alpha$ - $\alpha$	$\alpha$ - $\alpha$	$\alpha$ - $\alpha$	$\alpha$ - $\alpha$

freedom, and no predictions can be made.



**Fig. 5.5** Comparison between the PDB structure 1ABS (dark purple) and the corresponding multi-soliton solution (light blue).

In Figure 5.5 we interlace the 1ABS backbone with the multi-soliton; the difference is very small.

In Figure 5.6 we analyse site-wise the precision of the multi-soliton configuration with the PDB structure 1ABS. The 15 pico-meter gray-scaled region around the multi-soliton profile corresponds again to the regime of zero point fluctuations, that we have deduced from Figure 1.4. Conceptually, the multi-soliton describes a *single* myoglobin structure in the limit of vanishing temperature. In particular, as such the multi-soliton does not account for any kind of conformational fluctuations that are due to thermal effects, lattice imperfections, or any other kind of conformational sub-state effects; we model thermal effects using the Glauber heat bath (4.24). On the other hand,

## 62 Solitons and ordered proteins

**Table 5.2** Parameter values in energy (4.17) for the multi-soliton solution that describes 1ABS.

soliton	$\lambda_1$	$\lambda_2$	$m_1$	$m_2$
1	9.923	2.232	1.54097	1.54548
2	6.48516	0.9955	1.58013	1.54058
3	2.05153	0.657	1.66032	1.60224
4	0.89676	6.74235	1.3563	1.5232
5	9.26118	0.83376	1.55206	1.5386
6	0.98018	2.1337	1.45791	1.54653
7	1.37667	3.16891	1.47151	1.04128
8	10.3168	4.2801	1.18192	1.61334
9	0.80042	1.28973	1.5154	1.60278
10	3.15255	0.91475	1.55827	1.55151
soliton	$a$	$b$	$c$	$d$
1	-5.62412 e-08	-4.13459 e-07	1.81044 e-08	4.273 e-09
2	-6.25287 e-11	-1.68598 e-05	1.47093 e-07	2.82807 e-07
3	-9.05135 e-08	1.20232 e-06	5.10166 e-11	5.75389 e-09
4	-2.33413 e-07	-3.3991 e-07	2.36516 e-08	7.98841 e-09
5	-9.73035 e-08	4.78674 e-07	1.03189 e-10	4.88194 e-09
6	-7.25906 e-09	3.76092 e-09	6.82624 e-10	1.87212 e-14
7	-1.39052 e-13	5.97719 e-13	3.77897 e-14	5.81911 e-14
8	-1.27193 e-07	1.41736 e-06	1.07182 e-10	1.26295 e-08
9	-2.03487 e-07	1.13574 e-06	1.46007 e-11	7.82707 e-08
10	-1.07811 e-07	1.02768 e-06	7.49571 e-11	7.73639 e-09

the experimentally measured 1ABS crystal structure should not be interpreted as a single static low temperature structure. Instead, it is an average over a large number of closely packed crystallographic structures. A comparison between Figures 5.2 and 5.6 shows that in the latter, the distance between the PDB backbone and the multi-soliton profile is larger than that between the PDB backbone and the individual solitons in Figure 5.2. The Figure 5.6 describes the *single* multi-soliton solution to the equations (4.19), (4.18) while in Figure 5.2 we have constructed the individual solitons by solving (4.19), (4.18) independently for each loop. A similar individual soliton construction in the case of 1ABS gives profiles that are comparable, even slightly more precise, than those in Figure 5.2. But for energetic studies we need the full multi-soliton with its energy function, we need the local energy minimum of (4.17) for the *entire* backbone.

We presume that a multi-soliton solution could be constructed with a precision even better than 0.78 Å in C $\alpha$  RMSD. But the convergence of (4.20) becomes slow when we use a laptop like MacAir. Thus we have simply terminated the process when we reach the value 0.78 Å which is in any case much better than that obtained in any other approach, using any other computer, to our knowledge.

In Figure 5.6 we observe that the distance between the multi-soliton solution and



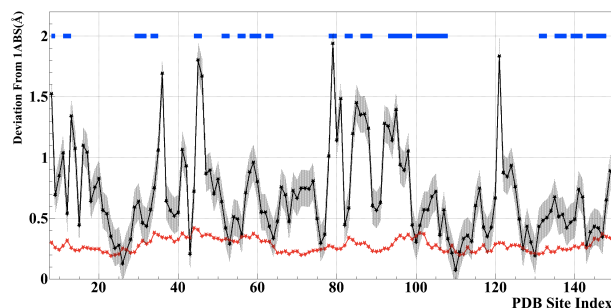


**Fig. 5.6** Comparison of the RMSD distance between the 1ABS configuration and the multi-soliton solution, with the Debye-Waller B-factor fluctuation distance around the 1ABS backbone. The blue marking at top, along 2.0 Å line, denotes sites where *Molprobity* (1.3) detects imperfections.

the C $\alpha$  carbon backbone of 1ABS has its largest values mainly in two regimes. These are located *roughly* between the sites 35-45, and between the sites 79-98; we propose the reader inspects the structure of 1ABS using the visualisation interface of PDB. The first regime corresponds to the single soliton that models the loop between helix B and helix C in Figure 5.3. The second regime corresponds to the location of the helix F. This helix is part of the "V"-shaped pocket of helices E and F, where the heme group is located. In particular, the reader can observe that helix F includes the proximal histidine at site 93, which is bonded to the iron ion of the heme. Note that in addition, our analysis detects an anomaly at around site 121.

In order to understand the origin of the observed deviations from an ideal multi-soliton crystal, we check for the presence of potential structural disorders in 1ABS using *Molprobity* (1.3); we recommend the reader performs this analysis on the *Molprobity* web-site. In Figure 5.5, along the top, at the level of the 2.0 Å line, we have marked with blue those regions where according to *Molprobity* we have potential clashes. The *Molprobity* clash score of 1ABS is 20.32 which puts it in the 10th percentile among structures with comparable resolution, 100 being the best score. The regions of potential structural clashes correlate with those regions, where our multi-soliton profile has the largest deviations from the 1ABS backbone. Except the vicinity of the site 121, which is unproblematic according to *Molprobity*.

We first consider the difference between the multi-soliton and the 1ABS backbone around the sites 79-98, that was also identified by the *Ansatz* as a potentially troublesome one. The difference appears to be largely due to a deformation of the helix F. It could be caused by a bond between the proximal histidine at site 93 and the oxygen binding heme iron. This might introduce a strain which modifies the backbone. The effect of the heme is not accounted for by our energy function, in the present form. Consequently we propose the histidine-heme interaction to be the likely explanation for the relatively large deviation between our multi-soliton profile and the 1ABS backbone, at this position.

We proceed to consider the difference between the multi-soliton and the 1ABS backbone around the sites 35-45. These sites are also located very close to the heme.

For example, the distance between the C $\alpha$  carbon at site 45 (Arg) and the hem oxygen 154 is 4.84 Å, and the C $\alpha$  of Phe at site 43 is even closer to the heme. This proximity between the backbone and the heme is reflected in the *Molprobability* clash at site 45 (between C $\delta$  and 154 HEM). We conclude that there could be strain in the backbone structure which is due to the heme, and this could explain the difference between 1ABS backbone and the multi-soliton configuration in this regime.

Finally, we note that in Figure 5.6, we also have our previously observed anomaly at site 121 (glycine). At this point, we have no explanation for the anomaly except that glycine is flexible and that this region is on the exterior of the protein. This leaves the hydrophobic phenylalanine at nearby site 123 exposed to the solvent. Consequently relatively strong fluctuations between several locally conformationally different but energetically degenerated sub-states are possible.

### 5.3 Dynamical myoglobin

The myoglobin stores O<sub>2</sub> by binding it to the iron atom, which is inside the myoglobin. The oxidation causes a conversion from ferrous ion (Fe<sup>2+</sup>) to ferric ion (Fe<sup>3+</sup>); the oxidised molecule is called oxymyoglobin. When the oxygen is absent, the molecule is called deoxymyoglobin. We propose the reader finds examples of each from PDB, and inspects the structures using the 3D Java interface.

Numerous detailed experimental investigations have been made both of oxymyoglobin and deoxymyoglobin. But to our knowledge, the understanding of the oxygen transport mechanism in myoglobin remains incomplete: We do not yet know exactly, how small non-polar ligands such as O<sub>2</sub>, CO and NO move between the external solvent and the iron containing heme group, which is located inside the myoglobin. From the available static crystallographic PDB structures one can not identify any obvious ligand pathway. It has been proposed that the process involves thermally driven large scale conformational motions. Collective thermal fluctuations could open and close gates through which the ligands migrate. Such gates are not necessarily visible in the crystallised low temperature structures. Computational investigations that model the dynamics of myoglobin might provide a clue how these gates operate.

#### 5.3.1 Glauber dynamics and phase structure

We start our investigation how ligand gates might open and close, by performing heating and cooling simulations of myoglobin with the energy function (4.17) in combination with Glauber dynamics (4.24), (4.25) [80]. We use the 1ABS multi-soliton we have constructed. The structure is a carbon-monooxy-myoglobin (MbCO), but with the covalent bond between the CO and iron broken by photodissociation. In any case, its dynamical properties should serve as a good first-approximation model how myoglobin behaves, more generally.

We start our simulations at a low temperature value, from the multi-soliton configuration that we have constructed: A classical soliton solution is commonly interpreted as a structure that describes the limit of vanishing temperature where thermal fluctuations become very small.

We take

$$k\mathcal{T}_L = 10^{-16}$$

for the numerical value of the low temperature factor, in terms of the dimensionless unit that is determined by our choice of the overall energy scale in (4.17). At this value of the temperature factor thermal fluctuations are absent in our multi-soliton. For the numerical high temperature value we choose

$$k\mathcal{T}_H = 10^{-13}$$

By applying the renormalisation group arguments in Section 4.5 we have related the two temperature factors  $k\mathcal{T}$  and  $k_B T$ . Our conversion relation that we shall justify in the sequel, is

$$k\mathcal{T} = 1.6181 \cdot 10^{-9} k_B T \exp\{0.05506 T\} \quad (5.2)$$

We use CGS units so that  $k_B = 1.381 \times 10^{-16} \text{ erg/K}$ .

Under *in vivo* conditions myoglobin always interacts with water. This interaction is essential for maintaining the collapsed phase. In our approach we account for the solvent (water) implicitly, in terms of the parameter values in (4.17). In particular, as such our model can only *effectively* take into account the highly complex phase properties of water at sub-freezing temperatures. We do not even try to address the obvious complications that appear when the temperature raises above the boiling point of water.

We start the simulation at  $k\mathcal{T}_L$ . The heating takes place with an exponential rate of increase during 5 million Monte Carlo steps. We model the non-equilibrium response using the Glauber protocol (4.24). According to (5.2) in terms of physical temperature factor  $k_B T$ , the heating process should correspond to an adiabatically slow nearly-linear rate of increase.

When we arrive at the high temperature  $k\mathcal{T}_H = 10^{-13}$  we fully thermalise the system by keeping it at this temperature value during 5 million steps. We then proceed to cool it back down to  $k\mathcal{T}_L$ . We use the same rate of cooling as we use for heating, *i.e.* we cool exponentially in  $k\mathcal{T}$  during 5 million steps. Each complete heating-cooling cycle takes about 3 minutes of wall-clock time when we use a single processor in a standard laptop (MacAir). Consequently time is no constraint for us and we can collect very, very good statistics. In particular, we have checked that our results and conclusions are quite insensitive to the rate of heating and cooling.

For statistical purposes, we have performed 100 repeated heating and cooling cycles that we have then analysed in detail; an increase in the number of cycles does not change our conclusions. Note that in an all-atom approach a comparable simulation would take over 100.000 years even with *Anton* [36] while for us a few minutes is enough.

During the simulations, we follow the evolution of both the radius of gyration  $R_g$  and the RMSD distance  $R_{rmsd}$  between the simulated configuration and the folded 1ABS structure. In Figure 5.7 a) we show the evolution of the radius of gyration, and in Figure 5.7 b) we show the evolution of the RMSD distance to 1ABS, as a function of steps during our 100 repeated heating and cooling cycles; Note that in these Figures we have converted the temperature into Kelvin scale, using (5.2).

We make the following observations: At low temperatures, with temperature factors

$$k\mathcal{T} < 10^{-15}$$

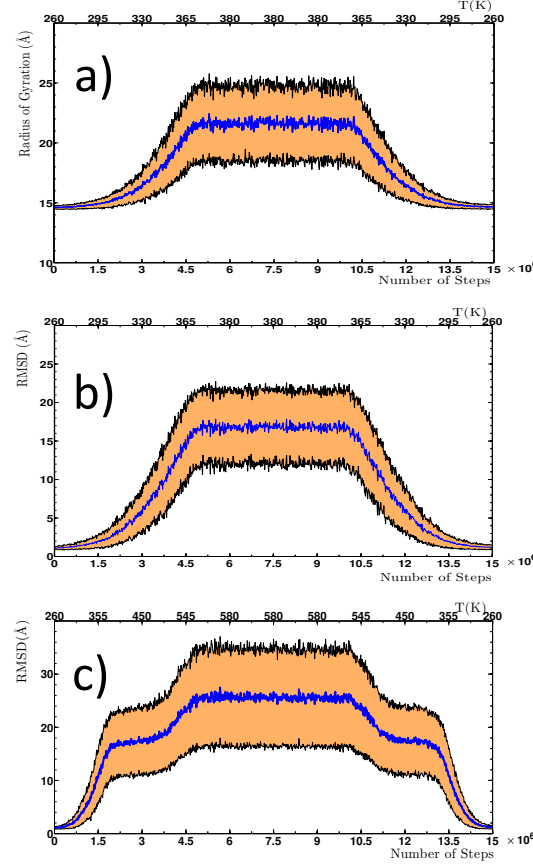


**Fig. 5.7** a) The evolution of the radius of gyration during 100 repeated heating and cooling cycles. b) The evolution of the RMSD distance between the 1ABS backbone and the simulated configuration during 100 repeated heating and cooling cycles. c) The evolution of the RMSD distance between the 1ABS backbone and the simulated configuration during 100 repeated heating and cooling cycles, to very high temperature values. In each Figure the (blue) line denotes the average, and the shaded area around it is the extent of one standard deviation fluctuations. Along the top axis, we show the temperature in the Kelvin scale, using the conversion relation (5.2).

the radius of gyration is essentially constant  $R_g \approx 14.6$  and only subject to very small thermal fluctuations. Between

$$10^{-15} < k\mathcal{T} < 10^{-14}$$

we have a regime when the radius of gyration increases at an accelerating rate in the number of steps. The increase in  $R_g$  continues until we reach a temperature near  $k\mathcal{T}_H$ . But for temperatures where the temperature factor is in the range

$$10^{-14} < k\mathcal{T} < k\mathcal{T}_H = 10^{-13}$$

the rate of increase decelerates so that when we reach the temperature  $k\mathcal{T}_H$  we observe no increase in  $R_g$ . This proposes that we have reached the random walk  $\theta$ -regime. Furthermore, the radius of gyration value

$$R_g \approx 22 \text{ \AA}$$

is *extremely* close to the experimentally measured value  $\sim 23.6 \text{ \AA}$  for the molten globule state of myoglobin. The difference can be entirely attributed to the 12 residues that we have excluded (7 from the N-terminal and 5 from the C-terminal) when constructing the multi-soliton.

We have confirmed that the transition near  $k\mathcal{T}_H$  is indeed a  $\theta$ -transition between collapsed phase and random walk phase, by heating the configuration to substantially higher temperature factor values. We have found that above this putative  $\theta$ -transition, the radius of gyration remains essentially intact under temperature variations all the way to

$$k\mathcal{T} = 10^{-8}$$

Around this temperature value another transition takes place, presumably to the  $\nu \sim 3/5$  self-avoiding random walk phase. In Figure 5.7 c) we show how the RMS distance between the heated configuration and 1ABS changes as a function of temperature, during heating and cooling cycles between  $k\mathcal{T}_L = 10^{-16}$  and  $k\mathcal{T} = 10^{-8}$ . We observe two clear transitions that are consistent with the transitions between collapsed and random walk phases, and between random walk and self-avoiding random walk phases according to (1.7).

When we decrease the temperature, the evolution of  $R_g$  becomes inverted. At the end of the cycle, when the temperature reaches  $k\mathcal{T}_L$ , the configuration returns back to a very close proximity of the original folded state; see Figure 5.7 b). This demonstrates the stability of the multi-soliton solution that describes the natively folded myoglobin as a local minimum of the energy (4.17).

Figure 5.8 a) shows the average values of  $R_g$ . These averages are evaluated at several different temperature values, over 100 runs. Both during the heating period when  $0 < x < 7.5$ , and during the cooling period when  $7.5 < x < 15$  where  $x$  is the number of MC steps in millions. The data can be approximated by a fitting function of the form

$$R_g(x) \approx a \cdot \tanh\{b(x - c)\} + d \quad (5.3)$$

The parameter values are listed in Table 5.3.

**Table 5.3** Parameter values in the fits (5.3), (5.5) for the two ranges 0 - 7.5 and 7.5 - 15 (in million) of iteration steps

range	$R_g$				$R_{rmsd}$			
	a	b	c	d	a	b	c	d
0 - 7.5	3.519	0.9047	3.6855	18.29	7.9	0.8318	3.5715	9.291
7.5 - 15	-3.486	0.9193	11.2965	18.28	-7.872	0.8327	11.4255	9.298

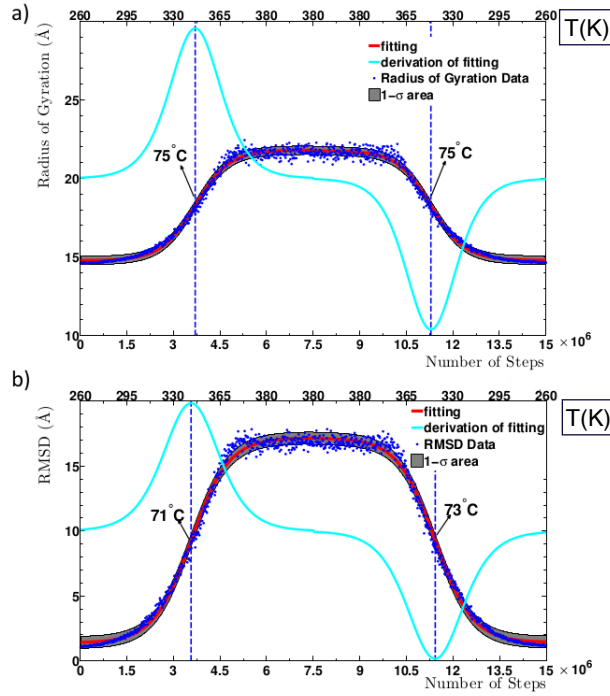


**Fig. 5.8** The red line is the fitting of (5.3) to the average values of blue dots which are the numerically computed values of  $R_g$ , over the heating and cooling periods. The shaded area around the red fitting line is one standard deviation estimate. Note: The difference between these three is so small that it is barely observable in the Figure. Also shown is the derivative of (5.3) (light blue line). Along the top axis, we have converted the temperature into Kelvin scale.

In Figure 5.8 a) we display the derivative of (5.3). We can try and use the maximum of the derivative to identify the  $\theta$ -transition temperature in our model. For this, we assume that the experimentally measured [90,91] transition temperature at  $T_c \approx 348\text{ K}$  is the one that corresponds to the  $\theta$ -transition. We identify it with the maximum of the derivative of  $R_g$ , to conclude that during the heating cycle the  $\theta$ -transition temperature relates to our dimensionless temperature values as follows,

$$\mathcal{T}_g^h \approx 1.63 \cdot 10^{-14} \approx 348\text{ K} \quad (5.4)$$

We use this value to determine one of the two parameters in (5.2).

During the cooling cycle, we find the slightly different

$$\mathcal{T}_g^c \approx 1.71 \cdot 10^{-14} \approx 349\text{ K}$$

We note that an asymmetry between heating and cooling has been observed experimentally [90].

The RMSD distance between the simulated configuration and the 1ABS backbone depends on temperature in a very similar manner. In Figure 5.8 b) we show the comparison between simulation, and the corresponding approximation (5.3),

$$R_{rmsd} \approx a \cdot \tanh\{b(x - c)\} + d \quad (5.5)$$

These parameter values are also listed in Table 5.3 separately for the heating period  $0 < x < 7.5$  and for the cooling period  $7.5 < x < 15$ . The Figure 5.8 b) also shows the derivative of  $R_{rmsd}(x)$ . Like in the case of radius of gyration, we use the maximum of the derivative to estimate the peak rate of change in the transition temperature. During the heating period the increase in  $R_{rmsd}$  peaks at

$$\mathcal{T}_{rmsd}^h \approx 1.35 \cdot 10^{-14} \approx 344 \text{ K}$$

During the cooling period we find that the peak corresponds to a slightly higher temperature value,

$$\mathcal{T}_{rmsd}^h \approx 1.45 \cdot 10^{-14} \approx 346 \text{ K}$$

These values are very close to those we observe in the case of  $R_g$ .

### 5.3.2 Backbone ligand gates

We proceed to try and identify potential thermally driven backbone ligand gates. We are interested in studying how the gates open and close as the myoglobin is heated and cooled. Moreover, thus far we have fixed only one of the two parameters in (5.4) using the  $\theta$ -transition temperature. We shall fix the second parameter in the sequel, by considering the dynamics of the backbone ligand gates.

We investigate the shape of the backbone visually, during the heating and cooling. We find that qualitatively the thermal fluctuations follow a very similar pattern. The backbone becomes unfolded in more or less the same manner, again and again, as the temperature becomes increased. The inverse pattern is observed during the cooling.

During heating we observe a clear onset of the unfolding transition, which we characterise in terms of backbone ligand gates. We have identified three major gates that we call Gate 1, 2 and 3, and we define them as follows:

The Gate 1 shown in Figure 5.9 a) is defined as the area between the segment that starts from PDB site 37 (Pro) and ends at PDB site 44 (Asp), and the segment that starts at 96 (Lys) and ends at 103 (Tyr). The opening of this gate takes place as the distance between the two segments increases. The open gate exposes the heme to the solvent. Figure 5.9 a) shows the location of this gate along the 1ABS backbone.

The Gate 2 is located between the helical structures E and F, as shown in 5.9 b). This gate extends over the entire length of both helices E and F. Thus, in order to compare it with Gate 1 that is composed of segments with only eight residues, we select two opposing segments along helices E and F, each with eight amino acids. The first segment, located in the helical structure E, starts with site 61 (Leu) and ends with site 68 (Val). The second segment, located in the helical structure F opposite to the first segment, starts with site 89 (Leu) and ends with site 96 (Lys). We have intentionally selected these two segments to be far from the loop that connects the helices E and F. This is because in our simulations, we have observed that the amplitudes of the

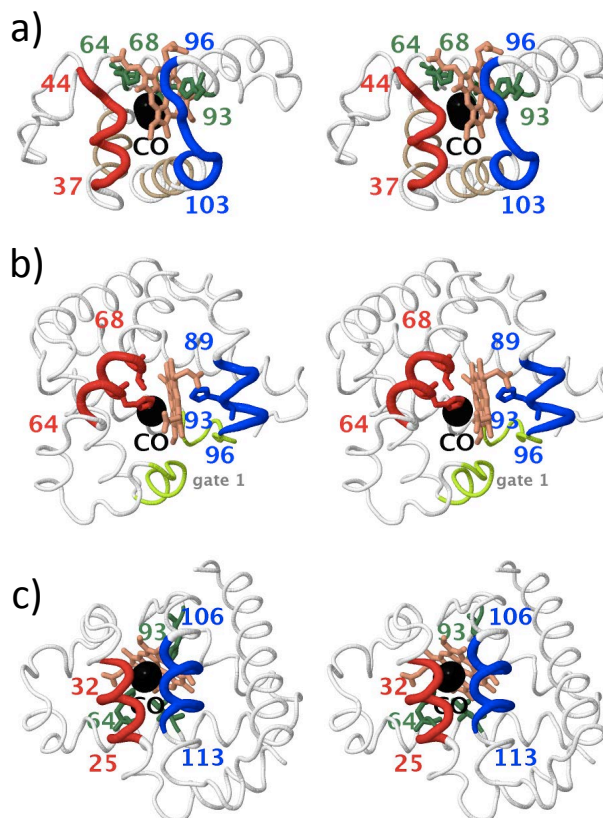


**Fig. 5.9** Stereographic cross-eyed view of the ligand Gate 1, 2 and 3 as defined in the text. Figure a) is Gate 1 formed by segment located between 37 (Pro) and 44 (Asp), and segment that starts at 96 (Lys) and ends at 103 (Tyr). Figure b) is Gate 2, between segment that starts from PDB site 61 (Leu) and ends at PDB site 68 (Val), and segment that starts at 89 (Leu) and ends at 96 (Lys). Figure c) is Gate 3, between segment starting from site 25 (Gly) and ending at 32 (Leu), and segment that starts at 106 (Phe) and ends at 113 (His). We also show the location of the heme (orange), the proximal histidine (93), the valine (68), the distal histidine (64) (all green) and the CO (black ellipsoid) of 1ABS.

thermal fluctuations in the segment distances tend to increase, the further away the segment is located from the connecting loop: The opening and closing of the gate resembles the opening and closing of scissors, with blades formed by helices E and F that are connected by the loop between these two helices. Note that the first segment along helix E, includes both the distal histidine at site 64 and the valine at the end site 68. This valine is also inside the heme pocket, and it is presumed to have an important role in CO vs. O<sub>2</sub> discrimination. Similarly, the opposite segment in the helical structure F includes the proximal histidine at site 93.

Finally, the Gate 3 which is shown in 5.9 c) is located between the helical structures



B and G. Again, in order to compare this relatively long gate with Gate 1 we select two opposing segments, each with eight amino acids. The segment in the helical structure B starts at site 25 (Gly) and ends at site 32 (Leu). The segment in helix G starts at site 106 (Phe) and ends at site 113 (His).

During the heating and cooling cycle of the myoglobin, we follow the size of the three gates. We do this by computing the distance  $d_i$  ( $i = 1, 2, 3$ ) between the respective segments, as a functions of temperature. We define the distance  $d_i$  between the two segments for each of the three gates, as follows:

$$d_i = \sqrt{\sum_{n=1}^8 (\mathbf{x}_n - \mathbf{y}_n)^2} \quad (5.6)$$

Here  $\mathbf{x}_n$  are the eight coordinates in the first segment, and  $\mathbf{y}_n$  are the corresponding coordinates in the second segment, along Gate  $i = 1, 2, 3$ . Note that the two segments in each of the three gates, are spatially oriented in an anti-parallel manner with respect to PDB indexing. Consequently, in computing (5.6), we invert the indexing in one of the two segments with respect to the PDB indexing.

We start by investigating the temperature dependence of the three gates, using the experimental data which is available in PDB. For this we compute the following three gate ratios, from PDB data:

$$\frac{\text{Gate1}}{\text{Gate2}} = \frac{d_1}{d_2} \quad \& \quad \frac{\text{Gate3}}{\text{Gate2}} = \frac{d_3}{d_2} \quad \& \quad \frac{\text{Gate3}}{\text{Gate1}} = \frac{d_3}{d_1} \quad (5.7)$$

We use all the presently available myoglobin structures in PDB, that have been measured with resolution 2.0 Å or better. The results are shown Figures 5.10. In each Figure, we observe substantial fluctuations in the gate ratios, in case of PDB data that has been taken at around 100K. But this reflects only the fact that the majority of PDB data has been collected at this temperature value. Overall, we conclude that the gate ratios show no temperature dependence for  $T < 300K$ .

We proceed to the computation of the temperature dependence of the gate ratios using our 1ABS multi-soliton with the energy function (4.17). The results are shown in Figure 5.11 a), b) and c). We have found that the Gate 3 is the first gate to open as the temperature increases, and the last one to close as temperature decreases. The Gate 2 is the one to open last, and the one to close first. In the low temperature limit the Gate 3 is about half the size of the Gate 2. But its size exceeds that of the Gate 2 in the segment separation distance (5.6) at temperature

$$k\mathcal{T}_{23}^c \approx 10^{-14} \sim 340 K$$

The transition is very rapid, in line with the general results of reference [92]: When the temperature reaches the  $\theta$ -transition value  $\sim 348 K$ , the Gate 3 is about twice as large as the Gate 2.

The Gate 1 also opens much faster than Gate 2, but slower than Gate 3. It also closes slower than Gate 2, but faster than Gate 3. In the low temperature limit the

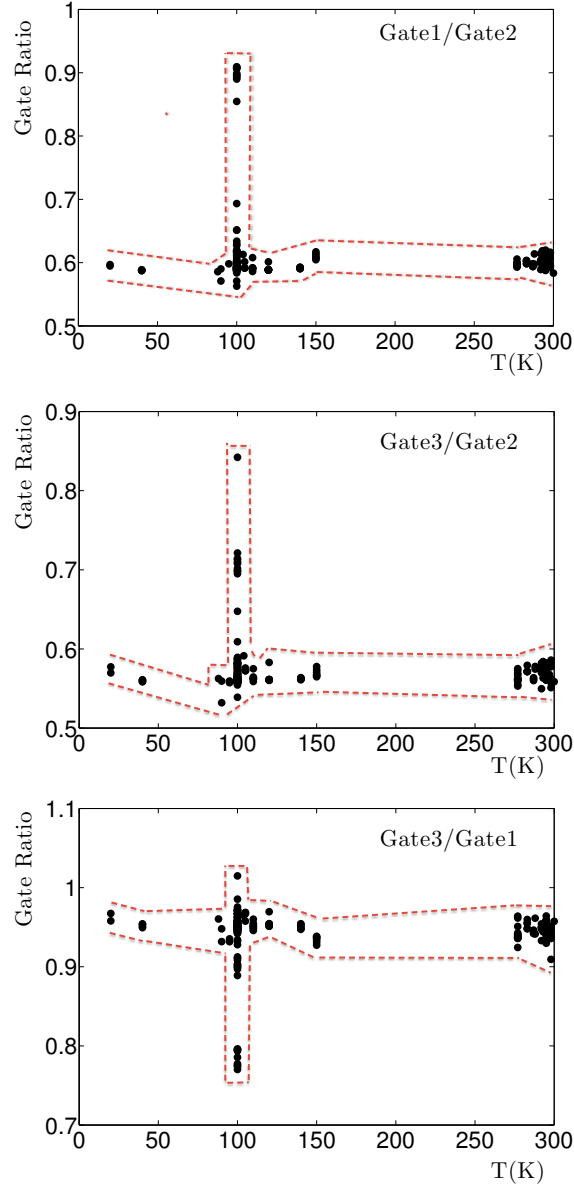


**Fig. 5.10** The three Gate ratio (5.7). The dotted (red) lines are intended to guide eye only.

Gate 1 is about half as wide as Gate 2. But it becomes wider than Gate 2 when the temperature reaches a value

$$kT_{12}^c \approx 10^{-14}$$

However, the Gate 1 does not become quite as wide as Gate 3. This is shown in Figure 5.11 a).

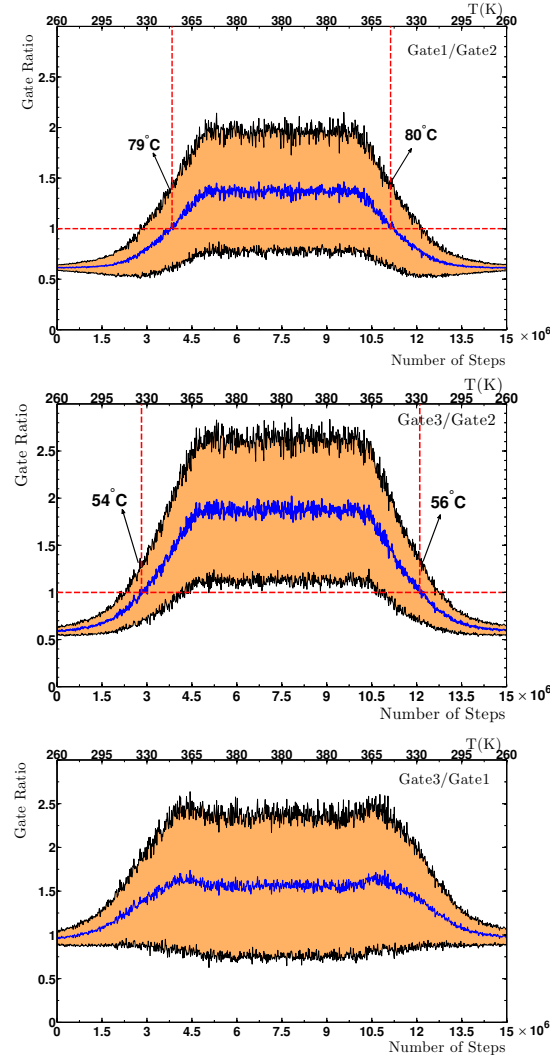


**Fig. 5.11** The temperature dependence of the three Gate ratios (5.7) during our heating and cooling cycles.

We are now in a position to determine the second parameter in (4.32) to arrive at (5.2); we remind that one of the two parameters is already determined, in (5.4). For this we proceed as follows: When we compare Figures 5.10 we conclude that experimentally, the gate ratios do not display any observable temperature dependence whenever  $T < 300\text{ K}$ . Consequently, the lowest possible value of the temperature factor

$kT$  where Figures 5.11 can display any change in the gate ratios, should correspond to a temperature which is above 300 K. When we read off the lowest possible  $kT$  value where we have an observable effect in Figures 5.11, we conclude that, necessarily,

$$kT \approx 10^{-15} > k_B 300 K$$

This gives a lower bound. When we adopt this lower bound value as our estimate for the gate opening temperature we obtain the second parameter value in (5.2).

In reality the actual gate opening temperature can be higher, but at the moment experimental basis for choosing a higher value is lacking: The single presently existing NMR data of myoglobin in PDB is 1MYF. It has been measured at the slightly higher temperature value of 308 K. But the quality of data does not enable us to improve our estimate.

We note that a higher gate opening temperature has no qualitative effect to our conclusions, quantitatively the differences are minor. The only effect would be a sharpening of the  $\theta$ -transition onset.

We conclude with a summary of the consequences that results in Figures 5.11 might have to ligand migration: We have found that to the extent backbone thermal fluctuations play a rôle in ligand migration, the Gate 3 between the helical structures B and G can be very important. This gate opens very much like a baseball glove, as we increase temperature. The Gate 1 might also play a rôle, but probably a lesser one than Gate 3. On the other hand, the V-shaped Gate 2 between helices E and F seems to be quite sturdy, it does not seem to open as much as the other two gates. The presence of the distal and proximal histidines in Gate 2 and their attractive interactions with heme, might have an additional stabilising effect that is not accounted by our model. Consequently we do not see how the thermal backbone fluctuations that take place in the Gate 2, could play a major rôle in ligand migration. At least, to the extent that backbone fluctuations are relevant.

A recent THz time-scale spectroscopy experiment has detected collective thermal fluctuations in the protein, that might relate to our theoretical proposals of ligand gate dynamics [93]. However, more detailed experiments need to be performed.

## 6

# Intrinsically disordered proteins

---

The crystallographic protein structures in PDB are *ordered* proteins. An ordered protein has an essentially unique native fold which can be determined by x-ray crystallography. But most proteins are not ordered, most proteins do not seem to have an essentially unique native fold. Instead, the low energy landscape of most proteins seems to comprise several states which are energetically degenerate but conformationally disparate. With local energy minima that are separated from each other by very low free energy barriers. We call them *intrinsically disordered* proteins. Normally these proteins can not be crystallised, and structural data is in short supply. Our aim is to extend the methods that we have developed, to describe the properties of such proteins. For this we start by describing some formalism.

But please keep in mind that there is a grey zone between ordered and intrinsically disordered proteins: A skilfull crystallographer might be able to produce a crystal out of a protein that others consider hopeless.

### 6.1 Order vs. disorder

When an ordered protein becomes cooled down to low temperatures it should assume an essentially unique native fold, that corresponds to a minimum of the low temperature thermodynamic (Helmholtz) free energy. More specifically, in the case of a protein with an ordered native fold, a cooling should produce a highly localized statistical distribution of structurally closely related conformational substates. When taken together, this ensemble constitutes the folded native state at low temperatures. But if a protein is intrinsically disordered, instead we expect that the low temperature limit produces a *scattered* statistical distribution of structurally disparate but energetically comparable ensembles of conformational substates. Moreover, these different substates should be separated from each other only by relatively low energy barriers. The unstructured, disordered character of the protein is a consequence of a motion around this scattered landscape: The protein swings and sways back and forth, quite freely, over the low energy barriers that separate the various energetically degenerate but structurally disparate conformations.

We may think that the state space of a ordered protein with an essentially unique native fold, consists of a set of *snapshot* states  $|\mathfrak{s}\rangle$  that form a *tightly* localized and essentially Gaussian distribution around an average state  $|\mathfrak{s}\rangle_{ave}$ . When taken together, the set of these snapshots determine the low temperature folded native state as an ensemble of conformational substates. In fact, we expect that for an ordered

protein, the extend of conformational variations around the average state  $|\mathfrak{s} >_{ave}$  can be estimated from the crystallographic Debye-Waller B-factor.

However, in the case of an intrinsically disordered protein the low temperature set of snapshot states  $|\mathfrak{s} >$  exhibits a *disperse* statistical distribution. We have no single tightly localised peak, with a clearly identifiable average value, in the statistical distribution of snapshots. Instead, the statistical distribution of the snapshot states is *scattered*. The snapshots become apportioned between several structurally disperse but energetically degenerate conformational substates.

Of particular interest are those energetically degenerate substates that are separated from each other by relatively low energy barriers. The unstructured and unsettled character of an intrinsically disordered protein is a consequence of thermally induced fluctuations that move the configuration around the structurally diverse and energetically degenerate landscape: The protein swings and sways back and forth between the disparate snapshot states  $|\mathfrak{s} >$ . Due to very low energy barriers, this dynamics persists even at very low temperatures, where quantum mechanical tunneling transitions eventually take over the thermally induced ones. Thus the unstructured character can persist even at very low temperatures.

We interpret the ensemble of snapshot states in terms of a Hartree state  $|\Phi >$  which is a linear combination of the form

$$|\Phi > \simeq \sum_i p_i |\mathfrak{s}_i > \quad (6.1)$$

Here the index set  $i$  can have both discrete and continuum portions, including various small and large amplitude collective coordinates. We envision that the state space which is spanned by  $|\mathfrak{s}_i >$  can be endowed with a norm (metric) which enables us to select and orthonormalize the set of *eigen-conformations* (snapshot structures)  $|\mathfrak{s}_i >$ . The detailed construction of a norm in the space of string-like structures will not be addressed here.

When  $|\mathfrak{s}_i >$  are normalised, the coefficient  $p_i$  determines the probability weight for the ensuing eigen-conformation  $|\mathfrak{s}_i >$  to contribute in the Hartree state. In particular, the Hartree state (6.1) is a *mixed* state and not a pure state, when it describes an intrinsically disordered protein; the conformational entropy is non-vanishing,

$$S = - \sum_i p_i \log p_i > 0$$

Note that when we have one single value  $p_k \approx 1$ , and the other  $p_i$  with  $i \neq k$  are vanishingly small  $p_i \approx 0$ , the Hartree state  $|\Phi >$  reduces to a pure state and describes an ordered native fold.

The eigen-conformations  $|\mathfrak{s}_i >$  are time independent, akin states in the quantum mechanical Heisenberg picture. But the  $p_i$  can be time dependent quantities, they then describe the time evolution of  $|\Phi >$ . For sufficiently long time scales, larger than the characteristic thermal tunneling time between different eigen-conformations  $|\mathfrak{s}_i >$ , the time dependence of the  $p_i$  is governed by a Liouville equation

$$\frac{d\hat{\rho}}{dt} = \frac{\partial \hat{\rho}}{\partial t} + \{\hat{\rho}, H\} \equiv \mathcal{L} \hat{\rho} \quad (6.2)$$

where

$$\hat{\rho} = \sum_i p_i |\mathfrak{s}_i\rangle\langle\mathfrak{s}_i|$$

is the density matrix. The second term in (6.2) is the Poisson bracket with the (total) semiclassical Hamiltonian  $H$ ; in a quantum mechanical version the density matrix and the Hamiltonian are replaced by the corresponding Heisenberg operators. We note that for a non-equilibrium system, the total operator  $\mathcal{L}$  becomes the (semiclassical) Lindblad superoperator.

For a system at or very near a thermodynamical equilibrium, the  $|\mathfrak{s}_i\rangle$  concur with the extrema configurations of the low temperature limit of Helmholtz free energy. The probabilities  $p_i$  are evaluated from corresponding values of the free energy, and (6.1) acquires the form

$$|\Phi\rangle \simeq \frac{1}{Z} \sum_{\{\mathfrak{s}\}} e^{-\beta E(\mathfrak{s})} |\mathfrak{s}\rangle \quad (6.3)$$

where

$$Z = \sum_{\{\mathfrak{s}\}} e^{-\beta E(\mathfrak{s})}$$

and  $\beta = 1/kT$  is the inverse temperature. For completeness, we note that for an extremum conformation  $|\mathfrak{s}_i\rangle$  that is not a local minimum of the free energy, a Maslov index contribution needs to be included.

## 6.2 hIAPP and type-II diabetes

We now proceed to consider an example of an intrinsically disordered protein with very extensive and important biological, medical and pharmaceutical ramifications.

The human islet amyloid polypeptide (hIAPP), also known as amylin, is a widely studied 37 amino acid polypeptide hormone; for extensive reviews we refer to [94,95]. It is processed in pancreatic  $\beta$ -cells from an 89 residue precursor protein, by a protease cleavage in combination of post-translational modifications. The secretion of hIAPP responses to meals, and the peptide co-operates with insulin to regulate blood glucose levels. But hIAPP can also form pancreatic amyloid deposits, and their formation and buildup correlates strongly with the depletion of islet  $\beta$ -cells. The hIAPP amyloidosis is present in over 90 per cent of the type-II diabetes patients, and the deposits are considered as the hallmark of the disease in progression.

It still remains to be fully clarified whether the hIAPP amyloid aggregation is the direct cause of apoptosis in the islet  $\beta$ -cells. Instead, the amyloid fibers might only be a consequence of the disease which is ultimately caused by some other and yet-to-be-identified agent. Among the arguments that support the existence of a first-hand causal relationship between hIAPP fibrillation and the onset of type-II diabetes, is the observation that wild-type mice do not develop the disease while transgenic mice that express hIAPP can fall ill with the disease. It has also been observed that a direct contact between the hIAPP amyloid fibrils and the surfaces of pancreatic islet  $\beta$ -cells has a toxic effect on the latter.

There is a real possibility that by understanding the structural landscape of hIAPP, in particular how the amyloidosis transition takes place, we could gain a major step towards the identification of therapeutic targets and the development of strategies to combat a potentially deadly disease, that presently plagues around 5 per cent of the world's adult population. Indeed, type-II diabetes is arguably among the most devastating diseases to curse mankind. Its annual economic cost has been globally estimated to be in excess of 425 billion Euro's, and the number of sufferers is estimated to almost double during the next 20 years.

The structure of aggregated hIAPP fibrils have been studied very extensively [94, 95]. The fibrils consist of an ordered parallel arrangement of monomers, with a zipper-like packing. Apparently the fibril formation proceeds by nucleation, with one monomeric hIAPP molecule first assuming a hairpin-like structure. This is followed by a piling-up of several monomers, which eventually leads to the buildup of amyloid fibrils as the hallmark of the disease in progression. But the structure of a full-length monomeric hIAPP, its potentially disease causing dynamical conformational state in our pancreatic cells, and why it occasionally may form the disease causing hairpin-like structure, all these remain unknown. Moreover, despite the highly ordered nature of amyloid fibril aggregates, only very recently have experimental advances made it possible to obtain high-resolution models. However, we still largely lack detailed atomic level knowledge, needed for drug development.

The monomeric form of hIAPP is presumed to be an example of an intrinsically disordered protein. When biologically active and healthy, it is in an unsettled and highly dynamic state. As such it lacks an ordered three dimensional folded state that could be studied by conventional x-ray crystallography approaches. Several experimental methods which are based e.g. on solution and solid-state NMR and other techniques, are currently under development to try and characterise the conformation of monomeric hIAPP. But the existing techniques do not yet permit a direct examination of the atomic level structure. Detergents such as Sodium dodecyl sulfate (SDS) micelles are commonly introduced as stabilising agents.

The detailed atomic level information could in principle be extracted by theoretical means with molecular dynamics simulations. However, with explicit water presently available computer power can at best cover a dynamical *in vitro*/*in vivo* trajectory up to around a microsecond per a day *in silico*. At the same time amyloid aggregation takes hours, even days. Thus the present all-atom computational investigations are largely dependent on our ability to determine an initial conformation for the simulations. Otherwise, one might only end up simulating the initial condition.

Due to its intrinsically disordered character, the structural data of hIAPP in isolation remains sparse in PDB. The only presently available PDB data of hIAPP consists of two NMR structures and one crystallographic structure. Both NMR structures describe hIAPP in a complex with SDS micelles, the PDB access codes are 2L86 and 2KB8. The sole available crystallographic structure describes hIAPP that has been fused with a maltose-binding protein, the PDB access code is 3G7V. We note that these three structures are all very different from each other.

The NMR structure 2L86 has been measured at pH of 7.4 *i.e.* around the pH value in the extracellular domain where the hIAPP amyloid deposits appear. On the other



hand, the NMR structure 2KB8 has been measured with pH value 4.6 which is closer to the pH value around 5.5 inside the  $\beta$ -cell granules of pancreas. We point out that even though hIAPP amyloidosis is apparently an extracellular process, some evidence suggests that the aggregation might have an intracellular origin. Thus, a thorough investigation of the rôle of hIAPP in the onset of type-II diabetes, should account *both* for the extracellular and the intracellular structural properties of the peptide. In addition, a detailed analysis how hIAPP interacts with cell membranes is needed; we note that to some extent, micelles might mimic membrane effects.

We conclude, that it has been pointed out, that hIAPP affects also several other organs besides pancreas. For example, hIAPP is known to have binding sites in the brain, where it apparently has a regulatory effect on gastric emptying. A delayed gastric emptying is commonly diagnosed in patients with diabetes. But gastroparesis is also a component in a number of other disorders. Certainly, the ability of hIAPP to cross the blood-brain barrier and affect the central nervous system, relates to its structure. Amyloid fibers can hardly cross the barrier. Thus, besides apparently contributing directly to type-II diabetes, aggregation should also have a wider influence on the regulatory activity of hIAPP.

### 6.3 hIAPP as a three-soliton

In this Section we shall investigate in detail the physical properties of a 28 segment monomer of hIAPP; we propose that the reader gets access to the entry 2L86 in PDB. The segment we are interested in, consists of the residues 9-36 where several studies have either observed or predicted that the amyloid fibril formation starts [94,95]. The physical properties of the short N-terminal segment that comprises the residues 1-8 is not addressed here. The structure of this segment is more involved, due to the disulfide bond that connects the cysteines which are located at the residues 2 and 7. Moreover, it remains to be understood what is the rôle, if any, of the residues 1-8 in hIAPP aggregation. These residues appear to have a tendency towards forming long and stable non- $\beta$ -sheet fibers in solution, under the same conditions in which hIAPP aggregates into amyloid fibers.

We use the NMR structure 2L86 in PDB as a decoy to train the energy function. We construct a multi-soliton configuration as an extremum of the energy function (4.17), that accurately describes 2L86. Since 2L86 is a composite of hIAPP with SDS micelles, we propose the following biological set-up: We consider the structural evolution of an isolated hIAPP in the extracellular domain, in a scenario where the polypeptide is initially in a direct but residual interaction with the cell membrane. The effect of an initial cell membrane interaction is modelled by the effect of SDS micelles in 2L86. Following the construction of the multi-soliton configuration, we study the presumed disordered structural landscape of an isolated hIAPP; we try and model hIAPP as it enters the extracellular domain. For this we subject the multi-soliton to a series of heating and cooling simulations as in the case of myoglobin, using the Glauber dynamics. During the heating, we increase the temperature until we detect a structural change in the multi-soliton, so that the configuration behaves like a random walker. We fully thermalise the configuration at the random walk phase. We then reduce the ambient temperature, to cool down the configuration to very low temperature values

until it freezes into a conformation where no thermal motion prevails. Since an isolated hIAPP is intrinsically disordered, instead of a single native fold as in the case of myoglobin we expect that the low temperature limit produces a scattered statistical distribution of structurally disparate but energetically comparable ensembles of conformational substates (6.1). Moreover, the individual different substates should be separated from each other by relatively low energy barriers. The unstructured, disordered character of hIAPP is then a consequence of a motion around this landscape: It swings and sways back and forth, quite freely, over the low energy barriers that separate the various energetically degenerate but structurally disparate conformations. We shall find that in the case of hIAPP, the heating and cooling procedure which in the case of myoglobin yields a single low energy state, now produces exactly this kind of structurally scattered ensembles of conformations.

In Table 6.3 we have the parameter values, that we find by training the energy function (4.17) to describe 2L86. These parameters values are taken from [96].

**Table 6.1** Parameter values for the three-soliton configuration that describes 2L86; the soliton 1 cover the PDB segment THR 9 – ASN 21, the soliton 2 covers the segment ASN 22 – ALA 25 and the third soliton covers the segment ILE 26 – THR 36. The value of  $a$  is fixed to  $a = -10^{-7}$ .

soliton	$q_1$	$q_2$	$m_1$	$m_2$	$d/a$	$c/a$	$b/a$
1	9.454	4.453	1.521	1.606	$-8.164 \cdot 10^{-2}$	$-1.402 \cdot 10^{-3}$	-2.568
2	2.927	2.441	1.667	1.534	$-4.894 \cdot 10^{-1}$	$-1.067 \cdot 10^{-3}$	-19.48
3	1.119	8.086	1.522	1.514	$-3.578 \cdot 10^{-2}$	$-5.907 \cdot 10^{-3}$	- 1.908

In Figure 6.1 a) we show the spectrum of bond and torsion angles for the first NMR structure of 2L86, with the convention that the bond angle takes values between  $\kappa \in [0, \pi]$ . In Figure 6.1 b) we have introduced the  $\mathbb{Z}_2$  symmetry (4.11) to disclose three individual solitons along the backbone. The first soliton from the N-terminal is centered at the site 17. The third soliton is centered at the site 27. Both of these two solitons correspond to clearly visible loops in the three dimensional structure, in the PDB entry 2L86 (see PDB). The second soliton, centered at site 23, is much less palpable in the three dimensional NMR structure. This soliton appears more like a bend in an  $\alpha$ -helical structure, extending from the first soliton to the third soliton. The  $\mathbb{Z}_2$  transformed  $(\kappa, \tau)$  profile shown in Figure 6.1 b) is the background that we have used in training the energy function (4.17).

In Figure 6.2 we compare the bond and torsion angle spectrum of our three-soliton solution with the first NMR structure of 2L86; the solution is obtained using the program *ProPro* in (5.1). The quality of our three-soliton solution is clearly very good, at the level of the bond and torsion angles.

Figure 6.3 shows our three-soliton solution, interlaced with the first NMR structure of 2L86. The RMSD distance between the experimental structure and the three-soliton configuration is 1.17 Å. This is somewhat large, when compared to the multi-

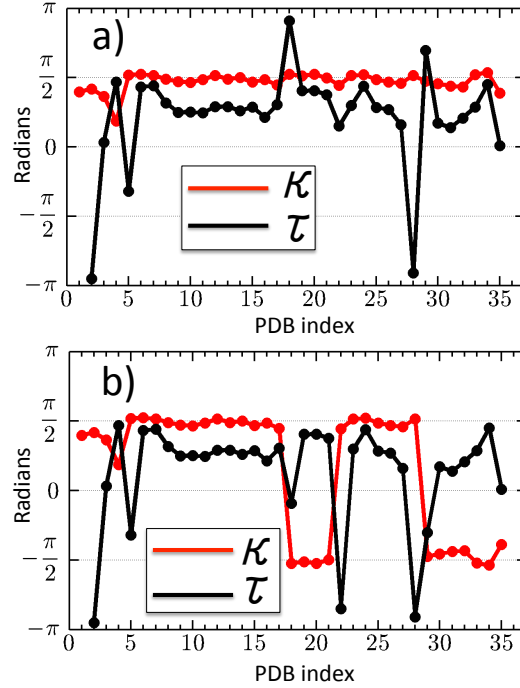


**Fig. 6.1** a) The spectrum of the bond and torsion angles of 2L86 (first entry) with the convention that bond angle takes values in  $\kappa \in [0, \pi)$ . b) The spectrum of the bond and torsion angles that identifies the soliton structures.

soliton structures that we have found previously. But the resolution of the present experimental NMR structure is not that good, and this is reflected by the somewhat lower quality of the three-soliton solution, in comparison to the case of high resolution crystallographic structures.

Figure 6.4 compares the residue-wise  $C\alpha$  distances, between the 20 different NMR structures in the PDB entry 2L86, and our three-soliton solution. For those residues that precede the bend-like second soliton which is centred at site 23, the distance between the experimental structures and the numerically constructed solution is relatively small. We observe a quantitative change in the precision of the three-soliton solution, that takes place after site 23. The distance between the experimental structures and the three-soliton solution clearly increases after this residue. It could be that this change is due to the SDS micelles, used in the experimental set-up to stabilise hIAPP/2L86: SDS is widely used as a detergent, to enable NMR structure determination in the case of proteins with high hydrophobicity. The mechanism of SDS-protein interaction is apparently not yet fully understood. But it is known that the hydrophobic tails of SDS molecules interact in particular with the hydrophobic core of a protein. These interactions are known to disrupt the native structure to the effect, that the protein displays an increase in its  $\alpha$ -helical posture; these additional  $\alpha$ -helical structures

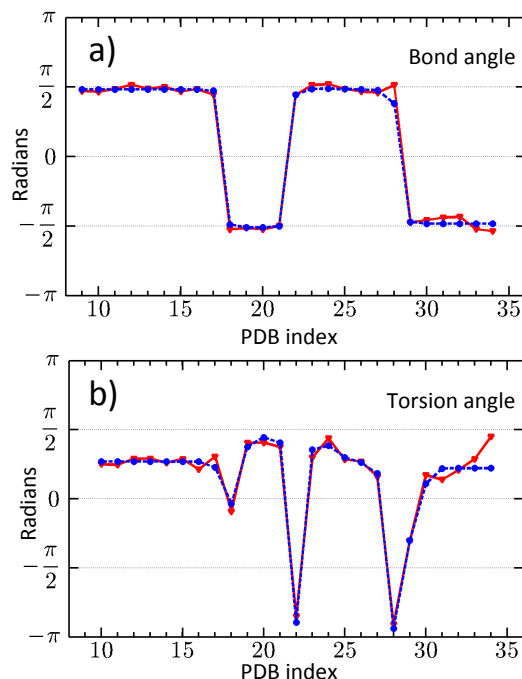


**Fig. 6.2** Top: Comparison of the three-soliton bond angle (blue) with the experimental 2L86 bond angle spectrum (red). Bottom: Comparison of the three-soliton torsion angle (blue) with the experimental 2L86 torsion angle spectrum (red).

tend to be surrounded by SDS micelles.

The residue site 23 of hIAPP is the highly hydrophobic phenylalanine. It is followed by the very flexible glycine at site 24. Thus, the apparently abnormal bend which is located at the site 23 and affects the quality of our three-soliton configuration, could be due to an interaction between the phenylalanine and the surrounding SDS micelles. A high sensitivity of the hIAPP conformation to the phenylalanine at site 23 is well documented.

An analysis of 2L86 structure using *Molprobit* (1.3) suggests a propensity towards poor rotamers between the sites 23-36, *i.e.* the region where the quality of our three-soliton solution decreases.

A comparison with the statistically determined radius of gyration relation (1.10) reveals that for 2L86 the value of  $R_g \approx 9.2$  (over residues  $N = 9, \dots, 36$ ). This is somewhat high. According to (1.10), we expect a value close to  $R_g \approx 7.9$  when we set  $N = 28$ . The structure of 2L86 should be more compact.

We conclude that most likely the SDS-hIAPP interaction has deformed a loop which, in the absence of micelles, should be located in the vicinity of the residue number 23. Probably, the interaction with micelles has converted this loop into a structure resembling a bend in an  $\alpha$ -helix. This interaction between hIAPP and SDS interferes with our construction of the three-soliton configuration, adversely affecting

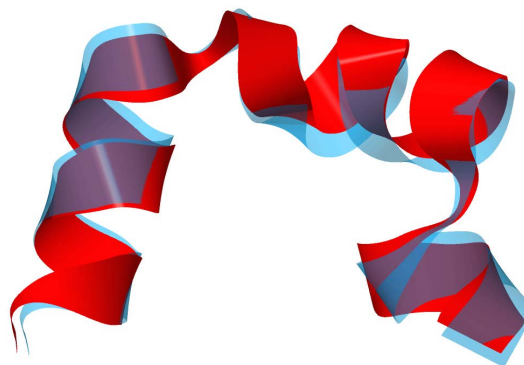


**Fig. 6.3** The three-soliton solution (blue) interlaced with the 2L86 experimental structure (red).

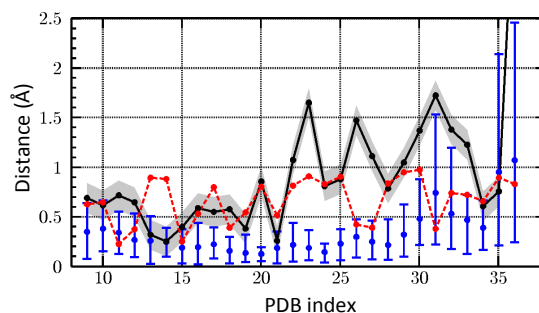


**Fig. 6.4** The black line denotes the  $C\alpha$  atom distance between the 3-soliton configuration and the model 1 NMR configuration 2L86; the grey region is an estimated  $0.15 \text{ \AA}$  zero-point fluctuation distance from the three-soliton configuration. The red line denotes the B-factor Debye-Waller fluctuation distance from model 1 of 2L86. The blue-colored points denote the average  $C\alpha$  distance between the model 1 NMR structure from the average of the remaining 19 models on 2L86; the error-bars denote the maximal and minimal  $C\alpha$  distances.

its precision.

## 6.4 Heating and cooling hIAPP

Following our myoglobin analysis, we proceed to investigate the properties of the three-soliton model of 2L86 under repeated heating and cooling, using the Glauber algorithm.

The Figures 6.5 describe the evolution of the three-soliton configuration during repeated heating and cooling. The Figure 6.5 (top) shows the evolution of the radius of gyration, and the Figure 6.5 (bottom) shows the RMSD distance to the PDB structure 2L86. Both the average value and the one standard deviation from the average value are shown. During the cooling period we observe only one transition, in both the radius of gyration and the RMSD. Thus, based on our previous experience, we are confident

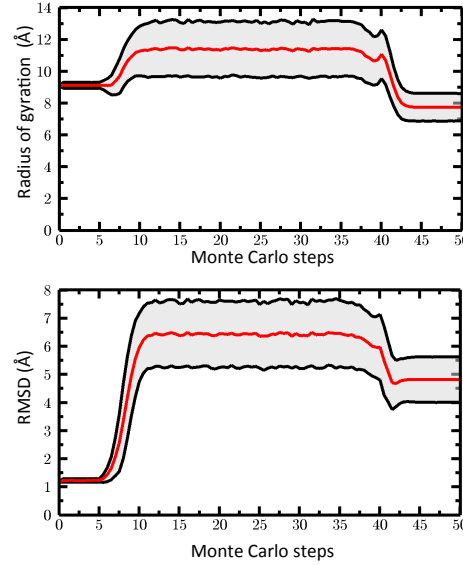


**Fig. 6.5** The top figure shows how the radius of gyration of the three-soliton configuration evolves during heating and cooling cycle. The bottom figure shows the same for the RMSD distance from the initial configuration. The red line is the average value over all configurations, and the grey zone marks the extent of one standard deviation from the average value. The Monte Carlo steps are displayed in multiples of  $10^6$ .

that at high temperatures we are in the random walk regime. The profile of each curve in Figure 6.5 also shows that the structures are fully thermalised, both in the high temperature and in the low temperature regimes.

We observe that the average final value of the radius of gyration  $R_g \approx 7.8$  is an excellent match with the prediction obtained from (1.10). In particular, the final configurations are quite different from the initial one: The RMSD distance between the initial configuration and the average final configuration is around  $4.8 \text{ \AA}$ .

Figure 6.6 shows results for a representative simulation with 1.500 complete heating and cooling cycles; an increase in the number of cycles does not have a qualitative effect on the result. The Figure shows the distribution of the final snapshot conformations, grouped according to their radius of gyration versus end-to-end distance. The final conformations form clusters, and we identify the six major clusters that we observe in our simulations. By construction, the clusters correspond to local extrema of the energy function we have constructed to model 2L86: The average conformation of each cluster can be identified with a particular snapshot state  $|\mathbf{s}\rangle$  in the expansion (6.1), (6.3). Five of the clusters, denoted 2-6 in the Figure, have an apparent spread. This implies that the energy has a flat conformational direction around its extremum. The clusters 3 and 5 are also somewhat more scattered than the clusters 2, 4 and 6. Finally, the cluster number 1 is a localized one: This cluster corresponds to a sharply localized snapshot state  $|\mathbf{s}\rangle$ . Note that the initial conformation, marked with red triangle in

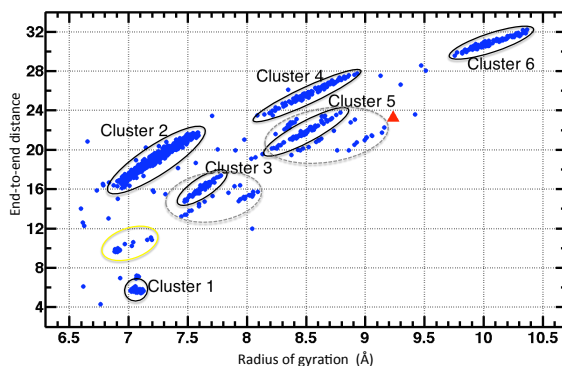


**Fig. 6.6** The distribution of all final configurations, in a run with 1.500 full heating and cooling cycles, classified in terms of the radius of gyration and end-to-end distance of the final configuration. Each blue dot represents a single final configuration. The six major clusters are encircled with a black ellipse; a wider grey ellipse around the clusters 3 and 5 includes some nearby scattered states. The red triangle identifies the initial configuration, the entry 1 in 2L86. Note also the presence of a cluster encircled with yellow between clusters 1 and 2.

the Figure 6.6, does not appear among the final configurations. It is apparently an unstable extremum of the energy, stabilised by the micelles.

In Figure 6.7 we display the average conformations in each of the six clusters, interlaced with each other and the initial 2L86 configuration. In this Figure, the first two  $C\alpha$  atoms from the N-terminus are made to coincide. We have maximised the alignment of the subsequent  $C\alpha$  atoms, to the extent it is possible. The Figure reveals the presence of substantial conformational difference between the clusters. The totality of the conformations shown in Figure 6.7 can be given an interpretation in terms of the dynamical hIAPP. It is a long time period average picture of the Hartree state (6.1), (6.3) that is a linear combination of the various snapshot conformations  $|\mathfrak{s}_i\rangle$  ( $i = 1, \dots, 6$ ).

In Figures 6.8 we compare the individual clusters with the initial 2L86 configuration (in blue). In each of these Figures, we show ten representative entries in each of the clusters (in red), to visualise the extent of conformational fluctuations within each cluster. We observe that the conformational spread within each of the six clusters is not very large.

In conclusion, we have found that the three-soliton configuration which models the  $C\alpha$  backbone of the human islet amyloid polypeptide, is quite unsettled: Its low temperature limit comes endowed with six different conformational clusters. This is a marked contrast with the properties of a multi-soliton configuration which models a protein that is known to possess a unique folded native state, such as myoglobin. The low temperature clustering of hIAPP is in full accord with the intrinsically disordered

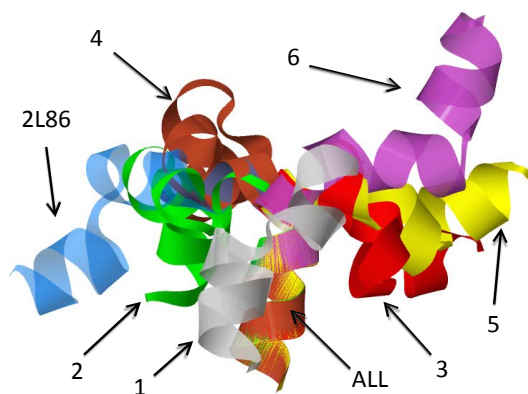


**Fig. 6.7** Superposition of all the six major clusters in Figure 6.6, interlaced with each other and with the PDB entry 2L86.

character of the protein: The different clusters can be viewed as instantaneous snapshot conformations, between which the dynamic hIAPP swings and sways in an apparently unsettled manner which is characteristic to an intrinsically disordered protein.

Only the cluster number one appears different. This cluster has a much more localised conformational distribution than the other five clusters, and the posture comprises of two anti-parallel helices. This proposes to us, that the cluster number one is a good candidate to trigger the formation of hIAPP fibrils and amyloidosis which correlates with diabetes-II.

*My advice to all my students is, be careful with your life-style to keep your hIAPP folds under good control.*



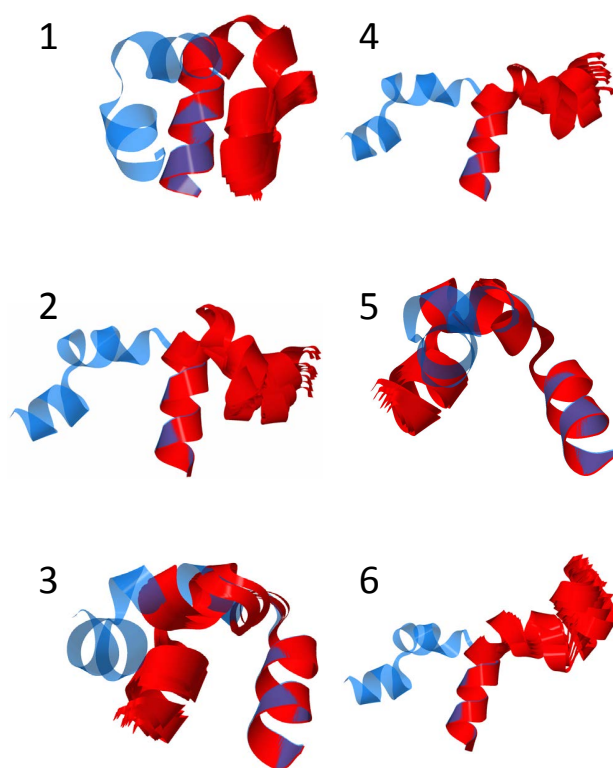


**Fig. 6.8** Superposition of ten representative conformations (red) in each of the six clusters, as marked, together with the PDB entry 2L86 (blue).

## 7 Beyond $C_\alpha$

---

Thus far we have analysed the protein structure and dynamics in terms of the  $C_\alpha$  atoms only, we have argued that the virtual  $C_\alpha$  backbone bond and torsion angles form a complete set of local order parameters to describe the protein backbone conformation.

The  $C_\alpha$  atoms are in a central rôle in x-ray crystallography, where the experimental determination of protein structure often starts with a skeletonisation of the electron density map: From Figures 1.1, 1.7 we observe that the  $C_\alpha$  atoms are located centrally. They form the vertices that connect the peptide planes. They coincide with the branch points between the backbone and the side chain. Thus the  $C_\alpha$  atoms are subject to stringent stereochemical constraints. Accordingly, the first step in experimental model building is the initial identification of the skeletal  $C_\alpha$  trace.

The central rôle of the  $C_\alpha$  atoms is widely exploited in structural classification schemes like CATH and SCOP [84, 85], in various homology modeling techniques [27–29] in *de novo* approaches [3], and in the development of coarse grained energy functions for folding prediction [47, 48]. The so-called  $C_\alpha$ -trace problem has been formalised, and it is the subject of extensive investigations [97–99]. The aim is to construct an accurate main chain and/or all-atom model of the folded protein from the knowledge of the positions of the central  $C_\alpha$  atoms only. Both knowledge-based approaches such as *Maxsprout* [100] and *de novo* methods like *Pulchra* [101] have been developed for this purpose. In the case of the backbone atoms, various geometric algorithms can be utilised. For the side chain atoms, most approaches rely either on a statistical or on a conformer rotamer library in combination with steric constraints, complemented by an analysis which is based on diverse scoring functions. For the final fine-tuning of the model, all-atom molecular dynamics simulations can be utilised.

The Ramachandran map shown in Figure 1.10 is used widely both in various analyses of the protein structures, and as a tool in protein visualisation. It describes the statistical distribution of the two dihedral angles  $\phi$  and  $\psi$  that are adjacent to the  $C_\alpha$  carbons along the protein backbone. In the case of side chain atoms, visual analysis methods similar to the Ramachandran map have been introduced. For example, there is the Janin map that can be used to compare observed side chain dihedrals in a given protein against their statistical distribution in a manner which is analogous to the Ramachandran map. Crystallographic refinement and validation programs like *Phenix* [102], *Refmac* [103] and many others, utilise the statistical data obtained from libraries such as Engh and Huber library [12], that are built using small molecular structures which have been determined with a very high resolution. At the level of entire proteins, side chain restraints are commonly derived from analysis of high resolution PDB crystallographic structures [104]. Backbone independent rotamer li-

libraries that make makes no reference to backbone conformation, and both secondary structure and backbone dependent rotamer libraries have been developed. According to [104] the information content in the secondary structure dependent libraries and the backbone independent libraries essentially coincide, and both are often used during crystallographic protein structure model building and refinement. But for the prediction of side-chain conformations for example in the case of homology modelling and protein design, it is often an advantage to use the more revealing backbone dependent rotamer libraries.

## 7.1 "What-you-see-is-what-you-have"

We shall present a short introductory outline, how the  $C\alpha$  Frenet frames can be utilised to develop new generation visualisation techniques for protein structure analysis, refinement and validation. Our outline is based on [105–107].

Despite the availability of various 3D visualisation tools such as the Java-based viewer on PDB website, thus far the visualisation of proteins has not yet taken *full* advantage of modern visualisation techniques. The commonly available 3D viewers present the protein in the 'laboratory' frame and as such they provide mainly an *external* geometry based characterisation of the protein structure. On the other hand, the method that we describe is based on internal, *co-moving* framing of the protein backbone: To watch a roller-coaster is not the same as taking the ride. As such our approach provides complementary visual information. Starting from the positions of the  $C\alpha$  atoms, we aim for a 3D *what-you-see-is-what-you-have* type visual map of the all-atom structure. Indeed, the visualization of a three dimensional discrete framed curve is an important and widely studied topic in computer graphics, from the association of ribbons and tubes to the determination of camera gaze directions along trajectories.

In lieu of the backbone dihedral angles that appear as coordinates in the Ramachandran map and correspond to a toroidal topology, we use the geometry of virtual two-spheres that surround each heavy atom. For this we employ the geometric interpretation of the virtual  $C\alpha$  backbone bond and torsion angles in terms of latitude and longitude on the surface of a sphere  $S^2$ . We shall outline how the approach works in the case of the backbone N and C atoms, and the side chain  $C\beta$  atoms. The approach can be easily extended to visually describe all the higher level side chain atoms on the surface of the sphere, level-by-level along the backbone and side chains [105–107]. The outcome is a 3D visual map that describes the backbone and side-chain atoms exactly in the manner how they are seen by an imaginary, geometrically determined and  $C\alpha$  based miniature observer who roller-coasts along the backbone: At each  $C\alpha$  atom the observer orients herself consistently according to the purely geometrically determined  $C\alpha$  based discrete Frenet frames. Thus the visualisation of all the other atoms depends only on the  $C\alpha$  geometry, there is no reference to the other atoms in the initialisation of the construction. The other atoms - including subsequent  $C\alpha$  atoms along the backbone chain - are all mapped on the surface of a sphere that surrounds the observer, as if these atoms were stars in the sky; the construction proceeds along the ensuing side chain, until the position of all heavy atoms have been determined. This provides a

purely geometric and equitable, direct visual information on the statistically expected all-atom structure in a given protein, based entirely on the C $\alpha$  trace.

We start with the bond and torsion angles (4.4), (4.5) and we choose each bond angle to take values  $\kappa \in [0, \pi]$ . We identify the bond angle with the latitude angle of a two-sphere which is centered at the C $\alpha$  carbon. We orient the sphere so that the north-pole where  $\kappa = 0$  is in the direction of  $\mathbf{t}$ . The torsion angle  $\tau \in [-\pi, \pi)$  is the longitudinal angle of the sphere. It is defined so that  $\tau = 0$  on the great circle that passes both through the north pole and through the tip of the normal vector  $\mathbf{n}$ . The longitude angle increases towards the counterclockwise direction around the vector  $\mathbf{t}$ . We find it also useful, to introduce the stereographic projection of the sphere onto the plane. The standard stereographic projection from the south-pole of the sphere to the plane with coordinates  $(x, y)$  is given by

$$x + iy \equiv r e^{i\tau} = \tan(\kappa/2) e^{i\tau} \quad (7.1)$$

This maps the north-pole where  $\kappa = 0$  to the origin  $(x, y) = (0, 0)$ . The south-pole where  $\kappa = \pi$  is sent to infinity; see Figure 7.1. If need be, the visual effects of the

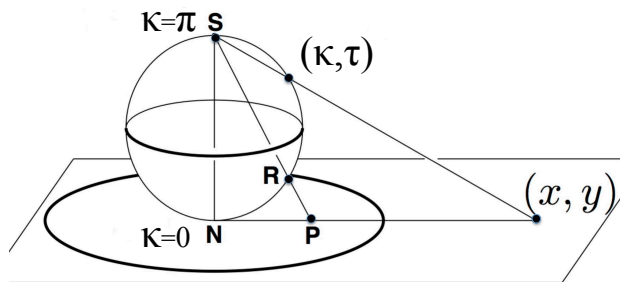


**Fig. 7.1** Stereographic projection of two-sphere  $S^2$  on the plane  $\mathbb{R}^2$ , from the south-pole.

projection can be enhanced by sending

$$\kappa \rightarrow f(\kappa)$$

where  $f(\kappa)$  is a properly chosen function of the latitude angle  $\kappa$ .

### 7.1.1 The C $\alpha$ map

We first explain how to visually describe the C $\alpha$  trace in terms of the C $\alpha$  Frenet frames (4.1)-(4.3). Consider the virtual miniature observer who roller-coasts the backbone by moving between the C $\alpha$  atoms. At the location of each C $\alpha$  the observer has an orientation that is determined by the Frenet frames (4.1)-(4.3). The base of the  $i^{th}$  tangent vector  $\mathbf{t}_i$  is at the position  $\mathbf{r}_i$ . The tip of  $\mathbf{t}_i$  is a point on the surface of the sphere  $(\kappa, \tau)$  that surrounds the observer and points towards the north-pole. The vectors  $\mathbf{n}_i$  and  $\mathbf{b}_i$  determine the orientation of the sphere. These vectors define a frame on the normal plane to the backbone trajectory, as shown in Figure 4.1. The observer maps the various atoms in the protein chain on the surface of the surrounding two-sphere, as if the atoms were stars in the sky.

The map of the  $C\alpha$  backbone is constructed as follows. The observer first translates the center of the sphere from the location of the  $i^{th}$   $C\alpha$ , all the way to the location of the  $(i+1)^{th}$   $C\alpha$  with *no rotation* of the sphere with respect to the  $i^{th}$  Frenet frames. The observer then identifies the direction of  $\mathbf{t}_{i+1}$ , i.e. the direction towards the site  $\mathbf{r}_{i+2}$  to which she proceeds from the next  $C\alpha$  carbon, as a point on the surface of the sphere. This determines the corresponding coordinates  $(\kappa_i, \tau_i)$ . After this, the observer re-defines her orientation so that it matches the Frenet framing at the  $(i+1)^{th}$  central carbon, and then proceeds by repeating the construction, exactly in the same manner. The ensuing map, over the entire backbone, gives an instruction to the observer at each point  $\mathbf{r}_i$ , how to turn at site  $\mathbf{r}_{i+1}$ , to reach the  $(i+2)^{th}$   $C\alpha$  carbon at the point  $\mathbf{r}_{i+2}$ .

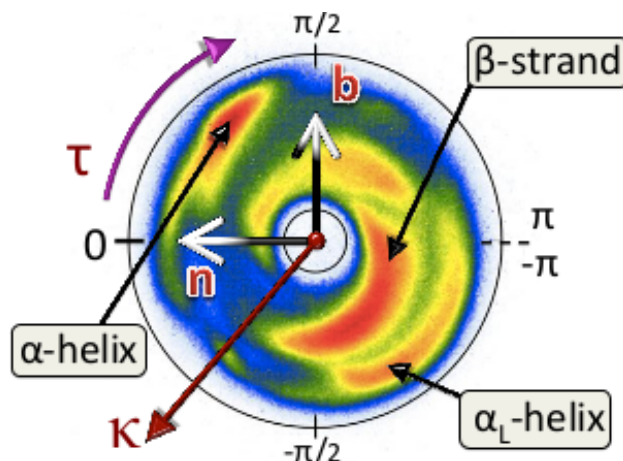


**Fig. 7.2** The stereographically projected Frenet frame map of backbone  $C\alpha$  atoms, with major secondary structures identified. Also shown is the directions of the Frenet frame normal vector  $\mathbf{n}$ ; the vector  $\mathbf{t}$  corresponds to the red circle at the center, and it points away from the viewer. The map is constructed using all PDB structures that have been measured with better than 2.0 Å resolution.

In figure 7.2 we show the  $C\alpha$  Frenet frame backbone map. It describes the statistical distribution that we obtain when we plot all PDB structures which have been measured with better than 2.0 Å resolution, and using the stereographic projection (7.1). For our observer, who always fixes her gaze position towards the north-pole of the surrounding two-sphere at each  $C\alpha$  i.e. towards the red dot at the center of the annulus, the color intensity in this map reveals the probability of the direction at position  $\mathbf{r}_i$ , where the observer will turns at the next  $C\alpha$  carbon, when she moves from  $\mathbf{r}_{i+1}$  to  $\mathbf{r}_{i+2}$ . In this way, the map is in a direct visual correspondence with the way how the Frenet frame observer perceives the backbone geometry. Note how the probability distribution concentrates within an annulus, roughly between the latitude angle values  $\kappa \sim 1$  and  $\kappa \sim 3/2$ . The exterior of the annulus is a sterically excluded region while the entire interior is in principle sterically allowed but very rarely occupied in the case of folded

proteins. In the figure we identify the four major secondary structure regions, according to the PDB classification; the  $\alpha$ -helices,  $\beta$ -strands, left-handed  $\alpha$ -helices and loops.

### 7.1.2 The backbone C, N and side chain C $\beta$ maps

Consider our imaginary miniature observer, located at the position of a C $\alpha$  atom and oriented according to the discrete Frenet frames. She proceeds to observe and record the backbone heavy atoms N, C and the side-chain C $\beta$  atoms that are covalently bonded to C $\alpha$ . These atoms form the covalently bonded heavy-atom corners of the C $\alpha$  centered  $sp^3$ -hybridised tetrahedron. In figures 7.3 a)-d) we show the ensuing density distributions on the surface of the C $\alpha$  centered sphere, the way how they are seen by the miniature observer. These figures are constructed from all the PDB entries that have been measured using diffraction data with better than 1.0 Å resolution.

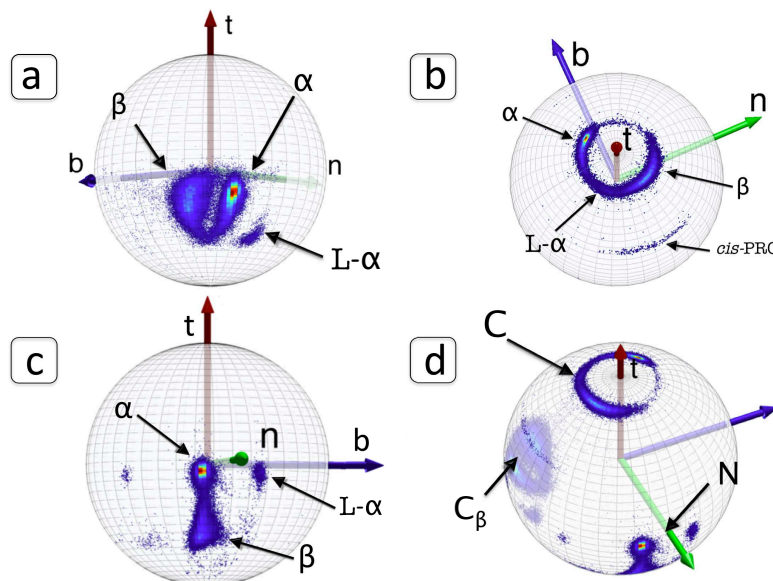


**Fig. 7.3** a) Distribution of C $\beta$  atoms in the C $\alpha$  centered Frenet frames in PDB structures measured with better than 1.0 Å resolution. The three major domains  $\alpha$ -helices,  $\beta$ -strands and left-handed  $\alpha$ -helices have been marked. b) Same as a) but for backbone C atoms. Note that *cis*-prolines are also clearly identifiable. c) Same as a) but for backbone N atoms. d) A combination of distributions in a)-c).

As visible in Figures 7.3 in the C $\alpha$  entered Frenet frames the C $\beta$ , C and N atoms each oscillate in a manner that depends on the local secondary structure. Note that both in the case of C $\beta$  and N, the left-handed  $\alpha$  region (L- $\alpha$ ) is distinctly detached from the rest. But in the case of C the L- $\alpha$  region is connected with the other regions. On the other hand, in the case of N the *cis*-prolines form a clearly detached and localized region, which is not similarly visible in the case of C and C $\beta$ .

We now consider the three bond angles

$$\begin{aligned}
 \vartheta_{\text{NC}} &\simeq \text{N} - \text{C}\alpha - \text{C} \\
 \vartheta_{\text{N}\beta} &\simeq \text{N} - \text{C}\alpha - \text{C}\beta \\
 \vartheta_{\beta\text{C}} &\simeq \text{C}\beta - \text{C}\alpha - \text{C}
 \end{aligned}
 \tag{7.2}$$

The  $\vartheta_{\text{NC}}$  angle relates to the backbone only, while the definition of the other two involves the side chain  $\text{C}\beta$ . In experimental protein structure validation these three angles are often presumed to have their ideal values. For example, the deviation of the  $\text{C}\beta$  atom from its ideal position is among the validation criteria used in *Molprobability* (1.3) that uses it in identifying potential backbone distortions around  $\text{C}\alpha$ .

In Figure 7.4 we show the distribution of the three tetrahedral bond angles in our 1.0 Å PDB data set. We find that in the case of the two side chain related angles  $\vartheta_{\text{N}\beta}$  and  $\vartheta_{\beta\text{C}}$  the distribution displays a single peak which is compatible with the ideal values; the isolated small peak in Figure 7.4 b) is due to *cis*-prolines. But in the case of the backbone specific angle  $\vartheta_{\text{NC}}$  we find that this is not the case. The PDB data shows a clear correlation between the  $\vartheta_{\text{NC}}$  distribution and the backbone secondary structure. We remind that  $\vartheta_{\text{NC}}$  pertains to the relative orientation of the two peptide planes that are connected by the  $\text{C}\alpha$ .

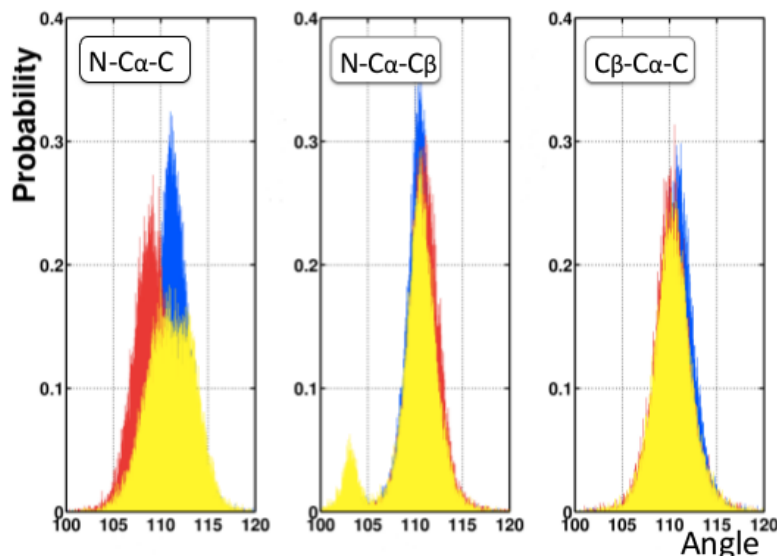


**Fig. 7.4** Distribution of the three angles (7.2) according to secondary structures. Blue are  $\alpha$ -helices, red are  $\beta$ -strands and yellow are loops; the small (yellow) peak in  $\text{N-C}\alpha\text{-C}\beta$  with angle around  $103^\circ$  is due to prolines.

The two Ramachandran angles ( $\phi, \psi$ ) in Figure 1.10 are directly adjacent to the given  $\text{C}\alpha$ , and each is specific to a *single* peptide plane; see Figure 1.7. But this is not the case of  $\vartheta_{\text{NC}}$  which connects two peptide planes. This angle contributes to the bending of the backbone. Consequently a systematic secondary structure dependence *should* be present in this angle. Due to the very rigid structure of the  $\text{C}\alpha$  centered

*sp*<sup>3</sup>-hybridized covalent tetrahedron one then expects that the secondary structure dependence should also become visible in the side chain specific  $\vartheta_{N\beta}$  and  $\vartheta_{\beta C}$ . The lack of any observable secondary structure dependence in the experimental data of these two angles proposes, that existing validation methods distribute the refinement tension entirely to  $\vartheta_{NC}$ .

*Research project: Can you explain in detail, why secondary structure dependence is absent in PDB data of  $\vartheta_{N\beta}$  and  $\vartheta_{\beta C}$ .*

The construction we have presented, can be continued to visualise all the higher level side chain atoms in a protein, beyond C $\beta$  [105–107]. It turns out that these higher level atoms also display a highly organised, systematic pattern akin those shown in Figure 7.3. In particular, the underlying geometry of the C $\alpha$  backbone is clearly visible in these side chain atoms; there is a very strong coupling between the C $\alpha$  backbone geometry and the side chain geometry. Accordingly it becomes possible, in principle, to highly accurately determine the all-atom structure of the protein from the knowledge of the C $\alpha$  atom positions only. This enables one to extend our C $\alpha$  based approach that builds on (4.17), to construct the full all-atom structure of the entire protein: The C $\alpha$  positions can be computed from the energy function (4.17), and the remaining atoms are located by *s* statistical analysis.

According to Figure 7.3 a) in the intrinsic, purely geometric Frenet frame coordinate system the directions of the C $\beta$  atoms are only subject to small fluctuations. At the level of C $\beta$ , the side chains all point to essentially the same direction. Thus the crystallographic protein structures are like a spin chain where the side chains are the spin variables, and the collapsed phase bears resemblance to a ferromagnetic phase.

*Research project: See how far you get using spin chain analogy of folded proteins, with side chains as the spin variables.*

*That's all, folks*



# References

- [1] E. Schrödinger, "What is Life?" The Physical Aspect of the Living Cell *Cambridge University Press* (1948)
- [2] P. W. Anderson, *Science* **177** 393 (1972)
- [3] K. Dill, S.B. Ozkan, T.R. Weikl, J.D. Chodera, V.A. Voelz, *Current Opinions in Structural Biology* **17** 342 (2007)
- [4] K.A. Dill and J.K. MacCallum, *Science* **338** 1042 (2012)
- [5] F. Chiti and C.Dobson, *Annual Reviews in Biochemistry* **75** 333 (2006)
- [6] J. Davies, *Nature* **383** 219 (1996)
- [7] C.T. Walsh, *Nature* **406** 775 (2000)
- [8] M.A. Fischbach, C.T. Walsh, *Science* **325** 1089 (2009)
- [9] B. Alberts, A. Johnson, J. Lewis, D. Morgan, M. Raff, K. Roberts, P. Walter, *Molecular Biology of the Cell 6<sup>th</sup> Edition Garland Science* (2014)
- [10] L. Frappat, P. Sorba, A. Sciarrino, *Physics Letters* **B250** 214 (1998)
- [11] R.J. Read *et.al.* *Structure* **19** 1395 (2011)
- [12] R.A. Engh, R. Huber, in *International Tables for Crystallography*, Vol. **F**, 382; edited by M. G. Rossmann and E. Arnold (Kluwer Academic Publishers, Dordrecht, 2001)
- [13] R. Joosten *et.al.* *Journal of Applied Crystallography* **42** 376(2009)
- [14] See News at *Nature* **459** 1038(2009)
- [15] Z. Dauter, A. Wlodawer, W. Minor, M. Jaskolski, B. Rupp, *Journal of the International Union of Crystallography IUCrJ* **1** 179(2014)
- [16] P.G. De Gennes, *Scaling Concepts in Polymer Physics Cornell University Press, Ithaca* (1979)
- [17] L. Schäfer, *Excluded Volume Effects in Polymer Solutions, as Explained by the Renormalization Group Springer Verlag, Berlin* (1999)
- [18] L.P. Kadanoff, *Physics* **2** 263 (1966)
- [19] K.G. Wilson, *Physical Review* **B4** 3174 (1971)
- [20] K.G. Wilson, J. Kogut, *Physics Reports* **12** 75-200 (1974)
- [21] M.L. Huggins, *The Journal of Chemical Physics* **9** 440 (1941)
- [22] P.J. Flory, *The Journal of Chemical Physics* **10** 51(1942)
- [23] B. Li, N. Madras, A. Sokal, *Journal of Statistical Physics* **80** 661(1995).
- [24] P.G. De Gennes, *Physics Letters* **38A** 339(1972)
- [25] J.C. LeGuillou, J. Zinn-Justin, *Physical Review* **B21** 3976 (1980)
- [26] K. Hinsen, S. Hu, G.R. Kneller, A.J. Niemi, *The Journal of Chemical Physics* **139** 124115 (2013)
- [27] M.A. Marti-Renom, A.C. Stuart, A. Fiser, R. Sánchez, F. Melo, A. Sali, *Annual Review of Biophysics and Biomolecular Structure* **29** 291(2000)
- [28] T. Schwede, J. Kopp, N. Guex, M.C. Peitsch, *Nucleic Acids Research* **31** 3389 (2003)
- [29] Y. Zhang, *Current Opinions in Structural Biology* **19** 145 (2009)
- [30] C. Chothia, *Nature* **357** 543-544 (1992)
- [31] <http://www.charmm.org/>
- [32] <http://ambermd.org/>
- [33] <http://www.gromacs.org/>
- [34] E. Ott, *Chaos in Dynamical Systems. Cambridge University Press, New York* (2002)
- [35] V.E. Korepin, N.M. Bogoliubov, A.G. Izergin, *Quantum Inverse Scattering Method and Correlation Functions, Cambridge university press, Cambridge* (1997)
- [36] D. E. Shaw, *et al.*, *Communications of the ACM* **51.7** 91(2008)
- [37] D.E. Shaw, *et al.*, *High Performance Computing Networking, Storage and Analysis, Proceedings of the Conference IEEE* (2009)
- [38] K. Lindorff-Larsen, S. Piana, R. O. Dror, D.E. Shaw. *Science* **334** 517(2011)
- [39] G. Gallavotti, *Nonequilibrium and irreversibility*, arXiv:1311.6448v4 [cond-mat.stat-mech]
- [40] S. Nosé, *The Journal of Chemical Physics* **81** 511 (1984)
- [41] W.G. Hoover, *Physical Review* **A31** 1695 (1985)
- [42] G.J. Martyna, M.L. Klein, M. Tuckerman, *The Journal of Chemical Physics* **97** 2635(1992)

- [43] Y. Liu, M.E. Tuckerman, *The Journal of Chemical Physics* **112** 1685(2000)
- [44] A.J. Niemi *Theoretical and Mathematical Physics* **181** 1235(2014)
- [45] H.J.C. Berendsen, J. Pl M. Postma, W.F. van Gunsteren, A.R.H.J. DiNola, J.R. Haak. *The Journal of Chemical Physics* **81** 3684(1984)
- [46] A. Liwo, S. Oldziej, M.R. Pincus, R.J. Wawak, S. Rackovsky, H.A. Scheraga, *Journal of Computational Chemistry* **18** 849(1997)
- [47] H.A. Scheraga, M. Khalili, A. Liwo, *Annual Reviews in Physical Chemistry* **58** 57 (2007)
- [48] A. Liwo, A.J. Niemi, X. Peng, A.K. Sieradzian, A novel coarse-grained description of protein structure and folding by UNRES force field and Discrete Nonlinear Schrödinger Equation, in *Frontiers in Computational Chemistry (Bentham Science Publishers)* (2014)
- [49] N. N. Gö, *Annual Review of Biophysics and Bioengineering* **12** 183(1983)
- [50] T. Haliloglu, I. Bahar, B. Erman, *Physical Review Letters* **79** 3090(1997)
- [51] C.K. Chiang, C.R. Fincher Jr, Y.W. Park, A.J. Heeger, H. Shirakawa, E.J. Louis, S.C. Gau, A.G. MacDiarmid. *Physical Review Letters* **39** 1098(1977)
- [52] R. Jackiw, J.R. Schrieffer, *Nuclear Physics* **B190** 253(1981)
- [53] A.J. Niemi, G.W. Semenoff, *Physics Reports* **135** 99(1986)
- [54] G. Baskaran, Z. Zou, P. W. Anderson. *Solid state communications* **63** 973(1987)
- [55] B.J. Kim, H. Koh, E. Rotenberg, S.-J. Oh, H. Eisaki, N. Motoyama, S. Uchida, T. Tohyama, S. Maekawa, Z.-X. Shen, C. Kim, *Nature Physics* **2** 397(2006)
- [56] S. Coleman, E. Weinberg, *Physical Review* **D7** 1888(1973)
- [57] M.N. Chernodub, L.D. Faddeev, A.J. Niemi, *Journal of High Energy Physics* **12** 014 (2008)
- [58] A.J. Niemi, *Physical Review* **D67** 106004 (2003)
- [59] R.L. Bishop, *The American Mathematical Monthly* **82** 246 (1975)
- [60] S. Hu, M. Lundgren, A.J. Niemi *Physical Review* **E83** 061908 (2011)
- [61] L.D. Faddeev, L.A. Takhtajan, *Hamiltonian methods in the theory of solitons (Springer Verlag, Berlin, 1987)*
- [62] M.J. Ablowitz, B. Prinari, A.D. Trubatch, *Discrete and Continuous Nonlinear Schrödinger Systems (London Mat. Soc. Lect. Note Series 302, London, 2003)*
- [63] A.M. Polyakov, *Nuclear Physics* **B268** 406 (1986)
- [64] O. Kratky, G. Porod, *Recueil des Travaux Chimiques des PaysBas* **68** 1106(1949)
- [65] P.G. Kevrekidis, *The Discrete Nonlinear Schrödinger Equation: Mathematical Analysis, Numerical Computations and Physical Perspectives (Springer-Verlag, Berlin, 2009)*
- [66] N. Manton, P. Sutcliffe, *Topological Solitons (Cambridge University Press, Cambridge, 2004)*
- [67] S. Hu, Y. Jiang, A.J. Niemi, *Physical Review* 105011 (2013)
- [68] T. Ioannidou, Y. Jiang, A.J. Niemi *Physical Review* **D90** 025012 (2014)
- [69] V.I. Arnold, *Singularities of Caustics and Wave Fronts (Kluwer Academic Publishers, Dordrechts, 1990)*
- [70] V.I. Arnold, *Russian Mathematical Surveys* **50** 1 (1995)
- [71] V.I. Arnold, *American Mathematical Society Translations* **171** 11 (1996)
- [72] F. Aicardi, *Functional Analysis and Applications* **34** 79(2000)
- [73] R. Uribe-Vargas, *L'Enseignement Mathématique* **50** 69(2004)
- [74] U.H. Danielsson, M. Lundgren, A.J. Niemi, *Physical Review* **E82** 021910 (2010)
- [75] M.N. Chernodub, S Hu, A.J. Niemi, *Physical Review* **E82** 011916 (2010)
- [76] N. Molkenthin, S. Hu, A.J. Niemi, *Physical Review Letters* **106** 078102 (2011)
- [77] S. Hu, A. Krokhotin, A.J. Niemi, X. Peng, *Physical Review* **E83** 041907 (2011)
- [78] A. Krokhotin, A.J. Niemi, X. Peng, *Physical Review* **E85** 031906 (2011)
- [79] A. Krokhotin, M. Lundgren, A.J. Niemi, *Physical Review* **E86** 021923 (2012)
- [80] A. Krokhotin, A.J. Niemi, X. Peng, *The Journal of chemical physics* **138** 175101 (2013)
- [81] A. Krokhotin, M. Lundgren, A.J. Niemi, X. Peng, *Journal of Physics: Condensed Matter* **25** 325103 (2013)
- [82] R.J. Glauber, *Journal of Mathematical Physics* **4** 294 (1963)
- [83] A.B. Bortz, M.H. Kalos, J.L. Lebowitz, *Journal of Computational Physics* **17** 10 (1975)
- [84] <http://www.cathdb.info/>
- [85] <http://scop.mrc-lmb.cam.ac.uk/scop/>
- [86] J. Skolnick, A.K. Arakaki, Y.L. Seung, M. Brylinski, *Proceeding of National Academy of Sciences USA* **106** 15690 (2009)
- [87] M. Ptashne, *A Genetic Switch, Third Edition, Phage Lambda Revisited. Cold Spring Harbor Laboratory Press, Cold Spring Harbor* (2004)
- [88] M.E. Gottesman, R.A. Weisberg, *Microbiology and Molecular Biology Reviews* **68** 796 (2004)
- [89] P.A. Jennings, P.E. Wright, *Science* **262** 892 (1993)

- [90] Y. Moriyama, K. Takeda, *Journal of Physical Chemistry* **B114** 2430 (2010)
- [91] Y. Ochia, Y. Watabane, H. Ozawa, S. Ikegami, N. Uchida, S. Watabe, *Bioscience, Biotechnology, and Biochemistry* **74** 1673 (2010)
- [92] M.N. Chernodub, M. Lundgren, A.J. Niemi *Physical Review* **E83** 011126 (2010)
- [93] K.N. Woods, *Soft Matter* **10** 4387 (2014)
- [94] P. Westermarck, A. Andersson, G.T. Westermarck, *Physiological Reviews* **91** 795 (2011)
- [95] K. Pillay, P. Govender, *BioMed Research International* **2013** 826706 (2013)
- [96] Jianfeng He, Jin Dai, Jing Li, A.J. Niemi, *The Journal of Chemical Physics* (to appear)
- [97] L. Holm, C. Sander, *Journal of Molecular Biology* **218** 183 (1991)
- [98] S.C. Lovell, I.W. Davis, W.B. Arendall III, P.I.W. de Bakker, J.M. Word, M.G. Prisant, J.S. Richardson, D.C. Richardson, *Proteins* **50** 437 (2003)
- [99] P. Rotkiewicz, J. Skolnick, *Journal of Computational Chemistry* **29** 1460 (2008)
- [100] <http://www.ebi.ac.uk/Tools/structure/maxsprout/>
- [101] <http://cssb.biology.gatech.edu/PULCHRA>
- [102] <http://www.phenix-online.org/>
- [103] <http://www2.mrc-lmb.cam.ac.uk/groups/murshudov/>
- [104] R.L. Dunbrack Jr., *Current Opinions in Structural Biology* **12** 431 (2002)
- [105] M. Lundgren, A.J. Niemi, F. Sha, *Physical Review* **E85** 061909 (2012)
- [106] M. Lundgren, A.J. Niemi, *Physical Review* **E86** 021904 (2013)
- [107] X. Peng, A. Chenani, S. Hu, Y. Zhou, A.J. Niemi, *BMC Structural Biology* (to appear)